creative commons
COMMONS DEED

저작자표시-비영리-변경금지 2.0 대한민국

이용자는 아래의 조건을 따르는 경우에 한하여 자유롭게

- 이 저작물을 복제, 배포, 전송, 전시, 공연 및 방송할 수 있습니다.

다음과 같은 조건을 따라야 합니다:

저작자표시. 귀하는 원저작자를 표시하여야 합니다.

비영리. 귀하는 이 저작물을 영리 목적으로 이용할 수 없습니다.

변경금지. 귀하는 이 저작물을 개작, 변형 또는 가공할 수 없습니다.

- 귀하는, 이 저작물의 재이용이나 배포의 경우, 이 저작물에 적용된 이용허락조건을 명확하게 나타내어야 합니다.
- 저작권자로부터 별도의 허가를 받으면 이러한 조건들은 적용되지 않습니다.

저작권법에 따른 이용자의 권리는 위의 내용에 의하여 영향을 받지 않습니다.

이것은 이용허락규약(Legal Code)을 이해하기 쉽게 요약한 것입니다.

Disclaimer

dCollection

공학박사 학위논문

임베디드 굽힘 센싱을 활용한 보던 케이블 구동 시스템의 장력 제어

Tension Control of a Bowden-Cable Actuation System with Embedded Bending Sensing

2017년 2월

서울대학교 대학원

기계항공공학부

정 우 석

Abstract

Tension Control of a Bowden-Cable Actuation System with Embedded Bending Sensing

Useok Jeong
Department of Mechanical and Aerospace Engineering
The Graduate School
Seoul National University

A critical issue for Bowden-cable transmission is shape-dependent hysteresis that degrades control performance and limits the application. The relationship between input and output of the Bowden-cable varies with the changing bend angle of the cable. This dissertation proposes a novel method that can compensate the varying hysteresis of the Bowden-cable using an embedded auxiliary wire, called a sensing wire. The accumulated bend angle of the Bowden-cable can be estimated by measuring the displacement change of the sensing wire and the input tension of the actuation wire. The estimated bend angle of the sheath can be used to compensate the hysteresis of the Bowden-cable with a feedforward control scheme, even though it is subject to the varying shape of the Bowden-cable. The proposed system has a simple and fully embedded design inside the sheath and does not require any external

shape sensor or output tension sensor, which keeps the size and complexity of the system low. The results show that the control error of output tension decreased from 5.21 N to 0.50 N when the bend angle of the Bowden-cable changes from 0˚ to 400˚. The proposed system was implemented on the soft wearable robotic hand, and the experimental result illustrates that the grasping force was maintained consistent during the operation although the posture of the arm and the shape of the sheath changes.

Keywords : Bowden-cable, cable-conduit, cable actuation, tension control, bending sensing, friction compensation

Student Number : 2010 – 23231

Contents

Abstract ····· **i**

List of Tables ····· **vii**

List of Figures ····· **viii**

Nomenclature ····· **xvii**

Chapter 1 Introduction ····· **1**

1.1 Motivation and Challenges ····· 1

1.2 Objectives and Overview ····· 5

1.3 Scope and Limitation ····· 6

1.4 Contribution ····· 8

Chapter 2 Sheath Bending Sensing ····· **9**

2.1 Concept and Design ····· 9

2.1.1 Principle ····· 10

2.1.2 Maintaining Internal Tension ····· 12

2.1.3 Displacement Change Measurement ····· 13

2.2 Modeling ····· 13

2.2.1 Basic Model ····· 14

2.2.2 Effect of Curvature ····· 16

2.2.3 Advanced Model ····· 19

2.2.4 Sensor Gain ····· 21
2.2.5 Axial Force Robustness ····· 22
2.2.6 Axial Rotational Robustness ····· 23
2.3 Characteristics of the Proposed Bend Sensor ····· 25
2.4 Prototype Development ····· 29
2.4.1 Fabrication Considerations ····· 29
2.4.2 Potentiometer Version ····· 33
2.4.3 Zero Calibration ····· 34
2.5 Experiments ····· 35
2.5.1 Quasi-Static Experiment ····· 36
2.5.2 Large Static Deflection Experiment ····· 40
2.5.3 Robustness ····· 43

Chapter 3 Friction Modeling ····· 46

3.1 Friction Along the Cable ····· 46
3.1.1 Shape-Dependent Friction ····· 46
3.1.2 Shape Variation of the Sheath Inside the Workspace ····· 49
3.2 An Improved Friction Model ····· 52
3.2.1 Deficiency of the Previous Model ····· 52
3.2.2 Improved Model ····· 53
3.2.3 Parameter Fitting ····· 55
3.3 Friction Property Robustness ····· 61
3.3.1 Abrasion Effect ····· 61

3.3.2 Temperature Effect ····· 63

Chapter 4 Actuation with Embedded Bending Sensing ·· 66

4.1 Concept ····· 66

4.1.1 Principle ····· 66

4.1.2 System Configuration ····· 68

4.2 Bend Estimation during Actuation ····· 70

4.3 Multi-Bending Curvature ····· 78

4.4 Friction Compensation ····· 80

4.4.1 Compensation Rule ····· 80

4.4.2 Friction Degradation ····· 81

4.5 Tendon Actuator ····· 83

4.5.1 Slack Enabling Actuator ····· 83

4.5.2 Tension Controller ····· 86

4.5.3 Zero-Tension Controller ····· 90

4.6 Experiments ····· 95

4.6.1 Experimental Setup ····· 95

4.6.2 Results ····· 96

Chapter 5 Implementation and Application ····· 102

5.1 Exo-Glove ····· 102

5.1.1 Influence of Antagonistic Tension of the Wire ····· 103

5.1.2 Grasping Force with Different Arm Postures ····· 106

5.2 Endoscopic Forceps ····· 111

Chapter 6 Concluding Remarks ····· 114

Appendix ····· 117

Bibliography ····· 121

국문 초록 ····· 128

List of Tables

TABLE 1. COMPARISON OF SENSOR CHARACTERISTICS. 26

TABLE 2. SPECIFICATION AND PRICE LIST OF THE PROTOTYPE COMPONENTS (US DOLLARS). 32

List of Figures

Figure 2-1 A Bowden-cable–based bend sensor consists of an inner wire and an outer sheath. 9

Figure 2-2 Structure of the bending part of the proposed bend sensor, which consists of a helical coil, an inner wire, a Teflon® lining and an end-cap. 10

Figure 2-3 Basic working principle of the proposed bend sensor using a Bowden-cable. (**a**) When the sensor is straight; (**b**) When the sensor is bent. 10

Figure 2-4 Sensor bending with multiple bending points. The displacement change of the center line is proportional to the accumulated bend angle throughout the helical coil, $\Phi = \phi_1 + \phi_2 + \phi_3 + \phi_4$. 11

Figure 2-5 Two ways of maintaining internal tension and measuring the displacement change of the sensing wire. (**a**) Using a linear spring and a linear transducer; (**b**) Using a spool with a torsional spring and a rotational transducer. 12

Figure 2-6 Schematic of a bent helical coil showing the displacement change of the line passing through the center of the coil. Each coil pitch uniformly bends by α, resulting in a central displacement increment of x. 15

Figure 2-7 Simulation result of derived equation (2-4) when coil wire diameter b = 0.5 mm. It shows the linear relation between bend angle and the central displacement change, although (2-4) contains nonlinear functions. The curves with different length, L, are overlapped with the curves for the same coil diameter, d. 15

Figure 2-8 Simulation result showing how the displacement change rate varies with the bend curvature, κ, and the coil wire diameter, b, when d = 3 mm. The displacement change rate can be assumed to be constant within a certain range of design parameters and curvatures. 18

Figure 2-9 Simulation result of the approximation error depending on the normalized curvature. Large variation of the normalized curvature during sensor operation can lead to measurement error, but not by much—the change rate varies within 1.0% with extreme conditions when K = 0.5 (κ = 1000 m^{-1} when b = 0.50 mm). This can be approximated to a constant value during actual conditions of sensor operation. 18

Figure 2-10 The sensing wire does not maintain its position in the center of the coil because there are gaps between the sensor's parts. The effective distance between the center of the sensing wire and the outside wall of the helical coil, d_{eff}, should be considered when calculating the sensor gain derived in **Chapter 2.2.1**. 20

Figure 2-11 The model should be modified for a coil wire with a circular cross-sectional area for more accurate modeling. (**a**) Model modification for a circular cross-section; (**b**) Close view of the contact point between the two coil pitches. 21

Figure 2-12 Axial force robustness. (**a**) Safe region; (**b**) A sensing error occurs when the external axial force is higher than the wire tension and the initial tension. 23

Figure 2-13 Axial rotation along the helical coil causes only a small length change of the helical coil. The sheath (**a**) contracts with counter-clockwise rotation and; (**b**) extends with clockwise rotation. 24

Figure 2-14 Comparison of the representative characteristics of the proposed sensor (middle area with the patterns), the Flex sensor (right area), and the optical fiber-based sensor (left area). 25

Figure 2-15 Computer-assisted design (CAD) model of the bend sensor prototype. (**a**) Overall view of the sensor consisting of a sensing part and a bending part; (**b**) Close view of the sensing part, which provides tension to the sensing wire and measures its position. 31

Figure 2-16 Developed prototype of the bend sensor that consists of the sheath, sensing wire, supporting structure, spool, linear spring, and rotational

encoder.....32

Figure 2-17 Sensing part of the sensor prototype using the rotary potentiometer (3382G-1-103G, 2% nonlinearity, Bourns, Inc.). 33

Figure 2-18 Zero calibration algorithm for the bend sensor that uses the incremental encoder for the displacement measure of the sensing wire. 34

Figure 2-19 Simulation result of the zero calibration algorithm for the bend sensor. 35

Figure 2-20 Setup for the quasi-static experiment. The sensor sheath was constrained to the desired bend angle, and the setup was moved by hand. 36

Figure 2-21 Results for the quasi-static experiment in the time domain. (**a**) Reference angle (gray thick line), model-based sensor output (black solid line), and calibrated sensor output (gray dotted line) in the time domain; (**b**) Sensing error of model-based sensor output (black solid line) and calibrated sensor output (gray dotted line) in the time domain. 38

Figure 2-22 Results for the quasi-static experiment in the reference angle domain. (**a**) Reference angle (gray thick line), model-based sensor output (black solid line), and calibrated sensor output (gray dotted line) in the reference angle domain; (**b**) Sensing error of model-based sensor output (black solid line) and calibrated sensor output (gray dotted line).....39

Figure 2-23 Setup for the large static deflection experiment using a 90° bending bracket with three different curvatures. (**a**) $\kappa = 80.0\ m^{-1}$; (**b**) $\kappa = 26.7\ m^{-1}$. 40

Figure 2-24 Experimental results showing the output signal with various bending angles and curvatures. (**a**) Sensor output with difference curvatures showing model-based output (black) and calibrated output (gray); (**b**) Sensing error with different curvatures, showing model-based output

(black) and calibrated output (gray). 42

Figure 2-25 Experimental result of the bend sensor robustness showing the sensor output with the reference angle from 1 cycle (blue line) to 11,000 cycles (orange line). The output signal decreases with the repetitions. 43

Figure 2-26 Experimental result of the bend sensor robustness showing the sensor output on the reference angle 90° with the repetitions. 44

Figure 2-27 Experimental result of the bend sensor robustness showing the zero-offset change with the repetitions. 44

Figure 2-28 Experimental result of the bend sensor robustness showing the sensor gain (cnt/deg) change with the repetitions. It remains consistent until 6,150 cycles and starts to decrease with the rate of -9.57×10^{-5} cnt/deg per cycle. 45

Figure 3-1 Schematic diagram of a static friction model along the wire. 46

Figure 3-2 Characteristics of the relation between input and output. 47

Figure 3-3 Friction characteristics of the Bowden-cable changes as the accumulated bend angle changes. The graph is plotted with the friction coefficient $\mu = 0.1$. 48

Figure 3-4 Schematic of a free hanging sheath between two points, *A* and *C*. .49

Figure 3-5 Simulation result of the bending angle error assuming that the actuator is placed on (0,0,0). 51

Figure 3-6 The experimental data showing the deficiency of the previous model. 52

Figure 3-7 Comparison between previous and improved model for (upper) $\phi = 0$ and (lower) $\phi = 2\pi$. Parameters for previous and modified model: $\mu = 0.0721$, $\mu = 0.05$; $\varsigma = 4$ N; $\eta_0 = 0.9$ 54

Figure 3-8 Block diagram of a phase filtering algorithm (stage 1 to 7) for the data set of input and output tension of the Bowden-cable. 56

Figure 3-9 The processed data of the phase filtering algorithm showing raw data,

processed data of low pass filtering, thresholding, and moving averaging. 58

Figure 3-10 Results of the phase filtering with the data set from the bend angle of 0˚, 90˚, 180˚, 270˚, 360˚, 450˚, and 540˚. Each phase is differentiated by different colors. 58

Figure 3-11 Experimental results of the input and output tension of the wire with different bend angles (0˚, 90˚, 180˚, 270˚, 360˚, 450˚, and 540˚). The original and modified models are fitted. 59

Figure 3-12 The comparison of errors with the original and modified models. Each dots refer data points and the dotted lines indicate the root-mean-square values of the errors. 60

Figure 3-13 Root-mean-square error of the fitted model depending on the bend angle. The total RMS value of the modified model (red-dotted, 1.2980 N) is 39.63% lower than the total RMS value of the original model (black-dotted, 0.7836 N). 60

Figure 3-14 Input and output tension of the Bowden-cable actuation system with the repetitive operation up to 9,700 repetitions. 62

Figure 3-15 Experimental data of the friction coefficient with the increasing number of trials. The friction coefficient is calculated using the previous friction model. 62

Figure 3-16 Input and output tension of the Bowden-cable actuation system with the varying temperature from −50 °C to +70 °C. 64

Figure 3-17 Experimental data of the friction coefficient with the varying temperature from −50 °C to +70 °C. 64

Figure 4-1 Dual-wire scheme combining an actuation wire and a sensing wire. 66

Figure 4-2 Qualitative comparison of different cable actuation approaches. 67

Figure 4-3 Block diagram of the proposed sensorless control system of a Bowden-cable with a dual-wire scheme. The system consists of five

parts: Bowden-cable with embedded sensing wire, end-effector, bend estimation system, friction compensation algorithm, and tension-controlled tendon actuator. 69

Figure 4-4 Compressive force is applied to the sheath and the supporting parts along the axial direction as a reaction force to the tension of the actuation wire. 70

Figure 4-5 The graphs showing the tension distributions along the cable for four phases; (**a**) steady-state winding; (**b**) transient-state releasing; (**c**) steady-state releasing; (**d**) transient-state winding. 72

Figure 4-6 The compression model of the sheath and supporting parts with the original model (blue solid line) and the approximated model (orange dotted line) for the bend angle (**a**) $\phi = 0$; (**b**) $\phi = \pi$; (**c**) $\phi = 2\pi$; (**d**) $\phi = 3\pi$. The approximated model represents the hysteresis curve of the original model but with the easily implementable linear lines. 74

Figure 4-7 The region that satisfies the convergence condition in (4-12). The condition of the operating range ($\eta_0 = 0.95$, $\varsigma = 4$ N, $A = 0.269$ mm/rad, $E_s = 54{,}000$ N, $\mu = 0.05$, $0 \le \phi \le 3\pi$, $0 \le T_s \le 80$ N) satisfies the convergence of the solution for (4-1) using the fixed-step iteration up to $L = 5$ m with the assumption that the output support part is rigid ($K_{out} \to \infty$). 76

Figure 4-8 Simulation result of the bend estimation using the fixed-point iteration with a loop time 0.1 s showing the convergence of the estimated bend angle. 77

Figure 4-9 Simulation result of the bend estimation with a varying bend angle of the sheath and the input tension of the wire using the approximated compression model and fixed-point iteration. Simulation condition: $\mu = 0.05$; $\varsigma = 4$ N; $\eta = 0.95$; $K_s = 180$ N/mm; loop time = 0.01 s.....77

Figure 4-10 A schematic of the sheath and the sensing wire showing the effect of wire-sheath gap on multi-bending curvature. 78

Figure 4-11 The simulation result illustrating the error of the bend angle due to

the sheath-wire gap with two adjacent curves with the same amount of curvature and different direction. Plotted with the different curvatures and backlash gap ($\alpha = D - d$).....79

Figure 4-12 The simulation result that shows the output tension of the system with the friction coefficient increment of the system in the time domain. (solid line) tesnsion setpoint; (dashed line) 10%; (dotted line) 20%; (dash-dot line) 30% increment of the friction coefficient.....82

Figure 4-13 The simulation result showing the control error, $[T_s - T_{out}]/T_s \times 100\%$, in the setpoint domain with the fricion coefficient increment. (solid line) non-changing; (dashed line) 10%; (dotted line) 20%; (dash-dot line) 30% increment of the friction coefficient.....82

Figure 4-14 The simulation result showing the root-mean-square error of the output tension with the friction coefficient increments from 0% to 30% and the bend angle from π to 4π. 83

Figure 4-15 Concept of slack enabling mechanism: (**a**) winds the output 1 tendon, (**b**) releases the output 2 tendon.....85

Figure 4-16 The step (above) and the sinusoidal (bottom) responses of the tension controller for the slack enabling actuator.....90

Figure 4-17 Simulation result that shows the drift of the wire position when the tension setpoint is zero with the white noise (0.05 N amplitude) on the tension measurement. 92

Figure 4-18 Simulation result that shows the divergence of the system when the tension setpoint is zero with the white noise (0.05 N amplitude) and the bias (0.1 N) on the tension measurement.....92

Figure 4-19 The concept of the zero-tension controller that regulates the control gain of the tension controller to make the controller stable on zero-tension using the tension and position feedback.....93

Figure 4-20 The experimental result of the zero-tension controller. (**a**) The tension setpoint is set to zero and it does not show instability as in **Figure 4-17** and **Figure 4-18**; (**b**) The wire is pulled by hand and it shows

backdrivable interaction; (**c**) The tension setpoint is set to 10 N. The position of the wire increases with the threshold speed 20 mm/s until the slack of the wire is eliminated and the tension converges to 10 N without the overshoot. 94

Figure 4-21 Experimental setup for the Bowden-cable control system, consisting of an actuator, actuation wire, bend sensor, sensing wire, sheath, and end-effector. 95

Figure 4-22 Experimental result of sensing wire length changes with varying input tension of the actuation wire and the accumulated bend angle of the sheath. 97

Figure 4-23 Bend angle estimation of the sheath using the sensing wire with and without sheath compression compensation. 97

Figure 4-24 Experimental result showing the tension of the setpoint, input, and output at different accumulated bend angles of the sheath over time. 99

Figure 4-25 Results for feedforward force control with bend estimation. 100

Figure 5-1 Examples of sheath path bending on soft wearable robot. (**a**) 0; (**b**) 2π; (**c**) π.....103

Figure 5-2 Simulation result of finger trajectory while winding agonist tendon and exerting the friction of antagonist tendon. 105

Figure 5-3 Example of deformation of soft wearable robot. 106

Figure 5-4 The Exo-Glove Poly [76] with the embedded bending estimation system. 107

Figure 5-5 Branching part of the Exo-Glove Poly that the one end of the sensing wire is fixed on. The actuator side of the branching part consists of the sheath, Teflon lining, actuation wire, and sensing wire while the glove side of the branching part does not have the part of sensing wire. 107

Figure 5-6 Grasping force measurement using the force sensor (100 N capacity,

Ktoyo) and the polycarbonate plate. 108

Figure 5-7 Three different arm postures that involve different bend angles of the sheath. (**a**) $\phi \approx 0$; (**b**) $\phi \approx \pi$; (**c**) $\phi \approx 2\pi$ 108

Figure 5-8 The measured grasping force of the Exo-Glove Poly, not using (blue) and using (orange) the proposed actuation method with three different arm postures 109

Figure 5-9 The peak grasping forces measured with three different arm postures, not using (blue) and using (orange) the proposed actuation method. 109

Figure 5-10 The endoscopic forceps that consist of the spring sheath, actuation wire, and gripper. (US Endoscopy [77]) 111

Figure 5-11 (**a**) EndoSamurai [82] (Olympus Corp., Tokyo, Japan); (**b**) Anubis scope® [83] (Karl Storz, Tuttlingen, Germany); (**c**) a "fourth generation" endoscopic platform [84] (Boston Scientific Corp., Natik, USA); (**d**) the R-scope [85] (XGIF−2TQ240R; Olympus Corp., Tokyo, Japan); (**e**) ShapeLock Endoscopic Guide [86] (USGI Medical, Inc., San Clemente, USA); (**f**) ShapeLock Cobra [86] (USGI Medical, Inc., San Clemente, USA) 112

Figure 5-12 The insertion of the endoscope through the mouth that requires complex routing path along the organs. 113

Nomenclature

ϕ	rad	Local bend angle of the sheath
Φ	rad	Accumulated bend angle along the sheath
Φ_{gap}	rad	Error of bend angle due to the sheath-wire gap
$\Phi_{friction}$	rad	Effective bend angle that is related to the friction along the sheath
$\widehat{\Phi}$	rad	Estimation of the sheath bend angle
θ	rad	Rotational angle of the bending sensing spool
α_i	rad	Local bend angle between each coil pitch
x_i	mm	Local displacement change of the sensing wire between each coil pitch
b	mm	Wall thickness of the spring sheath
b_{tube}	mm	Wall thickness of the inner tube of the sheath
d_{wire}	mm	Diameter of the sensing wire
L	mm	Length of the sheath
d	mm	Outer diameter of spring sheath
Δl	mm	Displacement change of the sensing wire
$\Delta\tilde{l}$	mm	Measurement of the displacement change of the

		sensing wire
κ	mm^{-1}	Bend curvature of the sheath
A	mm/rad	Sensing wire displacement change rate
A_{eft}	Mm/rad	Effective displacement change rate of the sensing wire
K	–	Non-dimensionalized curvature
Λ	–	Non-dimensionalized sensing wire displacement change
X	–	Non-dimensionalized sensing wire displacement change rate
F_{axial}	N	Axial force applied on the sheath
φ_{axial}	N·mm	Axial torque applied on the sheath
F	N	Friction force between the inner wire and the sheath
N	N	Normal force between the inner wire and the sheath
T	N	Tension along the Bowden-cable
T_{in}	N	Input tension of the Bowden-cable
T_{out}	N	Output tension of the Bowden-cable
T_{out}^{steady}	N	Output tension of the Bowden-cable in steady-state
T_s	N	Tension setpoint of the actuation system

T_c	N	Friction compensated reference tension
p	mm	Position of the inner wire (sheath axial axis coordinate)
v	mm/s	Velocity of the inner wire (sheath axial axis coordinate)
μ	–	Friction coefficient of the Bowden-cable
ς	N/rad	Coefficient of tension independent normal force
η_0	–	Inherent efficiency of the Bowden-cable
E_i	N	Error function which is a difference between the experimental output tension and the model-based output tension
P	–	Model parameter set of the improved friction model
$\Delta L_{compress}$	mm	Compression of the sheath and the supporting parts originated from the tension of the actuation wire
ΔL_{sheath}	mm	Deformation of the sheath originated from the tension of the actuation wire
ΔL_{sheath}^{wn}	mm	Compression of the sheath on the winding state
ΔL_{sheath}^{rl}	mm	Compression of the sheath on the releasing state
$\Delta L_{sheath}^{steady}$	mm	Compression of the sheath on the steady-state phase
ΔL_{in}	mm	Deformation of the supporting part of the input port

		originated from the tension of the actuation wire
ΔL_{out}	mm	Deformation of the supporting part of the output port originated from the tension of the actuation wire
E_s	N	Young's modulus of the sheath multiplied by the cross-sectional area
K_s	N/mm	Stiffness of the sheath
K_{in}	N/mm	Stiffness of the supporting part of the input port
K_{out}	N/mm	Stiffness of the supporting part of the output port
Δl_{gap}	mm	Displacement changes of the sensing wire when it is subjected to sheath-wire gap
u	N·mm	Control input to the motor
m	kg·mm	Effective inertia of the slack enabling actuator
k_m	N/mm	Effective stiffness of the slack enabling actuator
c	N·s/mm	Effective damping of the slack enabling actuator
K_a	–	Feedback gain of the tension controller
z_i	–	States of the tension controller
w	N·s	Integrated term of the tension controller
y	N	Output of the Bowden-control actuation system
L_o	–	Observer gain of the tension controller

ε	N	Tension sensing error that consists of the white noise and offset
v_{th}	mm/s	Threshold speed of the zero-tension controller
T_{th}	N	Threshold tension of the zero-tension controller

Chapter 1 Introduction

Bowden-cable, which is also referred to as cable-conduit and sheath tendon system, is a tendon-driven mechanism that transmits power through a wire. The flexible characteristic of the Bowden-cable has been widely adopted in many robotic applications that require a complex and varying shape of a transmission path. It can also transmit power remotely, and the power source can be placed out of the end-effector, reducing a robot's weight, size, and complexity.

Wearable robots for hands [1]–[5] and lower limbs [6], [7] have been developed using the Bowden-cable to minimized the complexity of the structure and reduce the weight of the devices. In particular, soft wearable robots take advantage of flexible characteristics of the Bowden-cable in their soft tendon routing systems [1]. Endoscopes [8], [9], catheters [10], and surgical tools [11] have also adopted Bowden-cable transmission because these devices require a slender and flexible design.

1.1 Motivation and Challenges

Tendon Driven Mechanism

A tendon-driven mechanism (TDM) has been adopted to increase the density of degrees of freedom and to reduce the weight of the device on various robotic systems, including wearable robots and robotic hands [12]–[14]. The advantage of a TDM is that because its power is transferred via wire, the actuator can be remotely placed, increasing freedom for the position of the actuator. Additionally, owing to the small volume of the wire, the transmission can be compacted into a small space. TDMs can be divided into two categories: pulley-routed and suspended TDMs [14]. Most

tendon driven systems have adopted the pulley-routed TDM in which the tendon is routed on a pulley to transfer power [15]. Certain systems use a suspended TDM in which one end of the tendon is fixed to the link and the other end to the actuator [16]. Among these, Bowden cable, which is a representative type of suspended TDM, has the highest degrees of freedom for wire path. Moreover, Bowden cable was developed in advance to soft tendon routing system [1] which provides a guideline for routing Bowden cable system.

Shape-Dependent Cable Friction

Shape-dependent hysteresis is a Bowden-cable issue that suppresses its use in many applications. Friction along the cable varies with the accumulated bend angle of the cable [17]–[20]. There have been studies to compensate the hysteresis of the Bowden-cable for more accurate control. Output feedback control reduces the effort required to obtain accurate modeling of the varying hysteresis. Some studies used output feedback without hysteresis modeling for simple adoption [3], [4], [6]. Others used serial elastic actuation (SEA), which entails using a spring and position sensor on the output port, for more accurate torque control of the joint [7], [21], [22]. The performance of the feedback control can be further improved by combining feedforward compensation of the nonlinearities using a hysteresis model [8], [9], [17], [18], [20]. However, these methods using the output feedback require additional sensors on the output port, which increases the size of the end-effector, making it difficult to implement the method in devices that require compact size, such as surgical tools and wearable robots. Other studies used feedforward compensation alone without output feedback to eliminate the bulky sensing part of the end-effector [11], [23]. However, this method cannot deal with the varying shape of the cable and can only be used with a cable of fixed shape, which limits the application. Jeong et al. [24] introduced a loop routing that forces the sheath to

maintain the same friction characteristic wherever the end-effector placed within a two-dimensional space. However, loop routing does not allow external forces or constraints on the sheath so it cannot be used inside continuum robots such as endoscopes and catheters.

Consequently, shape sensing of the sheath became an important issue for a Bowden-cable intended for use without output feedback in the condition of a varying-shape cable [10]. Laby et al. (Intuitive Surgical, Inc.) [25] introduced an optical fiber–based shape sensor for a surgical device to compensate the hysteresis change of the cable-driven tool with a varying shape cable inside the human body. Also, continuum robots have adopted optical fiber–based shape sensors to eliminate nonlinearities and estimate the position of the end-effector [26]–[28]. Although the optical fiber–based sensors are thin and sensitive, these sensors require a very expensive interrogator to measure and analyze the light spectrum with intensive signal processing.

Bend Angle Estimation

Bend sensors have been widely used in various applications, from simple angle measurements to flexion and extension measurements of the body joints [29]–[39] and shape-sensing in mechanical structures [40]–[42]. Flex sensors and optical fiber sensors have proved useful in these applications.

A Flex sensor is a thin film printed with conductive ink whose resistance changes depending on the bend curvature and angle of the sensor [29], [43]. It is the most affordable bend sensor on the market, and several companies sell off-the-shelf versions of various dimensions [44], [45]. Some research [40]–[42], [46] and do-it-yourself projects [30] use Flex sensors because they are cheap, easy to integrate, and do not require complicated signal processing. Motion capture gloves measuring the

posture of the fingers using Flex sensors have been developed [29], [31]–[33] and commercialized [34] because they can be easily attached to fabric without adding volume. However, Flex sensors tend to have large nonlinearities, including time-dependent creep and a nonlinear relationship between curvature and resistance change [31], [32], [47], [48]. The nonlinearity of Flex sensors prevents them from measuring large curvatures and the absolute angles of objects. They are also limited in length (maximum, 95.25 mm for the Spectra Symbol Flex sensor) and so cannot measure a bend change for a large area [32].

Optical fiber-based sensors detect bending by measuring changes in intensity, phase, wavelength, or polarization of the light inside a bending optical fiber [31], [32]. The elaborate and intensive techniques used to manufacture the optical fiber and sophisticated signal processing of the light spectrum enable highly sensitive measurements of fiber shape changes [49]. Also, these sensors take advantage of the physical properties of optical fibers, including small diameter and flexibility. Optical fiber-based sensors can be divided into two types depending on whether they measure the spectrum or the overall intensity of light [50]. Grating-based sensors including fiber Bragg gratings (FBGs) and long-period fiber gratings (LPFGs) measure the intensity variation of the fiber's resonant dip wavelength [51]–[54]. An expensive device—an interrogator—is used to measure and analyze the spectrum of the light, and complicated signal processing is required to convert the spectrum data into curvature information [31], [32], [49]. It is possible but difficult to minimize the effect of temperature and nonlinearities via special fabrication techniques [52], [55]. Optical fiber-based sensors that measure light intensity were proposed [35], [36], [50] as a low-cost alternative to spectrum-analyzing sensors. These measure intensity changes in the light source of light-emitting diodes (LEDs) with photodiodes as the fiber bends. However, this type of sensor is used only to measure small curvatures [50].

Electronic textiles (e-textiles) are an emerging technology that can be used for bending sensing [37]–[39]. The fabric or thread used to make these textiles changes its electric properties depending on the stretch of the material. They are advantageous for wearable devices because the sensing material itself can be an integral part of the device. However, electronic textiles show high nonlinearities [39] and have limited application other than for wearable devices.

1.2 Objectives and Overview

This dissertation proposes a novel actuation system for the Bowden-cable transmission with a bend estimation based on an embedded sensing wire. This approach is advantageous because the sensing wire can be embedded inside the actuation sheath, which enables a simple and compact design. The estimated bend angle of the sheath can be used to compensate the cable hysteresis in a feedforward compensation manner that eliminates the requirement for a sensor on the end-effector, minimizing the size and simplifying the structure.

The rest of the dissertation is organized as follows. **Chapter 2** introduces the novel bending sensing methodology which utilizes the position error of the Bowden-cable that can be embedded inside the Bowden-cable actuation system. In **Chapter 3**, an improved friction model with an increased accuracy will be discussed that supplements the previous friction model. This improved friction model contributes to more accurate friction compensation of the system. **Chapter 4** proposes a new Bowen-cable actuation system with embedded bending sensing that can control the output tension of the wire without output feedback while subjected to the varying shape of the sheath. An application of the proposed system on the wearable robotic hand is presented in **Chapter 5** that promises the consistent grasping forces with different arm postures. And **Chapter 6** concludes the dissertation.

1.3 Scope and Limitation

The general purpose of this dissertation is providing a basic idea for the tension control of the Bowden-cable using the embedded bending sensing.

The following lists are the scope of this dissertation to discuss the above purpose:

- Proposition of a concept of bending sensing system using a Bowden-cable;
- Modeling of the bending sensing system on a relationship between the accumulated bend angle and the output signal of the sensor;
- Prototype development of the proposed bending sensing system;
- Experimental validation of the proposed bending sensing system with quasi-static continuous bend (0–120°) and large static deflection (0–450°, κ = 26.7 m^{-1}, 40.0 m^{-1}, and 80.0 m^{-1});
- Robustness test of the proposed bending sensing system using a repetitive bending;
- Proposition and experimental validation of an improved friction model for the Bowden-cable that introduced a tension independent normal force and an inherent efficiency;
- Development of a parameter fitting algorithm for the Bowden-cable friction model;
- Experiment and analysis for a robustness of the friction characteristics of the Bowden-cable subjected to a repetitive operation and a temperature change;
- Proposition of a tension control methodology for the Bowden-cable introducing a sensing wire to estimate the sheath bend and compensate the friction;
- Bend estimation of the Bowden-cable using the sensing wire during the actuation considering the compression of the parts;

- Development of a compression model for the Bowden-cable system considering the friction distribution along the cable;
- Prototype development for the Bowden-cable tension control system with the embedded bending sensing;
- Development of a tension control algorithm for the slack enabling actuator that has high bandwidth and can cope with zero-tension;
- Integration of the proposed Bowden-cable control system with Exo-Glove and the grasping force control;
- Proposal of the proposed Bowden-cable control system to be integrated with an endoscopic forceps;

The following lists are the limitations and the future research that are not covered by the scope of this dissertation:

- A dynamic response of the bending sensing system using the Bowden-cable should be studied;
- A dynamic effect of the friction properties should be further considered on the friction compensation of the proposed system;
- A methodology and implementation to compensate the degradation of the cable system with the repetitive operation and the effect of the temperature change should be further studied;
- An integration and experimental evaluation of the proposed actuation system with the endoscopic forceps;

1.4 Contribution

The main contribution of this dissertation is developing a Bowden-cable actuation system with embedded bending sensing that can accurately control the output tension without using the force sensor on the end-effector. The contribution of this dissertation can help Bowden-cable actuation systems to be more compact and improve the control performance. In addition, the proposed approach combining the actuation system, structure, and sensing system contribute a basic idea of soft actuation in soft robots.

The main accomplishments of this dissertation are:

- Proposed a **novel bending sensing system** that can be fully embedded inside the Bowden-cable actuation system;
- Proposed a **shape robust Bowden-cable actuation system** that can compensate the friction along the cable without using the force sensor on the end-effector;
- Contribute to a **soft actuation** methodology using a tendon sheath structure that combines actuation, structure, and sensing of the system;

Chapter 2 Sheath Bending Sensing

2.1 Concept and Design

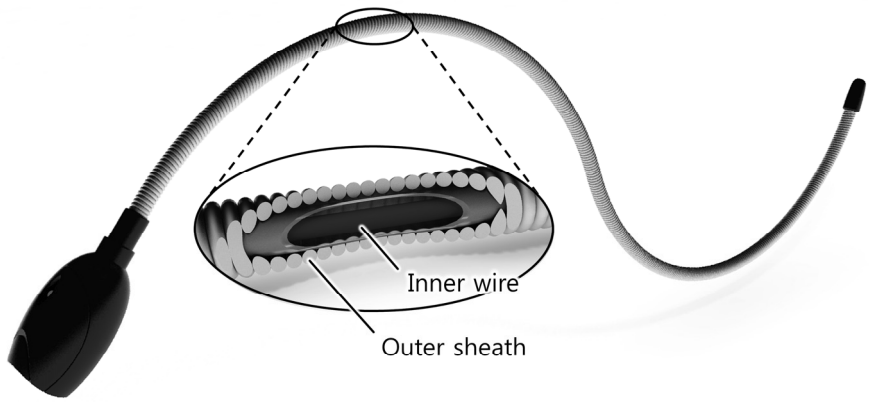

Figure 2-1 A Bowden-cable–based bend sensor consists of an inner wire and an outer sheath.

This chapter proposes a novel bending sensing methodology based on the Bowden-cable that operates on principles completely different from those at work in Flex sensors and optical fiber-based sensors. A Bowden-cable is a wire-driven mechanism that consists of an inner wire and an outer sheath that transmits force through the inner wire. It provides high degrees of freedom in the routing path because the transmission consists of flexible components. It has been used in bicycle brake systems for decades and in many robotic applications, from exoskeleton robots [1], [2], [6], [7] to surgical devices [8]–[10], [56]. One issue with Bowden-cables is property changes [24], especially related to a position error of the inner wire originating from the varying shape of the coil sheath [8]–[10], [56].

This study takes advantage of position error in the Bowden-cable to detect the bend angle of the sheath. When one end of the inner wire is fixed to the sheath, the

displacement change of the inner wire can be measured on the other end of the sheath. There is a linear relationship between the displacement change of the inner wire and the accumulated bend angle of the sheath such that the sheath can be used as the sensor body of a bend sensor. The design and material of the proposed sensor are simple, low cost, and does not require any special fabrication techniques or complicated signal processing. Based on these attributes, the author used a Bowden-cable to develop a low-cost, easy-to-use bend sensor (**Figure 2-1**) capable of sensing over a wide range of accumulative bend angle with a large curvature (up to 450° bend angle and 80.0 m^{-1} curvature for the first prototype).

2.1.1 Principle

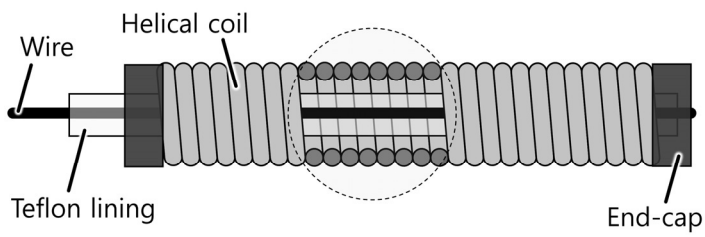

Figure 2-2 Structure of the bending part of the proposed bend sensor, which consists of a helical coil, an inner wire, a Teflon® lining and an end-cap.

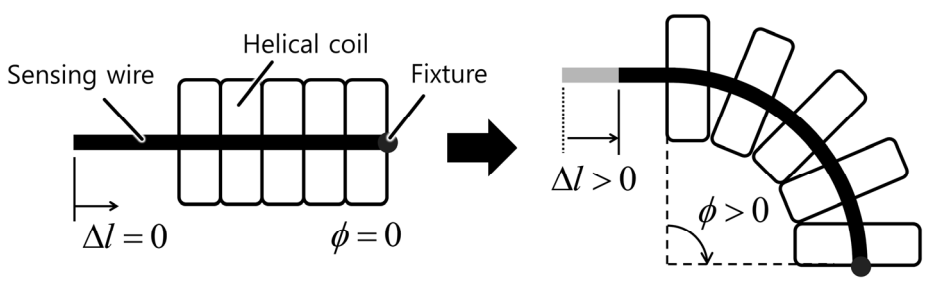

(**a**) (**b**)

Figure 2-3 Basic working principle of the proposed bend sensor using a Bowden-cable. (**a**) When the sensor is straight; (**b**) When the sensor is bent.

The working principle of the proposed bend sensor starts from the idea that the displacement of the line passing through the center of a helical coil increases as the coil bends, as shown in **Figure 2-2** and **Figure 2-3**. This occurs because each coil pitch remains in contact inside the curvature but the gap between each coil pitch on the outside of the curvature increases, as shown in **Figure 2-3 b**. This results in a displacement change of the center line (this is linearly related to the bend angle of the helical coil, which will be addressed in more detail in the next section). The displacement change can be measured with a wire that is placed through the center of the coil and fixed at one end of the coil and a displacement sensor such as a potentiometer or a Hall-effect sensor.

This idea can be extended to the whole body of the sheath: Central displacement changes of the sensor are related to the accumulated bend angle of the sensor (depicted in **Figure 2-4**).

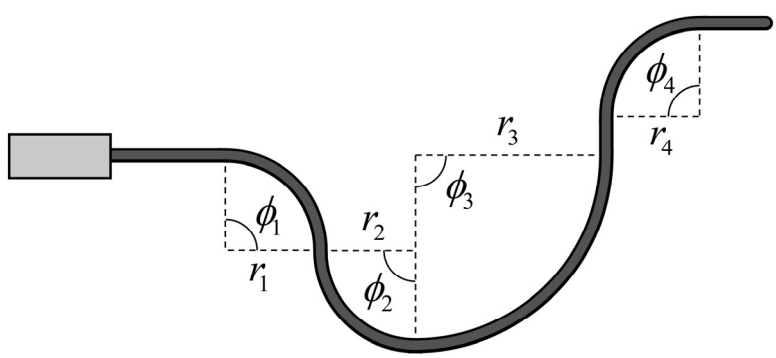

Figure 2-4 Sensor bending with multiple bending points. The displacement change of the center line is proportional to the accumulated bend angle throughout the helical coil, $\Phi = \phi_1 + \phi_2 + \phi_3 + \phi_4$.

2.1.2 Maintaining Internal Tension

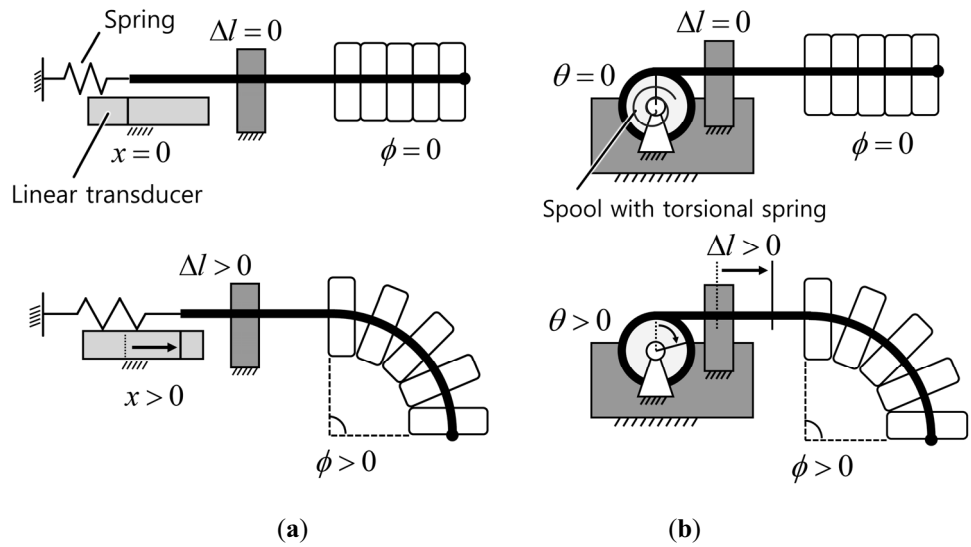

Figure 2-5 Two ways of maintaining internal tension and measuring the displacement change of the sensing wire. (**a**) Using a linear spring and a linear transducer; (**b**) Using a spool with a torsional spring and a rotational transducer.

The tension of the sensing wire inside the helical coil should be maintained over a certain range to prevent it from becoming slack, which would prevent accurate measurement of the central displacement change. There are two possible ways to keep the sensing wire taut. One is to use a passive element such as a spring to provide an elastic force to the sensing wire. **Figure 2-5** shows examples of this method using a linear and a torsional spring. The free end of the sensing wire can be connected to a linear spring (**Figure 2-5 a**) or wound around a spool with a torsional spring (**Figure 2-5 b**). The spring should have some initial stretch to keep the sensing wire taut, even for a straight-shaped sensor. Inner tension increases as the sensor bends, and central displacement of the coil increases as well. In this case, the operating range of the spring should cover the travel range of the sensing wire, which is determined by the bending sensing range and the design parameters of the sensor.

The other method is to maintain internal tension using an actuator such as an electric motor or piezo motor. This method can provide either constant or variable tension to the sensing wire, which enables the sensor to have variable bending stiffness or optimizes hysteresis properties. In all cases, tension should be maintained within a range that induces only negligible elongation of the wire. The wire stretch should be considered when calculating the bend angle if elongation of the wire is more than negligible.

2.1.3 Displacement Change Measurement

One end of the sensing wire is attached to the end of the helical coil, and the other free end of the sensing wire is connected to a displacement sensing device to measure the central displacement change of the helical coil. There are two possible ways to measure the position of the free end of the sensing wire. The first method merely measures the linear position of the free end of the sensing wire using a linear position transducer (**Figure 2-5 a**). Available linear position transducers include potentiometers, linear variable differential transformers (LVDTs), and Hall-effect sensors. The second method measures the rotation angle of a spool wound by a sensing wire (**Figure 2-5 b**). In both cases, the operating range and resolution of the displacement transducer influence the performance of the bend sensor. For example, it is preferable to choose a linear potentiometer that has a travel length as close as possible to the maximum range of the central displacement change of the sensor.

2.2 Modeling

This section provides a sensor model that describes the relationship between bend angle and curvature of the sensor, the displacement changes of the sensing wire, and sensor output. The resultant model shows that the bend angle of the sensor and

the sensor output are linearly related within an allowable curvature range.

2.2.1 Basic Model

Figure 2-6 delivers the basic modeling concept for the relationship between bend angle and the central displacement change of the coil. Each coil pitch is represented as a rectangle with coil wire diameter, b, and outer diameter, d. The vertexes of the rectangles on the inside of the bend keep in contact as the helical coil bends, and the angle between each coil pitch uniformly increases. Total bend angle, ϕ, and length of the sensor, L, can be represented by the number of coil pitches, n:

$$\phi = \sum_{i=1}^{n} \alpha_i \tag{2-1}$$

$$L = \sum_{i=1}^{n} b \tag{2-2}$$

The small change in the central displacement between two pitches is represented as x and can be calculated using a cosine rule:

$$x = \frac{d}{2}\sqrt{2\left(1-\cos\alpha\right)} = \frac{d}{2}\sqrt{2\left(1-\cos\frac{b}{L}\phi\right)} \tag{2-3}$$

Then the central displacement changes of the helical coil along the sensor, Δl, can be derived from the summation of the displacement changes:

$$\Delta l = \sum_{i=1}^{n} x_i = \frac{dL}{2b}\sqrt{2\left\{1-\cos\left(\frac{b}{L}\phi\right)\right\}} \tag{2-4}$$

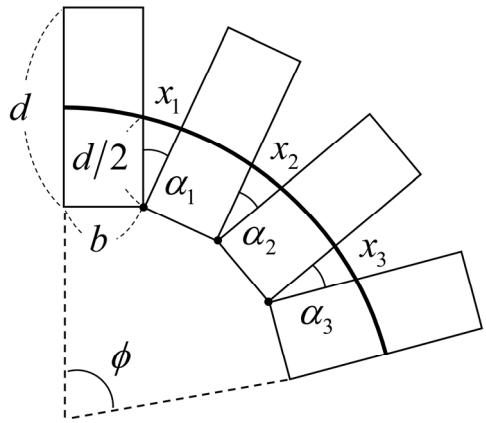

Figure 2-6 Schematic of a bent helical coil showing the displacement change of the line passing through the center of the coil. Each coil pitch uniformly bends by α, resulting in a central displacement increment of x.

Figure 2-7 illustrates the simulation result of the derived equation (2-4), showing the relationship between the central displacement change of the helical coil and the bend angle of the sensor. The simulation result indicates that it is possible to simplify the mathematical model.

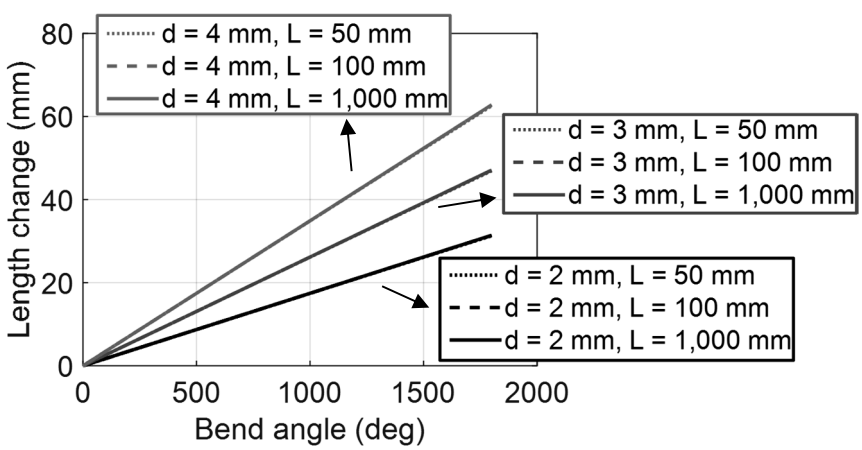

Figure 2-7 Simulation result of derived equation (2-4) when coil wire diameter b = 0.5 mm. It shows the linear relation between bend angle and the central displacement change, although (2-4) contains nonlinear functions. The curves with different length, L, are overlapped with the curves for the same coil diameter, d.

2.2.2 Effect of Curvature

To further analyze the linearity of the bend angle and the central displacement change, (2-4) can be expressed as the curvature of the sensor bend, κ:

$$\kappa = \frac{\phi}{L} \tag{2-5}$$

$$\Delta l = \frac{d}{2b\kappa}\sqrt{2\left\{1-\cos\left(b\kappa\right)\right\}}\cdot\phi = A\left(\kappa\right)\cdot\phi \tag{2-6}$$

$$A\left(\kappa\right) = \frac{d}{2}\cdot\frac{\sqrt{2\left\{1-\cos\left(b\kappa\right)\right\}}}{b\kappa} \tag{2-7}$$

Equations (2-6) and (2-7) indicate that the central displacement change ratio in regard to the bend angle, $A(\kappa)$, is a function of the design parameters (helical coil diameter, d, and coil wire diameter, b) and the bend curvature, κ. Here, there is a possibility that the bend curvature could change during sensor operation and affect the measurement of the bend angle.

Equation (2-7) can be non-dimensionalized by defining the normalized length change, Λ (length change, Δl, divided by the radius of the coil, $d/2$) and the normalized curvature, K (curvature, κ multiplied by the coil wire diameter, b):

$$\Lambda = \frac{\sqrt{2\left\{1-\cos\left(\mathrm{K}\right)\right\}}}{\mathrm{K}}\cdot\phi = \mathrm{X}\left(\mathrm{K}\right)\cdot\phi \tag{2-8}$$

The normalized change rate, X(K), can be expressed with a Taylor series (see Appendix A for more details):

$$\mathrm{X}\left(\mathrm{K}\right) = \sum_{n=0}^{\infty}\frac{1}{16^n}\frac{1}{n!}\frac{1}{\left(3/2\right)^{(n)}}\mathrm{K}^{2n} = 1 + O\left(\mathrm{K}\right)^2 \approx 1 \tag{2-9}$$

where $x^{(n)}$ is the Pochhammer symbol [57],

$$x^{(n)} \equiv \frac{\Gamma(x+n)}{\Gamma(x)} = x(x+1)\cdots(x+n-1) \tag{2-10}$$

Equation (2-9) can be approximated to 1 if the approximation error $O(\mathrm{K})^2$ is small enough.

Figure 2-8 and **Figure 2-9** show how the displacement change rate is affected by varying curvature with different design parameters. The displacement change rate is linearly proportional to coil diameter, d, as shown in (2-7), and it has a nonlinear relation to curvature and coil wire diameter, b. **Figure 2-8** shows that the displacement change rate, A, does not vary much when the coil wire diameter, b, is small. This is because the helical coil is approximated to the continuum structure with an incompressible wall inside the curve if the coil wire diameter is small enough relative to the coil diameter. In this case, the displacement change rate can be considered constant regardless of the bend curvature along the sensor. **Figure 2-9** shows that even in an extreme curvature condition, $\mathrm{K} = 0.5$ (e.g., $\kappa = 1000\ \mathrm{m}^{-1}$, $b = 0.50$ mm), the change rate only varies by 1.0%. The ratio of the coil diameter and the wire diameter illustrated here is within the proper range of practical design parameters because a high coil wire diameter increases the stiffness of the sensor, which is not desirable.

The effective displacement change rate, A_{eft}, which can be used as a sensor gain, can be derived with the approximation in (2-9):

$$A_{eft} = \frac{d}{2} \cdot \mathrm{X}(\mathrm{K}) \approx \frac{d}{2} \tag{2-11}$$

Equation (2-11) indicates that geometric model in **Figure 2-6** can be simply approximated with a perimeter calculation $\Delta l = d/2 \times \phi$ with the small normalized curvature. It can be used for the model-based sensor gain before precise calibration of the bend sensor. The accuracy of the derived model will be compared with

experimental results in **Chapter 2.4.2**.

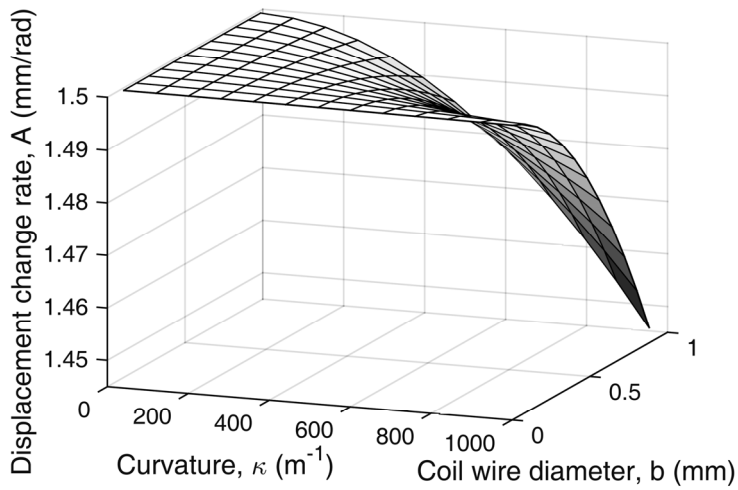

Figure 2-8 Simulation result showing how the displacement change rate varies with the bend curvature, κ, and the coil wire diameter, b, when $d = 3$ mm. The displacement change rate can be assumed to be constant within a certain range of design parameters and curvatures.

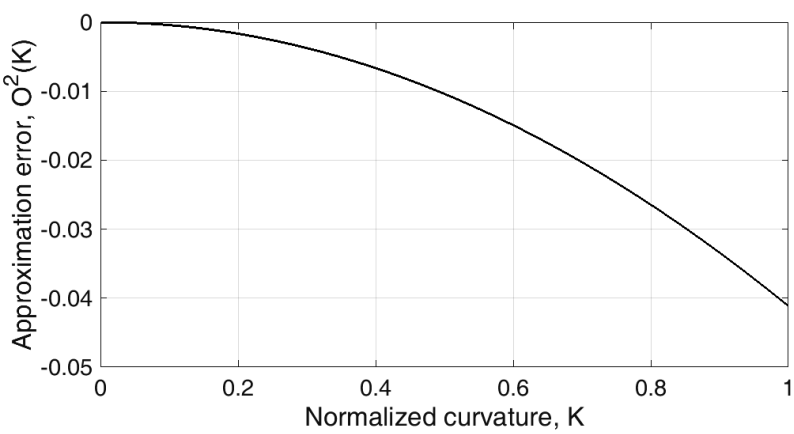

Figure 2-9 Simulation result of the approximation error depending on the normalized curvature. Large variation of the normalized curvature during sensor operation can lead to measurement error, but not by much—the change rate varies within 1.0% with extreme conditions when K = 0.5 ($\kappa = 1000$ m^{-1} when $b = 0.50$ mm). This can be approximated to a constant value during actual conditions of sensor operation.

2.2.3 Advanced Model

The gap between the sensing wire, the Teflon® tube, and the helical coil together with the cross-sectional shape of the coil wire should be considered for a more accurate description of the relationship between the bend angle of the sensor and the central displacement change.

(1) Gap Between Parts

Gaps between the sensing wire, the Teflon tube, and the helical coil are necessary to prevent excessive friction between these parts and to ensure that the sensing wire slides well with the angle change of the sensor. Thus the sensing wire does not retain its central position inside the coil, and it contacts the inner wall as the helical coil bends when the sensing wire is tensioned. As a result, the effective distance between the sensing wire and the outer wall of the helical coil, d_{eft1}, is smaller than the radius of the helical coil. This is depicted in **Figure 2-10** and described in the following equation:

$$d_{eft1} = b + b_{tube} + \frac{1}{2} d_{wire} \tag{2-12}$$

where b, b_{tube}, and d_{wire} are the wall thickness of the helical coil, the wall thickness of the Teflon tube, and the diameter of the sensing wire, respectively.

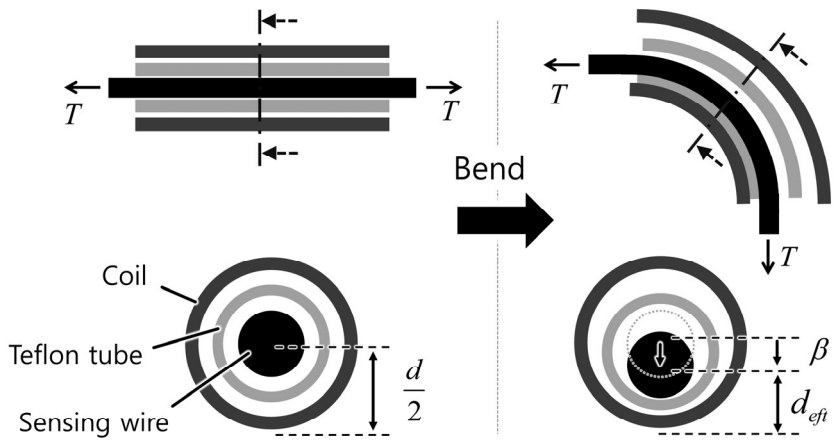

Figure 2-10 The sensing wire does not maintain its position in the center of the coil because there are gaps between the sensor's parts. The effective distance between the center of the sensing wire and the outside wall of the helical coil, d_{eft}, should be considered when calculating the sensor gain derived in **Chapter 2.2.1**.

(2) Shape of the Cross Section

In the helical coil model in **Figure 2-6**, the coil wire was assumed to have a square cross-sectional shape for purposes of simplification. However, the actual distance between the contact point of each coil pitch and the sensing wire decreases if the cross section of the coil wire is circular in shape. **Figure 2-11 b** shows a close up of the contact point between two pitches with rounded ends. The modified distance, d_{eft2}, can be approximated to a constant value if the angle between two pitches, α, is small enough:

$$\lim_{\alpha \to 0} d_{eft2} = \frac{d}{2} - \frac{b}{2} \tag{2-13}$$

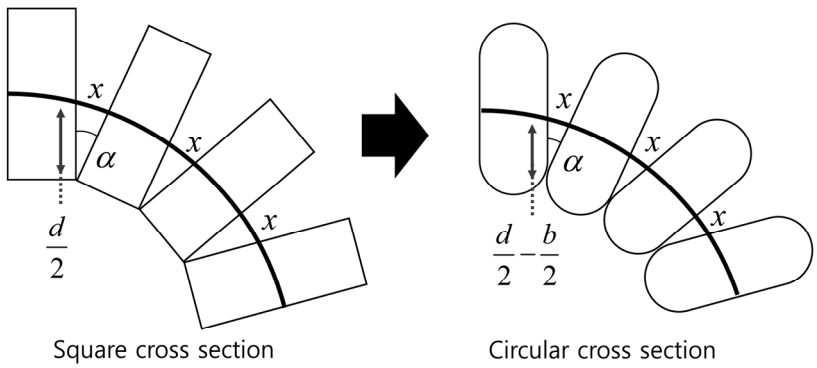

(**a**)

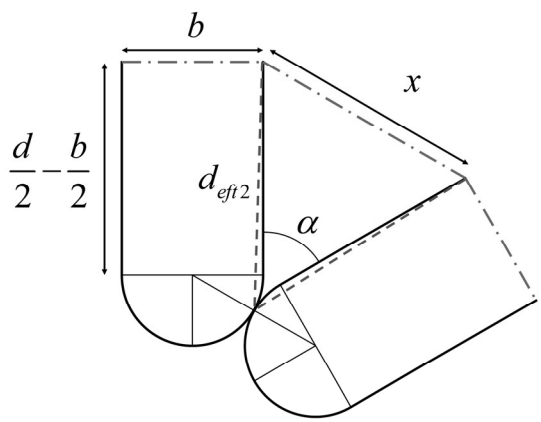

(**b**)

Figure 2-11 The model should be modified for a coil wire with a circular cross-sectional area for more accurate modeling. (**a**) Model modification for a circular cross-section; (**b**) Close view of the contact point between the two coil pitches.

2.2.4 Sensor Gain

The resultant sensor gain, which transforms the measured position of the sensing wire to the bend angle of the sensor, can be derived from the considerations described in **Chapters 2.2.1**–**2.2.3**:

$$\frac{\phi}{\Delta l} = \frac{1}{\left(\frac{b}{2} + b_{tube} + \frac{d_{wire}}{2}\right)} \tag{2-14}$$

$$\frac{\phi}{\Delta \theta} = \frac{r}{\left(\frac{b}{2} + b_{tube} + \frac{d_{wire}}{2}\right)} \tag{2-15}$$

Equations (2-14) and (2-15) describe a sensor gain with a linear position transducer and a rotational angle transducer, respectively. The operating range of each position transducer should be determined considering the range of motion of the bend sensor to increase the resolution and the sensitivity of the bend sensor. A small-diameter spool increases the ratio of spool rotation per sensor bend, which will increase resolution and sensitivity but decrease the sensing range.

2.2.5 Axial Force Robustness

The helical coil can stretch, causing a sensing error, if an axial force is exerted on the sensor, as shown in **Figure 2-12**. Stretching of the helical coil along the axial axis is prevented by the tension of the sensing wire (T_{wire}) and the initial extension force (F_I) of the helical coil. However, when the external axial force, F_{axial}, is higher than the summation of the wire tension and the initial extension force, a sensing error results for the bend sensor. The robustness of the axial force can be increased by choosing a helical coil with a higher initial tension (generally proportional to wire diameter and stiffness) and by increasing the pre-tension of the sensing wire.

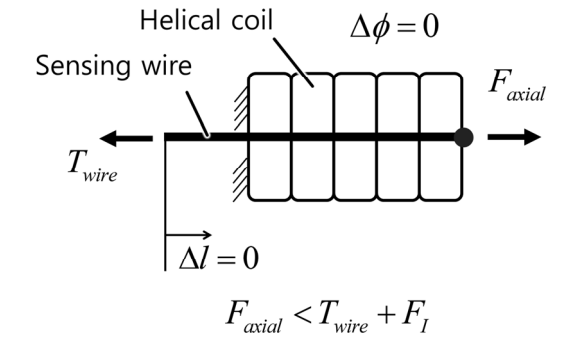

(**a**)

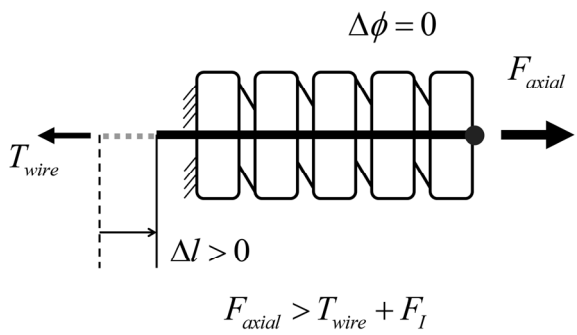

(**b**)

Figure 2-12 Axial force robustness. (**a**) Safe region; (**b**) A sensing error occurs when the external axial force is higher than the wire tension and the initial tension.

2.2.6 Axial Rotational Robustness

Axial rotation of the helical coil can cause geometrical changes in the sheath. The counter-clockwise rotation shown in **Figure 2-13 a** further coils the sheath, which increases the total length of the sheath, as if the sensing wire were being pulled by the sensor's bending:

$$\Delta L = \frac{b}{2\pi}\varphi_{axial} \tag{2-16}$$

The length change of the sheath can be represented as shown in (2-16), where φ_{axial} is the axial rotation angle of the sheath along the sensor in the radian. As an

example, 90° rotation of the sheath clockwise will increase sheath length 0.125 mm, causing a measurement error of 4.9°. However, this effect is much smaller in the real system because there is friction between each coil pitch and the diameter of the helical coil does not change uniformly along the sheath. If the axial rotational robustness is important on the specific application, torque coils [58]—that is used to transmit the torque for the endoscopic devices and the catheters and has high torsional stiffness—can be used instead of the standard extension spring.

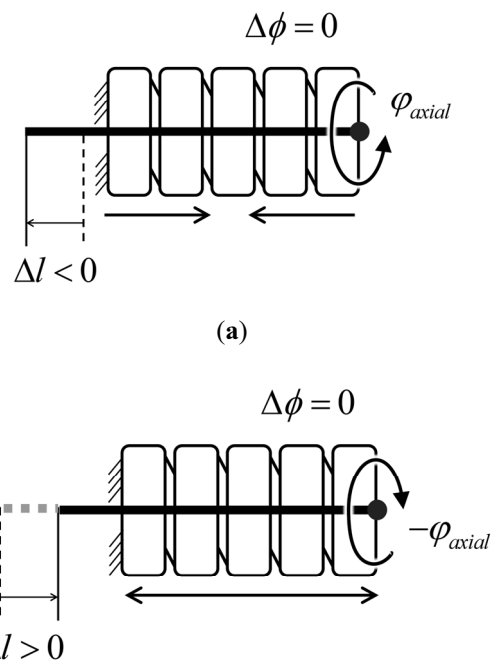

Figure 2-13 Axial rotation along the helical coil causes only a small length change of the helical coil. The sheath (**a**) contracts with counter-clockwise rotation and; (**b**) extends with clockwise rotation.

2.3 Characteristics of the Proposed Bend Sensor

The proposed sensor has several characteristics that differentiate it from Flex sensors and optical-fiber based sensors. The properties of these sensors are compared in **TABLE 1** and **Figure 2-14**.

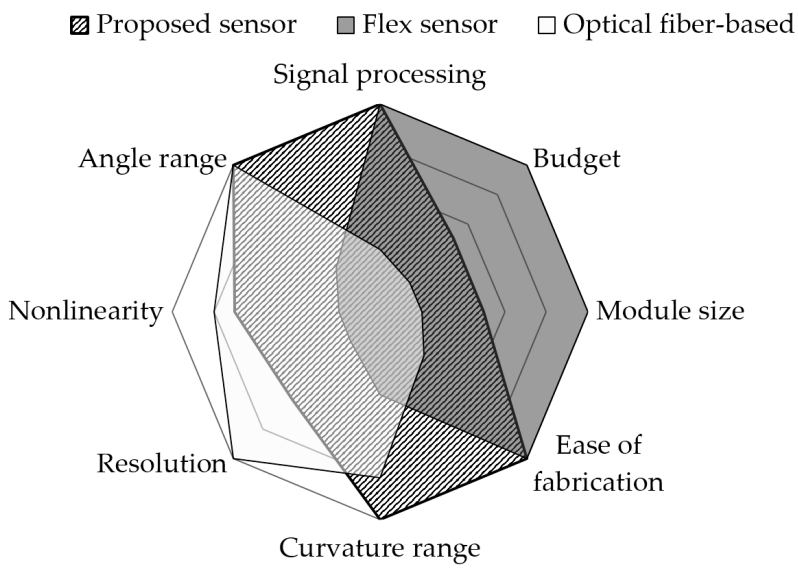

Figure 2-14 Comparison of the representative characteristics of the proposed sensor (middle area with the patterns), the Flex sensor (right dark area), and the optical fiber-based sensor (left bright area).

TABLE 1. COMPARISON OF SENSOR CHARACTERISTICS.

Property	Proposed Sensor	Flex Sensor	Optical Fiber-Based Sensor
Size	Thin	Wide	Very thin
Length	Unlimited [1]	Fixed	Unlimited [1]
Measurand	Position	Electrical resistance	Light [2]
Module size [3]	Medium	Compact	Large
Signal processing	Simple	Simple	Complicated
Fabrication	Simple	Off the shelf	Complicated
Cost [4]	Cheap	Cheap	Expensive
Directionality	Any-direction	Uni-/bi-direction	Any-direction
Curvature range	Wide	Narrow	Restricted
Stiffness [5]	Adjustable	Fixed	Depends on fiber
Nonlinearity	Low	High	High
Resolution [6]	High	Low	High

[1] Theoretically, the length can be increased infinitely, but unmodeled properties can affect the characteristics of sensors if they are lengthened a great deal; [2] Measures intensity, phase, wavelength, and polarization of light. An interrogator is necessary for spectrum analysis; [3] Size of the device that detects the measurand. It can be a Hall-effect sensor or a potentiometer (as in the proposed bend sensor) or a photodiode (as in an optical fiber-based sensor); [4] Costs for the proposed sensor in US dollars: $3.60 for the potentiometer version and $52.60 for the Hall-effect sensor version. Flex sensor: approximately $10 depending on size. Optical fiber-based sensor: Approximately $12,000, the manufacturer's suggested retail price for the interrogator (PXIe-4844; National Instruments, Corp., Austin, USA); [5] Bending stiffness of the optical fiber depends on the material and the inner and outer diameter of the fiber; [6] Resolution of the proposed sensor depends on the performance of the position measurement of the sensing wire and is bounded by mechanical properties (friction and backlash). On the other hand, the resolution of the optical fiber-based sensor is closely related to its fabrication process and sophisticated signal processing.

(1) Low Cost

The proposed sensor is made of low-cost materials and can be manufactured easily without specialized fabrication techniques. The sensor can be assembled with off-the-shelf parts within 15 min.

(2) High Degrees of Freedom for the Sensor's Dimensions

The dimensions of the sensor are determined by the diameter and length of the helical coil. Thus the size of the sensor can be easily and finely adjusted because there is a wide range of choices for the diameter of the extension spring, and the spring can be cut to the desired size.

(3) Intuitive and Easy to Use

The principle of the proposed sensor is the mechanical conversion of information about bending to information about displacement of the sensing wire. Thus the measurand of the proposed sensor is the displacement of the sensing wire. Because there are various options for the displacement transducer, the user can select one based on their preferences. No complex signal processing or specialized data acquisition device is required because the measurement from the displacement transducer is proportional to the bend angle of the sensor.

(4) No Directionality

This sensor can detect bending in any direction because the helical coil's shape and properties are symmetrical along the axial line. Moreover, because the sensing wire is placed in the center of the helical coil, the axial displacement of the sensing wire changes with bending in any direction along the helical coil.

(5) Measures the Accumulated Bend Angle

This sensor cannot detect the direction of bending or the specific location where bending occurs because it only measures one-degree-of-freedom information, that is, central displacement changes of the coil. However, it can detect the accumulated bend angle along the sensor, as depicted in **Figure 2-4**, because any local bending along the helical coil causes a central displacement change along the sheath.

(6) Large Sensing Range

The sensor's physical sensing range is restricted only by the maximum bend curvature of the helical coil that does not cause permanent strain on the sheath. Widely used extension springs made of spring steel or stainless steel have high elasticity and can enable large curvature of the sensor.

(7) Theoretical Performance

The theoretical performance of the sensor depends on the design parameters and performance of the sensor that is used to measure the displacement change of the sensing wire. The Hall-effect sensor provides high performance for both a linear and a rotary configuration. An incremental Hall-effect encoder with 8192 counts per resolution can provide 0.2° resolution for a bend sensor consisting of a 3-mm outer diameter helical coil and a 6-mm diameter spool. A potentiometer is an economical option that provides sufficient performance.

(8) Bending Stiffness

The bending stiffness of the sensor is determined by the stiffness of the helical coil and the tension of the sensing wire. A large spring constant and a large-diameter coil lead to high bending stiffness of the sensor because energy is required to elongate the spring coil, as shown in **Figure 2-6**. Also, greater tension in the sensing wire and a larger helical coil diameter contribute to the restoring force from the

sensing wire, which increases the bending stiffness. Bending stiffness increases as the sensor bends if a spring is used to provide tension on the sensing wire. Because bending stiffness can be modeled as a function of design parameters, a bending stiffness profile can be adjusted by changing the radius of the spool and the constant of the linear spring. An actuator can be used as a tensioning device to provide more degrees of freedom for the stiffness profile or to allow variable sensor stiffness.

(9) Environmental Robustness

The absence of electronic components on the bending part ensures good robustness to environmental conditions. Stainless steel, Teflon, and aramid, which are used in the helical coil, liner, and sensing wires, respectively, have high chemical resistance and thermal resistance (the melting point of Teflon and aramid is 327 °C and 500 °C, respectively). Because the sensor is mechanically operated, it is immune to electromagnetic interference and moisture, allowing it to be used even when submerged in boiling water or high-temperature oil.

2.4 Prototype Development

2.4.1 Fabrication Considerations

A prototype of the proposed bend sensor was developed using a spool to provide internal tension and measure the position change of the sensing wire (**Figure 2-15** and **Figure 2-16**). A miniature extension spring was attached between the spool and the frame to provide a restoring torque to the spool. A Hall-effect angle sensor and a magnet were placed to measure the rotational angle change of the spool. The Hall-effect sensor provides higher resolution than a rotary potentiometer, but it is more expensive. The frame of the sensing part was fabricated using a three-dimensional (3D) printer. A continuous length extension spring (Φ3.0 mm × Φ2.0 mm × 500 mm—Φ indicates diameter) whose coil wire had a circular cross section was used as

the helical coil of the bending part. An extension spring can be cut to the desired length of the sensor, and it is easy to find an off-the-shelf continuous length spring up to 1 m long on the market.

A Teflon tube was used inside the coil to reduce friction along the sensing wire. Two Teflon tubes with different diameters (Φ1.38 mm × Φ1.88 mm and Φ1.40 mm × Φ0.90 mm) were fitted together to increase the wall thickness and place the sensing wire as close as possible to the center of the coil, which increases the ratio of the central displacement change to bending of the sensor. The sensing wire and Teflon tube should not be tightly fit because that causes too much friction, resulting in hysteresis of the sensor. Using a 0.9 mm inner diameter Teflon tube with a 0.45 mm diameter Dyneema (Royal DSM, Heerlen, Netherlands) wire ensures that the wire moves smoothly. A 3D-printed end-cap was attached to both ends of the helical coil to provide rigidity and to connect the coil to the frame and fix the end of the sensing wire. The sensing wire was built with braided Dyneema wire (Φ0.45 mm) because this material has high modulus (109–132 GPa tensile modulus [59]), ensuring that the wire did not elongate and violate the assumptions of the derived model. Dyneema wire is flexible and easily wound around a small-diameter spool (6 mm), and it does not lose contact with the spool and the inner wall of the Teflon tube. Metal wires can lose contact with the surface of a spool because their bending stiffness is higher than that of polymer wires. Also, Dyneema wire is reported to have a small friction coefficient when used with Teflon tubes (a friction coefficient of 0.055 compared to 0.092 for steel [19], [24]).

All of the materials used to fabricate the sensor are inexpensive, enabling the manufacture of a low-cost bend sensor. The total price of the components used, exclusive of the displacement sensing element, was $2.60 US dollars. This study used a Hall-effect sensor module with an embedded analog to digital converter (ADC), which is somewhat expensive for fast prototyping. Using Hall-effect sensor

ICs with their own electronics would further reduce the manufacturing cost. The total cost of the sensor could be reduced to $3.60 US dollars if a rotary potentiometer is used instead of a Hall-effect sensor. The specifications and prices of the components are listed in **TABLE 2**.

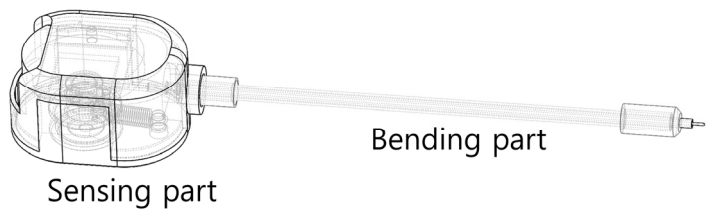

(**a**)

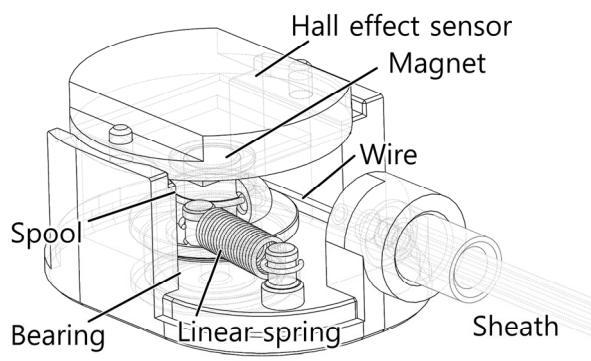

(**b**)

Figure 2-15 Computer-assisted design (CAD) model of the bend sensor prototype. (**a**) Overall view of the sensor consisting of a sensing part and a bending part; (**b**) Close view of the sensing part, which provides tension to the sensing wire and measures its position.

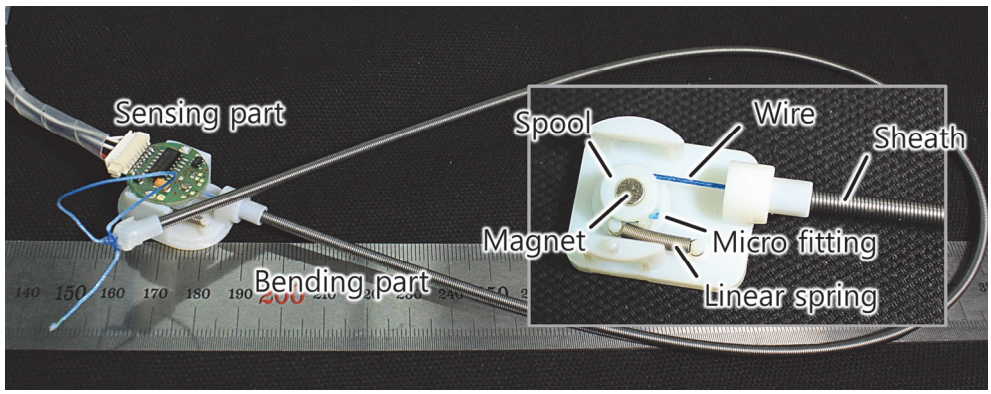

Figure 2-16 Developed prototype of the bend sensor that consists of the sheath, sensing wire, supporting structure, spool, linear spring, and rotational encoder.

TABLE 2. SPECIFICATION AND PRICE LIST OF THE PROTOTYPE COMPONENTS (US DOLLARS).

Component	Specification	Price
Helical coil	Extension spring: Φ3.0 mm × Φ2.0 mm × 500 mm	$1
Lining	Outer Teflon tube: Φ1.38 mm × Φ1.88 mm; Inner Teflon tube: Φ1.40 mm × Φ0.90 mm	$0.2
Wire	Braided Dyneema wire: Φ0.45 mm	$0.1
Structure	3D printed with VeroWhitePlus™ (Objet Connex; Stratasys Ltd., Eden Prairie, USA)	$1
Spring	Miniature extension spring	$0.3
Displacement sensor	Hall-effect sensor: RMB20IC13BC10 (RLS; 8192 pulses per turn, ±0.5° accuracy, 0.18° hysteresis, onboard RC filter with 720 Hz cut-off frequency for sine and cosine signal of magnetic flux); Magnet: Φ4 mm × 4 mm	$50

2.4.2 Potentiometer Version

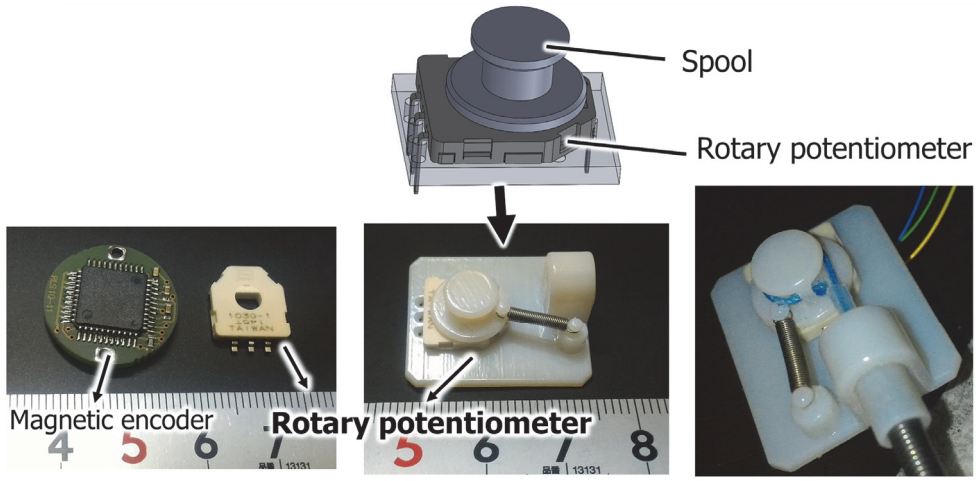

Figure 2-17 Sensing part of the sensor prototype using the rotary potentiometer (3382G-1-103G, 2% nonlinearity, Bourns, Inc.).

The proposed sensor can be designed and manufactured with a more affordable price using a rotary potentiometer ($1.0 ea. for 1,000 units) instead of the magnetic encoder. The rotary potentiometer has an embedded bushing inside the unit that eliminates the requirement for the bearing on the structure so it could simplify and miniaturize the sensor unit. However, there is a possibility of the hysteresis behavior of the sensing system that uses rotary potentiometer because of the increasing friction of the bushing inside the rotary potentiometer. Furthermore, the temperature coefficient of the potentiometer should be taken into account to avoid the undesirable error originated from the temperature change.

2.4.3 Zero Calibration

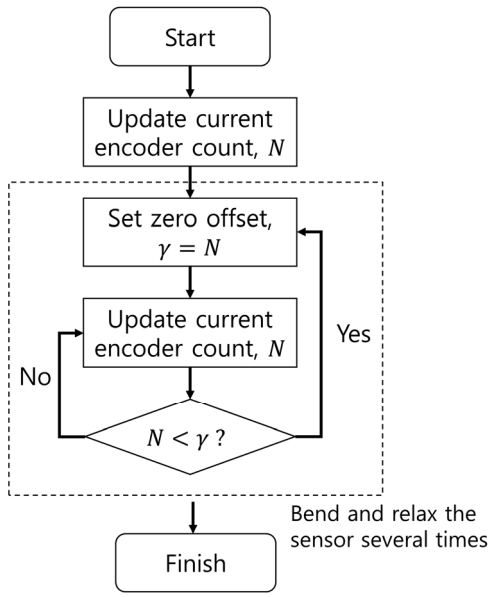

Figure 2-18 Zero calibration algorithm for the bend sensor that uses the incremental encoder for the displacement measure of the sensing wire.

There should be a reference point for the sensor signal that uses the incremental encoder for the displacement measure of the sensing wire because the incremental encoder can only measure the relative displacement change of the sensing wire. The zero-bend of the sensor can be set to be a reference bend point since the sensor cannot have a minus bend angle and the zero-bend should be the lowest value of the sensor signal. Based on this idea, a zero calibration algorithm (**Figure 2-18**) is developed and implemented on the signal processor of the sensor prototype to ease the zero calibration process. It utilizes a basic idea that the zero-bend is the lowest signal that the sensor can generate. The proposed algorithm constantly seeks the lowest value that the sensor measures and set the found value to be a zero offset of the sensor. On the first stage of the calibration period, the sensor can be bent and relaxed several

times so that the zero calibration algorithm could found the sensor signal that matches to the zero-bend of the sensor. In addition, the proposed algorithm could be run consistently during the sensor operation to reject the unexpected offset change of the sensor. The simulation result in **Figure 2-19** shows the zero-calibrated signal converges to the actual measurement of the bend angle with the proposed calibration algorithm

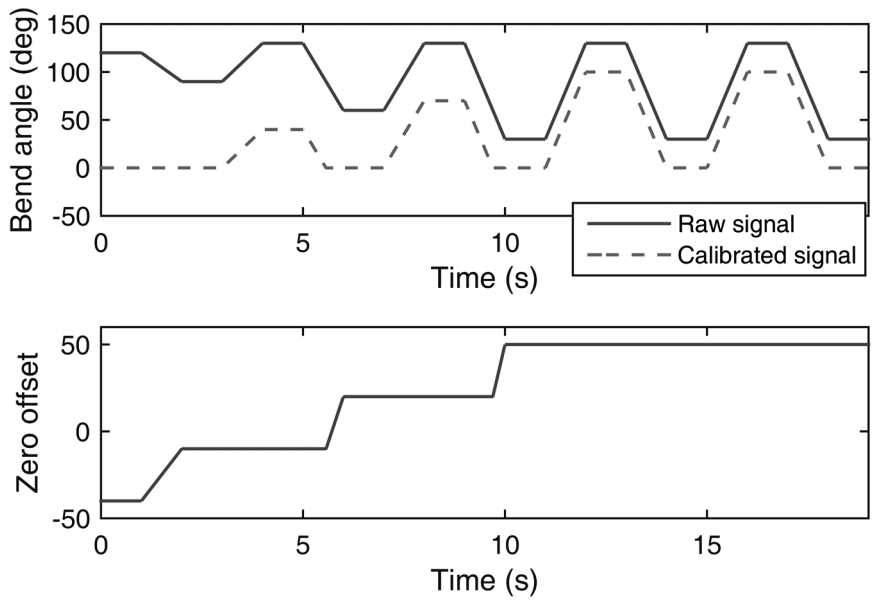

Figure 2-19 Simulation result of the zero calibration algorithm for the bend sensor.

2.5 Experiments

Two experiments were conducted to determine the output response of the sensor in terms of the reference bend angle and curvature. First, a quasi-static experiment was conducted to compare the continuous response of the sensor at a bend angle from 0° to 120° using an external reference angle sensor. Limitation of the bend angle range in the quasi-static experimental setup encouraged a second experiment

that permitted large deflections. Finally, a static experiment was conducted to determine the response of the sensor to large deflections (0° to 450° bend angle) with different bend curvatures (κ = 26.7 m^{-1}, 40.0 m^{-1}, and 80.0 m^{-1}) using bending brackets. In addition, the robustness experiment for the sensor is conducted to see the signal change if the sensor is subjected to the repetitive bending.

Hall-effect sensors with an incremental quadrature pulse output (RMB20IC; RLS, Komenda, Slovenia, accuracy ±0.7°, hysteresis 0.18°) and a magnet (Φ4 mm × 4 mm) were used to measure the spool angle of the bend sensor and the reference angle. The output signal of the sensor and the reference angle were acquired with a data acquisition device (cRIO-9082, National Instruments Corp.) with a differential digital input module (NI 9411, National Instruments Corp.). Data was saved on a host PC using an Ethernet interface with a 1-kHz sampling frequency. No filter was applied after data acquisition because the Hall-effect sensor module included an embedded ADC with filters. All of the brackets used in both experiments were made with a 3D printer (Object Connex, Stratasys Ltd.).

2.5.1 Quasi-Static Experiment

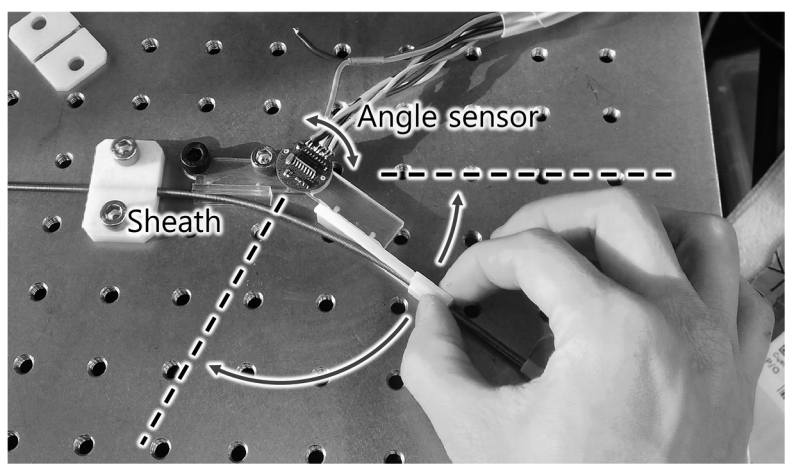

Figure 2-20 Setup for the quasi-static experiment. The sensor sheath was constrained to the desired bend angle, and the setup was moved by hand.

Figure 2-20 shows the experimental setup for measuring the sensor signal with a continuous bend angle change from 0° to 120°. To set the desired rotation angle, a rotating bracket with a reference angle sensor was moved by hand. The moving bracket was rotated from 0° to 120° and 120° to 0° three times sequentially.

Figure 2-21 and **Figure 2-22** show the experimental results of the quasi-static experiment in the time domain and the reference angle domain, respectively. Data was plotted to compare the reference angle, the model-based sensor output, and the calibrated sensor output. The model-based sensor output was calculated from the derived sensor model, the design parameter of the prototype, and the raw signal from the Hall-effect sensor. It shows the modeling accuracy of the sensor model derived in **Chapter 2.2**. The result shows that the model-based sensor output was lower than the actual reference angle, with a root mean square error (RMSE) of 8.42°. This means that the actual displacement change of the sensing wire is lower than for the derived model because of the uncertainty of the model. However, **Figure 2-22 a** shows that the sensor output signal has high linearity and can be calibrated with a linear function to increase accuracy. Linear regression (ordinary least squares) without the intercept term was conducted on the raw signal of the sensor and the reference angle to calibrate the developed sensor. The calibrated signal was plotted with a red dotted line in **Figure 2-21** and **Figure 2-22**. The RMSE of the calibrated signal was reduced to 5.15°, which is 4.29% of the full scale (120°). The R-square value (coefficient of determination) of the calibrated sensor output is 0.9887, which ensures the sensor to be used with a linear calibration function. However, the sensor signal can be calibrated with polynomials to further increase sensing accuracy.

The results show low levels of hysteresis with a maximum offset of about 3°. The sensor's hysteresis may have originated in wire friction. It can be compensated for with hysteresis modeling [8]–[10], [23] or minimized by hysteresis analysis and optimization of the design parameter of the sensor.

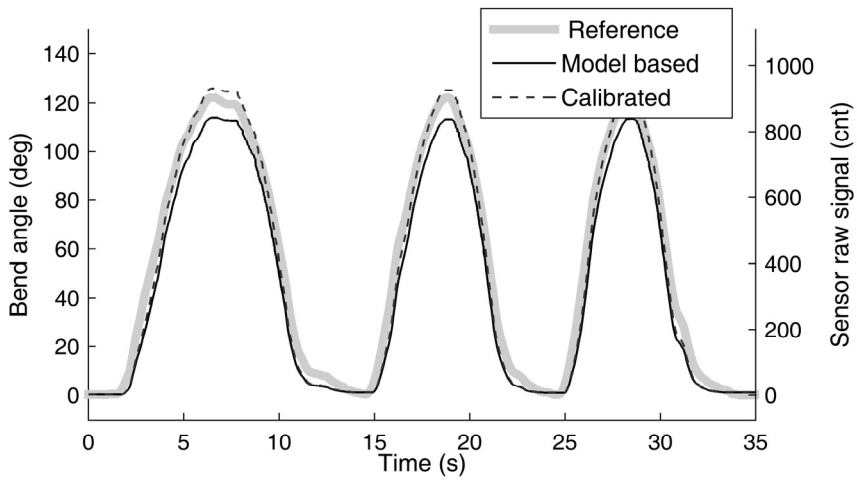

(**a**)

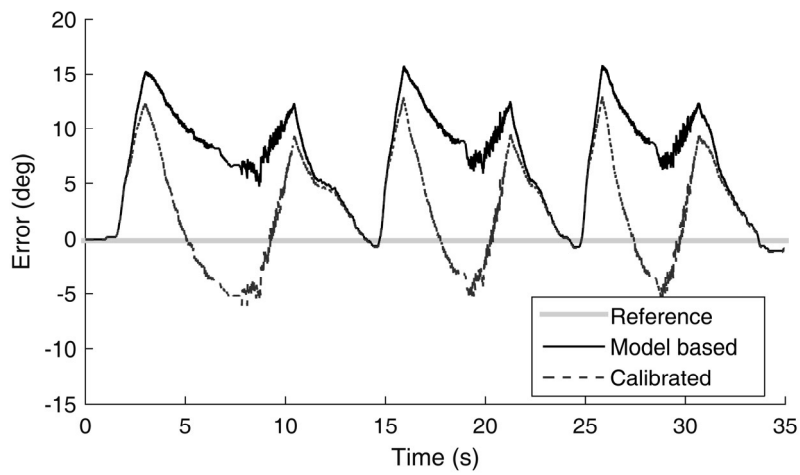

(**b**)

Figure 2-21 Results for the quasi-static experiment in the time domain. (**a**) Reference angle (gray thick line), model-based sensor output (black solid line), and calibrated sensor output (gray dotted line) in the time domain; (**b**) Sensing error of model-based sensor output (black solid line) and calibrated sensor output (gray dotted line) in the time domain.

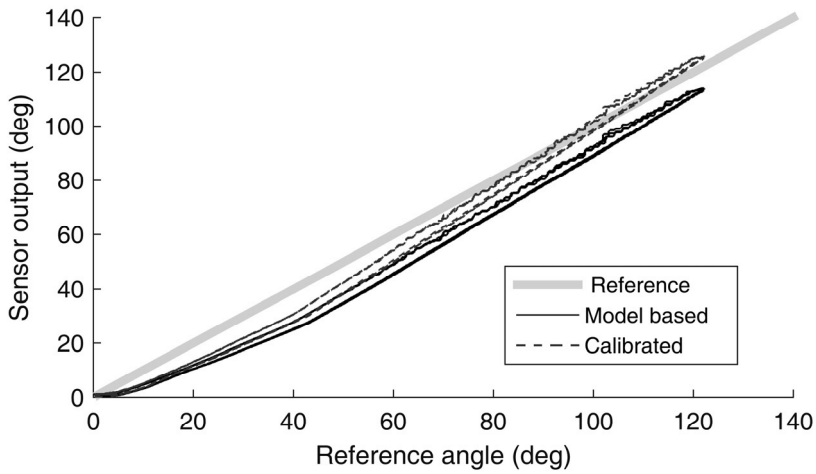

(**a**)

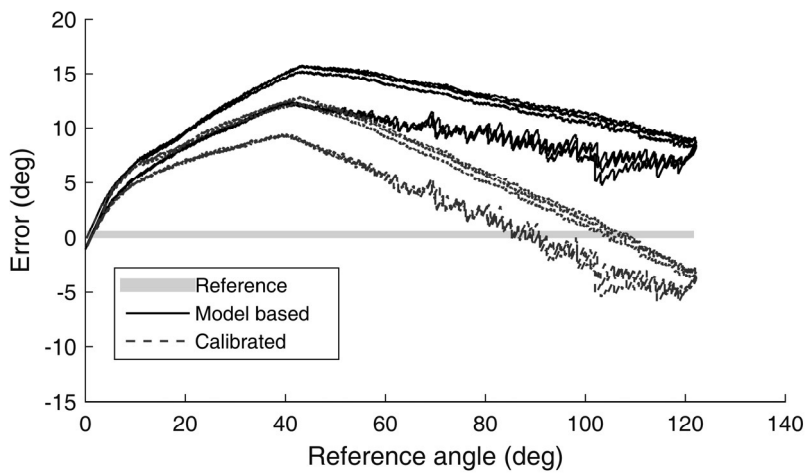

(**b**)

Figure 2-22 Results for the quasi-static experiment in the reference angle domain. (**a**) Reference angle (gray thick line), model-based sensor output (black solid line), and calibrated sensor output (gray dotted line) in the reference angle domain; (**b**) Sensing error of model-based sensor output (black solid line) and calibrated sensor output (gray dotted line).

2.5.2 Large Static Deflection Experiment

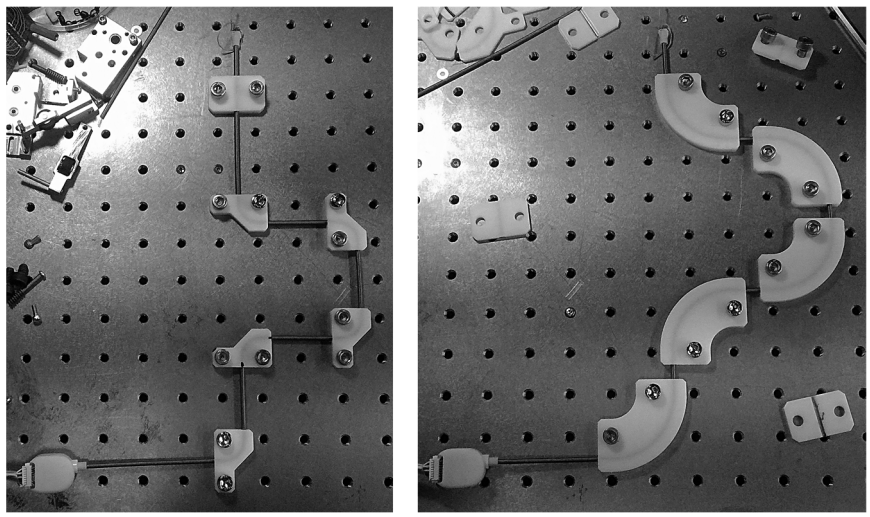

(**a**) (**b**)

Figure 2-23 Setup for the large static deflection experiment using a 90° bending bracket with three different curvatures. (**a**) $\kappa = 80.0\ m^{-1}$; (**b**) $\kappa = 26.7\ m^{-1}$.

A large static deflection experiment was conducted to determine the sensor's response when subjected to large bend angles of different curvatures. Five brackets having a 90° bend angle were placed onto a breadboard for experiments with three different bend curvatures ($\kappa = 26.7\ m^{-1}$, $40.0\ m^{-1}$, and $80.0\ m^{-1}$), as shown in **Figure 2-23**. Sensor output was measured with 11 different bend angles by adding and subtracting brackets from 0° to 450° and 450° to 0°.

Figure 2-24 shows the result of the large static deflection experiment. Data was plotted with different curvatures, and the sensor signal was compared to the reference angle. Overall, it was found that the sensor output shows a linear increment with an increasing bend angle up to 450°, with R-square values of 0.9959, 0.9968, and 0.9969 for the calibrated sensor output for the three different curvatures. Also, the tendency of the sensor output was not affected by the bend curvature, which was the expected result from the modeling and simulation.

The sensor output based on the model is still lower than the reference angle as in the quasi-static experiment, with RMSEs for the model-based sensor output of 38.05°, 37.90°, and 49.39° for the three curvatures. Additionally, the RMSEs of the calibrated sensor output are 9.05°, 8.10°, and 8.29° for the three curvatures, which represents a 2% maximum error of the full sensing range. The sensing range of this experiment was restricted by the length of the sensor. A longer bend sensor would have allowed a larger bend angle to be measured.

The experimental results show some unmodeled measurement error. The expected error of the proposed sensor can be considered in terms of thermal properties and mechanical precision. The helical stainless steel coil had a positive thermal expansion coefficient ($\alpha_{ss} = 10.1 \times 10^{-6} - 17.3 \times 10^{-6}$ K^{-1}), while Dyneema wire had a negative coefficient ($\alpha_{dyneema} = -12 \times 10^{-6}$ K^{-1}) [59]. This resulted in a 0.011–0.015 mm displacement error and a 0.65–0.86° measurement error per unit temperature (K^{-1}) for the 500 mm length of the sensor. However, the huge temperature change that occurred during sensor measurement is not typical, and the temperature effect described above is much smaller than the temperature effect of Flex sensors (±30% resistance tolerance) [29]. The precision of parts and the assembly process is another factor affecting the measurement error because the principle of the sensor is the mechanical conversion of the bend angle to the displacement change. Improper finishing of the sensing wire can lead to a dead signal zone or a zero offset change of the sensor. Also, the tilt axis of the spool can affect sensor gain depending on the bend angle, as shown in the tendency of an error in **Figure 2-22**. In addition, friction between the sensing wire and Teflon tube can affect the nonlinearities of the sensor signal, although the tension of the sensing wire is kept as low as possible to reduce the friction effect. Furthermore, during long-term use of the sensor, sensor contamination can affect its friction and hysteresis characteristics.

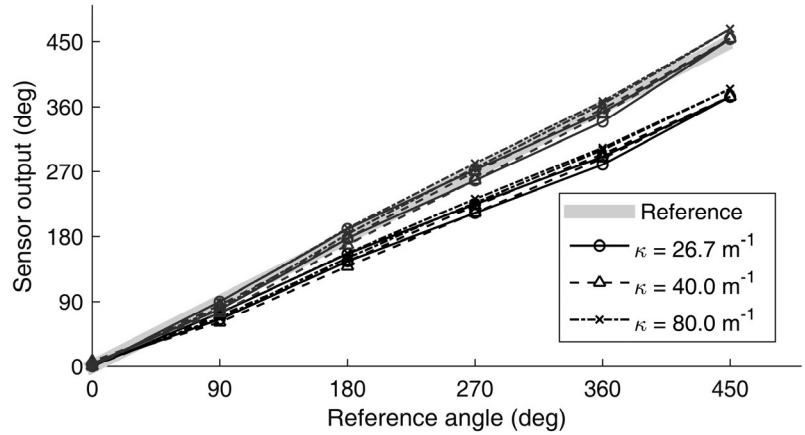

(**a**)

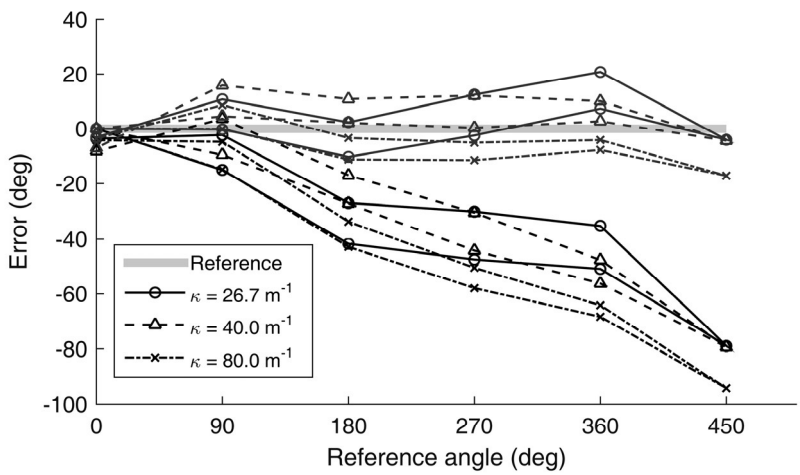

(**b**)

Figure 2-24 Experimental results showing the output signal with various bending angles and curvatures. (**a**) Sensor output with difference curvatures showing model-based output (black) and calibrated output (gray) with three different curvatures; (**b**) Sensing error with different curvatures, showing model-based output (black) and calibrated output (gray) with three different curvatures.

2.5.3 Robustness

The robustness of the proposed bend sensor is tested to see the signal change with the repetitive bend and to determine the lifetime of the sensor. A servo motor is attached to the quasi-static experimental setup to provide a consecutive bend of the bend sensor from 0° to 90° with the period of 4 s and speed of 10 RPM. The measured reference angle and the signal from the sensor were recorded two periods per ten minutes during 12 hours.

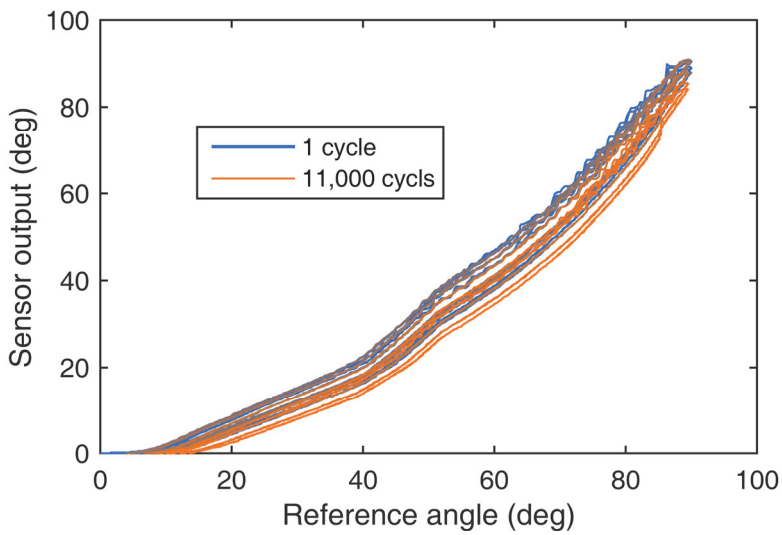

Figure 2-25 Experimental result of the bend sensor robustness showing the sensor output with the reference angle from 1 cycle (blue line) to 11,000 cycles (orange line). The output signal decreases with the repetitions.

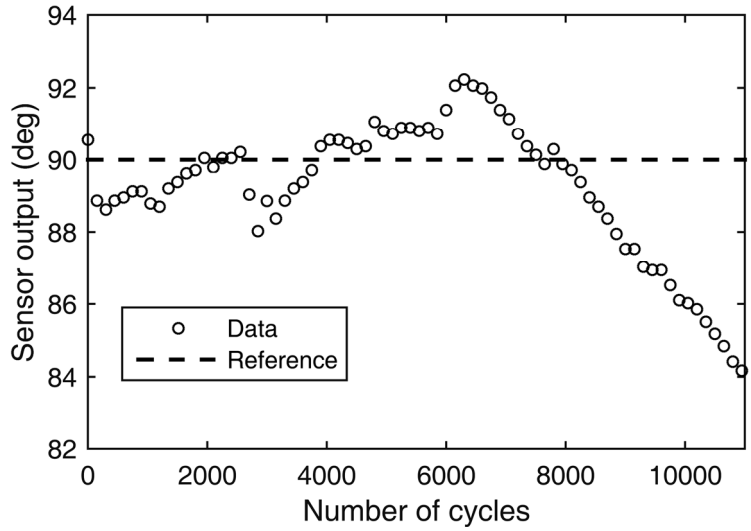

Figure 2-26 Experimental result of the bend sensor robustness showing the sensor output on the reference angle 90° with the repetitions.

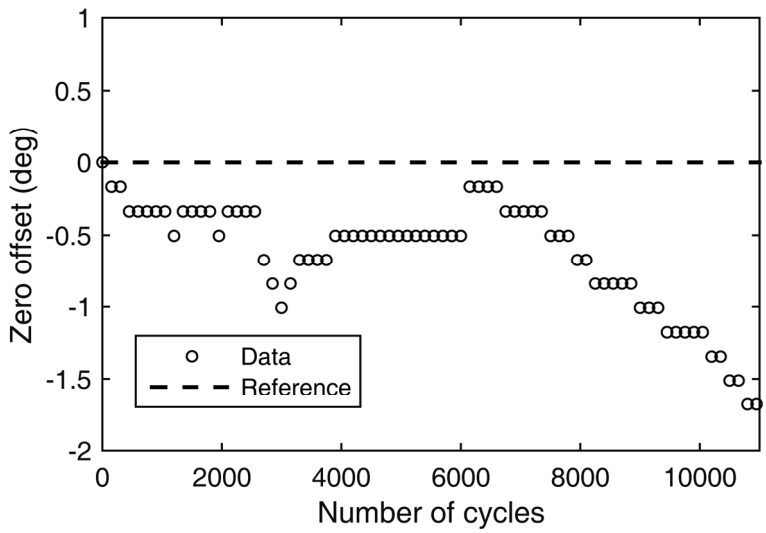

Figure 2-27 Experimental result of the bend sensor robustness showing the zero-offset change with the repetitions.

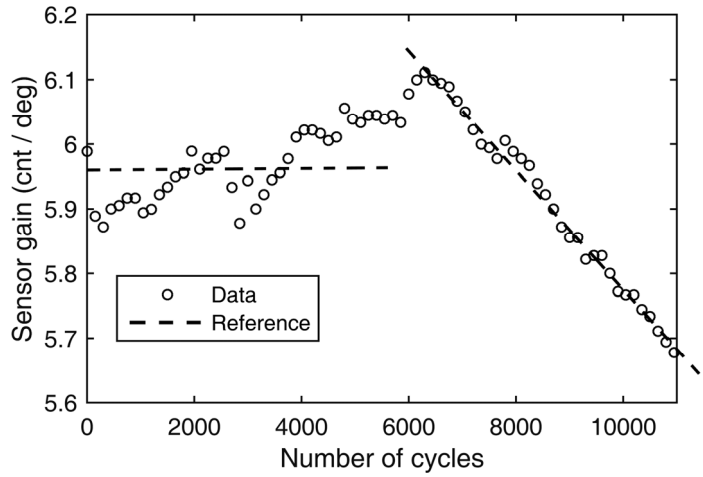

Figure 2-28 Experimental result of the bend sensor robustness showing the sensor gain (cnt/deg) change with the repetitions. It remains consistent until 6,150 cycles and starts to decrease with the rate of -9.57×10^{-5} cnt/deg per cycle.

Figure 2-25 shows the output signal of the bend sensor with the repetitions from 1 to 11,000 cycles. There exists some hysteresis in the relation between the reference angle and the output signal of the sensor which is originated from the characteristics of the sensor itself and the discrepancy between the reference angle of the experimental setup and the actual bend angle of the sensor. The overall shape of the curve representing the reference angle and the sensor output remained consistent during the repetitions. **Figure 2-26**, **Figure 2-27**, and **Figure 2-28** show the sensor output at the reference angle 90°, zero-offset at the reference angle 0°, and the sensor gain respectively during the repetitions. These graphs show that the zero-offset and the signal on the reference angle 90° drift up to 1.7° and 8.1° respectively with 11,000 repetitions. The sensor gain in **Figure 2-28** is calculated from the signal difference in **Figure 2-26** and **Figure 2-27** divided by 90°. It represents that the sensor gain is maintained consistent up to 6,150 cycles with the mean value of 5.97 cnt/deg and the standard deviation of 0.0572. The sensor gain starts to decrease after 6,150 cycles with the rate of -9.57×10^{-5} cnt/deg per cycle which is equivalent to 0.0018° per cycle with an initial sensor calibration.

Chapter 3 Friction Modeling

3.1 Friction Along the Cable

3.1.1 Shape-Dependent Friction

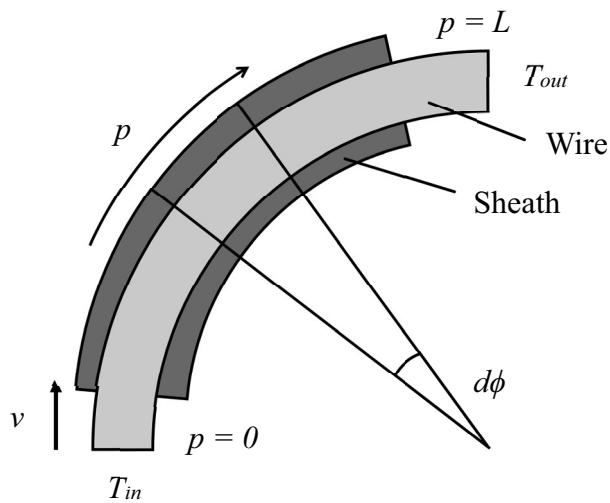

Figure 3-1 Schematic diagram of a static friction model along the wire.

One major issue for the Bowden-cable is shape-dependent hysteresis in terms of friction. The tension relationship between the input and output port of the cable is exponentially related to the accumulated bend angle of the sheath. **Figure 3-1** shows a schematic model of the static friction along the Bowden-cable. There exists a normal force between the wire and an inner wall of the sheath if the sheath is bent and the wire is tensioned. The friction force (F) can be represented as the normal force (N) multiplied by the friction coefficient. And the differential change of the tension along the wire is equivalent to the friction force.

$$F = \mu N \cdot \mathrm{sgn}(v) \tag{3-1}$$

$$dT = F \tag{3-2}$$

The force equilibrium between the normal force (N) and the tension (T) can be represented as (3-3) if $d\phi$ is sufficiently small.

$$N = Td\phi \tag{3-3}$$

The tension distribution along the cable can be modeled with the Capstan formula [17]–[20], as in

$$T(p) = \begin{cases} T_{in} \exp\left[-\mu\phi \cdot sign(v)\right] & (p < L_1) \\ T_0 & (L_1 \le p) \end{cases} \tag{3-4}$$

$$L_1 = \min\left\{p \in T(p) = T_0\right\} \tag{3-5}$$

$$T_{in} = T(p = 0) \tag{3-6}$$

$$T_{out} = T(p = L) \tag{3-7}$$

where $T(p)$ is the tension of the wire at position, p; μ is the coefficient of kinetic friction between the sheath and wire; ϕ is the summation of the bend angle of each segment, $d\phi$; v is the velocity of the wire relative to the sheath; and L is the total length of the sheath.

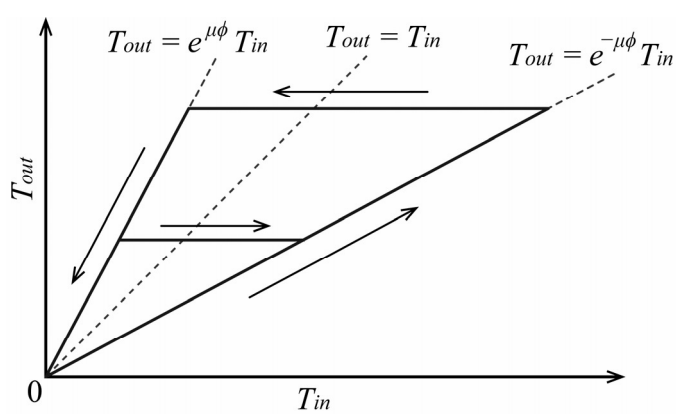

Figure 3-2 Characteristics of the relation between input and output.

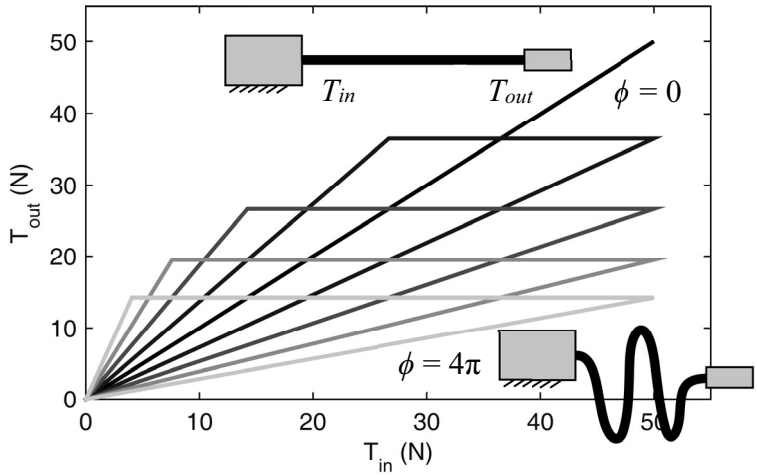

Figure 3-3 Friction characteristics of the Bowden-cable changes as the accumulated bend angle changes. The graph is plotted with the friction coefficient $\mu = 0.1$.

Figure 3-2 and **Figure 3-3** show a graphical illustration of (3-4)–(3-7) indicating that there is hysteresis between input and output tension of the Bowen-cable. There are four main phases of the relation. Firstly, if the input tension increases, the output tension increases with a transmission efficiency of $\exp(-\mu\phi)$. As the input tension decreases, the output tension maintains a constant value until the input tension reaches a certain point. Then the output tension decreases with a slope $\exp(\mu\phi)$. If the input tension increases again, the output tension maintains constant until the input and output tension satisfy $T_{out} = T_{in} \cdot \exp(-\mu\phi)$.

3.1.2 Shape Variation of the Sheath Inside the Workspace

Bend Angle

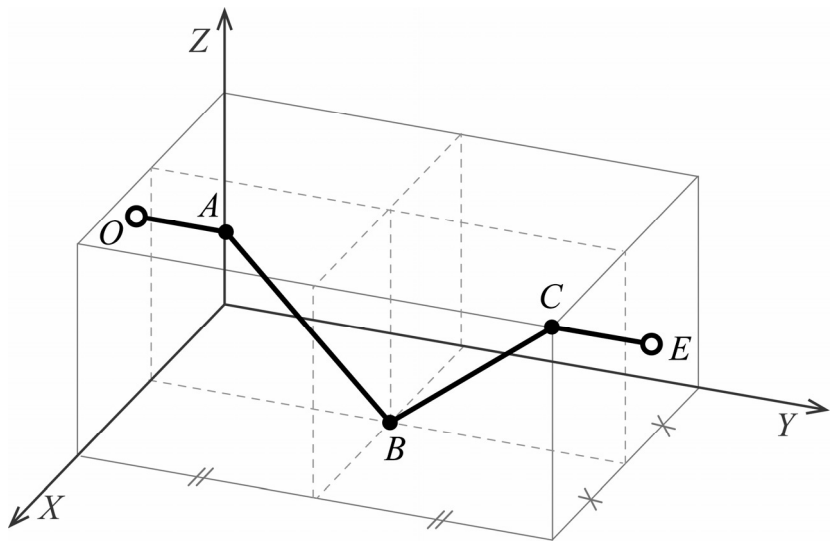

Figure 3-4 Schematic of a free hanging sheath between two points, *A* and *C*.

Figure 3-4 illustrates a sheath with a direct connection between the actuator, *A*, and the end-effector, *C*, in 3-D space. The sheath is represented by two straight lines, *AB* and *BC*, and five points, *O*, *A*, *B*, *C* and *E*.

$$A = (0,0,0) \tag{3-8}$$

$$C = (x,y,z) \tag{3-9}$$

$$\overrightarrow{OA} = \overrightarrow{CE} = (0,1,0) \tag{3-10}$$

Equations (3-8)–(3-10) describe the position of each point in 3-D space. The vectors *OA* and *CE* are set to a unit vector in the *Y*-axis to fix the relative orientation between the actuator and the end-effector.

$$\overrightarrow{AB} = \left(\frac{1}{2}x, \frac{1}{2}y, z_0 \right) \tag{3-11}$$

The *X* and *Y* position of *B* is assumed to be a mid-point of *A* and *C* as in (3-11).

$$\left|\overrightarrow{AB}\right| + \left|\overrightarrow{BC}\right| = L \tag{3-12}$$

With the constraint that the length of the sheath is constant, *L* as in (3-12), z_0 in (3-11) can be derived. The total bending angle of **Figure 3-4** can then be described by the following equation:

$$\phi_{free} = \angle\overrightarrow{OA}, \overrightarrow{AB} + \angle\overrightarrow{AB}, \overrightarrow{BC} + \angle\overrightarrow{BC}, \overrightarrow{CE} \tag{3-13}$$

The angle between the two vectors in (3-13) can be calculated with the dot product property described in (3-14); *P* and *Q* represent the arbitrary vectors in a 3-D space.

$$\angle\vec{P}, \vec{Q} = ArcCos\left(\frac{\vec{P} \cdot \vec{Q}}{\left|\vec{P}\right|\left|\vec{Q}\right|} \right) \tag{3-14}$$

Workspace

The workspace of the end-effector is bounded by the length of the Bowden-cable. The working position of the end-effector, *C*, should satisfy the following condition:

$$\sqrt{x^2 + y^2 + z^2} \leq L \tag{3-15}$$

Simulation

The bending angle was calculated within a range of workspaces using derived results from the previous section.

$$Error = \frac{\left|\phi_{ref} - \phi\right|}{2\pi} \times 100 \ (\%) \tag{3-16}$$

To compare the bending angle change within a workspace, an error of bending angle was calculated using (3-16) and plotted in **Figure 3-5** with a sheath length L of 1,000 mm. The reference bending angle, ϕ_{ref} in (3-16), was selected to have zero.

Figure 3-5 shows the distribution of the bending angle error in the workspace of the end-effector. The workspace has a half-sphere shape in accordance with (3-15). The colors of each point illustrate the bending angle error. The result shows zero error on (0, 1000, 0) which has a zero-bending angle. As the end-effector get closer to the actuator that is located on (0, 0, 0), the bending angle increases and it results in varying friction along the wire.

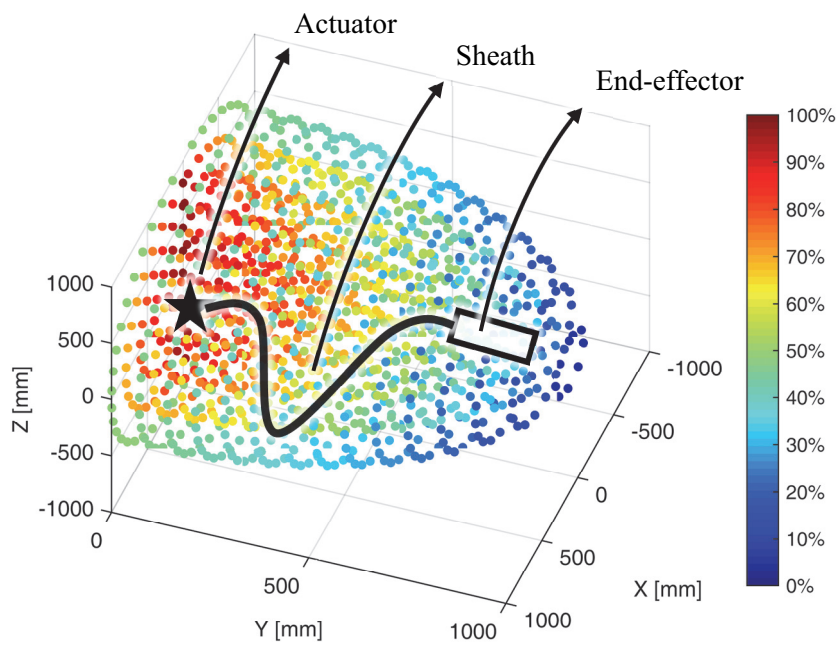

Figure 3-5 Simulation result of the bending angle error assuming that the actuator is placed on (0,0,0).

3.2 An Improved Friction Model

The Capstan formula in the previous section well describes the tension distribution along the wire and the hysteresis phenomenon between input and output tension of the wire. However, this model lacks to describe the actual input and output relationship, so it has limitation to be used for accurate friction compensation.

3.2.1 Deficiency of the Previous Model

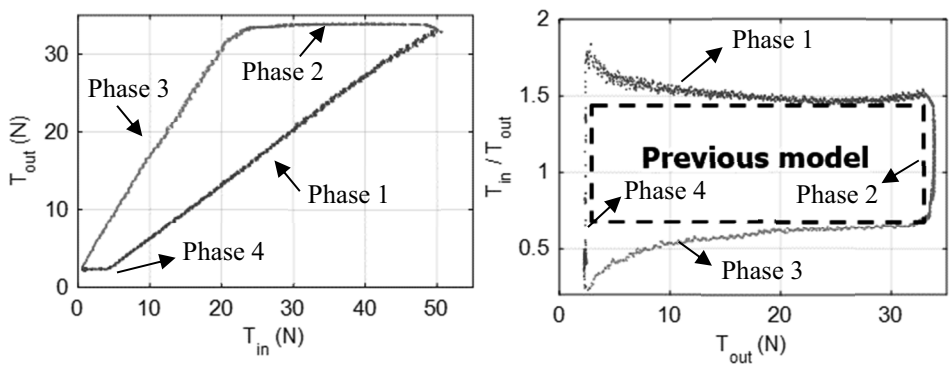

Figure 3-6 The experimental data showing the deficiency of the previous model.

Figure 3-6 shows the experimental data of input and output tension of the Bowden-cable when the sheath is subjected to 0˚ and 360˚ bend angle. From (3-4)–(3-7), the input tension divided by the output tension should be:

$$\frac{T_{in}}{T_{out}} = \exp\left[\mu\phi \cdot sign(v)\right] \tag{3-17}$$

which means the plot T_{out} versus T_{in} / T_{out} should be drawn in a square shape. However, it is obvious that the actual data in **Figure 3-6** do not coincide with the friction model (3-7). The experimental data suggests (3-7) should be a function of T_{out} and should not equal to 1 when $\phi = 0$. It arouses an improvement of the previous friction model for the Bowden-cable.

3.2.2 Improved Model

The proposed improved model takes two more physical phenomena, tension independent normal force and the inherent efficiency. The friction force considered in the previous model, (3-3), assumed that the normal force, *N*, is only related to the tension and bend angle of the wire [17]–[20]. In actual condition, however, the normal force in (3-3) is also influenced by the stiffness of the wire, a gap between wire and sheath, and other unpredictable factors. This consideration on the tension independent normal force can be written as:

$$N = Td\phi + \varsigma d\phi \tag{3-18}$$

where $\varsigma d\phi$ is the tension independent normal force of the cable. The combination of (3-1), (3-2), and (3-18) is reduced to:

$$\frac{dT(\phi)}{d\phi} = \left\{\mu T(\phi) + \mu\varsigma\right\} \cdot \mathrm{sgn}(v) \tag{3-19}$$

The inherent efficiency is adopted to represent the friction along the wire when the bend angle equals to zero.

$$T(\phi = 0) = \eta_0 \cdot T_{in} \tag{3-20}$$

where η_0 is the inherent efficiency ranges from 0 to 1. A solution of the differential equation (3-19) combined with the constraint (3-20) becomes a steady-state relationship between input and output tension of the Bowden-cable:

$$T_{out}^{steady}(\phi) = \eta_0^{-\delta} \cdot T_{in} e^{\mu\phi\cdot\delta} + \varsigma\left(e^{\mu\phi\cdot\delta} - 1\right) \tag{3-21}$$

$$\delta \equiv \mathrm{sgn}(v) \tag{3-22}$$

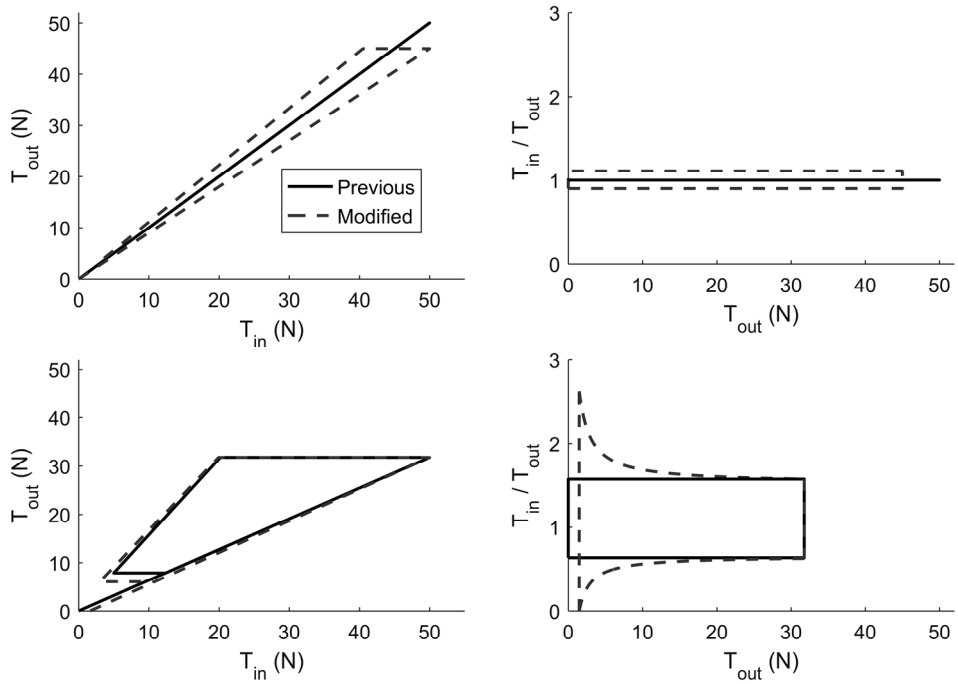

Figure 3-7 Comparison between previous and improved model for (upper graphs) $\phi = 0$ and (lower graphs) $\phi = 2\pi$. Parameters for previous and modified model: $\mu = 0.0721$, $\mu = 0.05$; $\varsigma = 4$ N; $\eta_0 = 0.9$.

Figure 3-7 illustrates the comparison of input and output relationship between previous and improved model when $\phi = 0$ (upper graphs) and $\phi = 2\pi$ (lower graphs). The improved model shows offset on x and y-intercepts when the sheath is bent representing that the output tension does not increase immediately after the input tension increases from zero. Similarly, the output tension does not converge to zero although the input tension decreases to zero which is in accordance with the actual phenomenon. Also, the input and output relationship shows hysteresis when $\phi = 0$ as if the sheath is bent representing the inherent efficiency.

3.2.3 Parameter Fitting

Three parameters should be determined for the improved friction model so that the model can be used for the friction compensation. Deciding the three parameters by trial and error is labor intensive and inaccurate unlike the previous model consist of one model parameter. This chapter introduces a parameter fitting algorithm that can directly calculate the three model parameters from the experimental data. The experimental data consist of input and output tension of the wire in several different bend angles are required to find the model parameters.

Optimization Problem

An optimization method is used to find the model parameter that minimizes the error between model and the experimental data. The optimization problem is reduced to:

$$\min_{P} \sqrt{\frac{1}{N} \cdot \sum_{i=1}^{n} \left\| E_i\left(P\right) \right\|_2^2} \quad \text{such that } 0 < \eta_0 < 1 \tag{3-23}$$

where P is an array including model parameters [η_0; μ; ς], n is the number of the data set with different bend angles, N is the total number of elements that is summed inside Sigma. $E_i(P)$ is an error function which is a difference between the experimental output tension and the model-based output tension. An initial value for the optimization P_0 = [0.9; 0.06; 3.3] was used to find P with an interior point method [60].

Phase Filtering

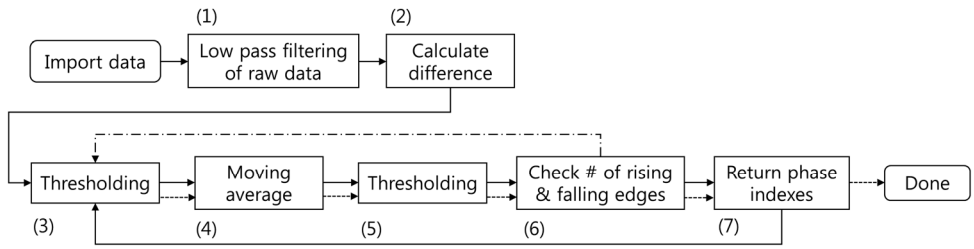

Figure 3-8 Block diagram of a phase filtering algorithm (stage 1 to 7) for the data set of input and output tension of the Bowden-cable.

Experimental data should be divided into three phases to calculate $E_i(P)$ for each hysteresis phases. Each hysteresis phases can be distinguished by the slope of the graph, T_{out} / T_{in}. However, the measurement noises and the model uncertainty of the experimental data demand proper filtering of the data. **Figure 3-8** proposes a phase filtering algorithm for the data of input and output tension of the wire. It consists of seven steps that return the data indexes of each hysteresis phases.

Differentiation with the low pass filtered data is processed at the first and second stage for the preprocessing. Ideally, the processed data should have positive constant value, zero, and constant negative value for phase 1, phase 2, and phase 3. However, the measurement noises prevent the processed data from a direct classification of the phases. Therefore, the moving averaging is applied at stage 4 to remove the thresholding jitter from the stage 3. Then the second thresholding is processed to remove the halfway phases created from the moving averaging. At this time, the rising and falling edges of the processed data are counted to check whether the filtered data have a same number of phases compared to the actual experiment. The same process from stage 3 and 7 are applied again to take a midpoint of the transition phase between two phases as a boundary. The filtering algorithm finishes if the edge counting test at stage 7 passed or go back to the stage 3 if the edge counting test

failed. **Figure 3-9** shows the processed data of the proposed phase filtering algorithm from the raw data to the final processed data. **Figure 3-10** shows the results of the phase filtered data from the bend angle of 0˚, 90˚, 180˚, 270˚, 360˚, 450˚, and 540˚.

Model Fitting

The model is fitted using the optimization method and the phase filtering with the experimental data. **Figure 3-11** shows the input and output tension data in 0˚, 90˚, 180˚, 270˚, 360˚, 450˚, and 540˚ with the previous fitted model and improved model. The original model does not represent the friction on 0˚ bend angle while the improved model coincides with the experimental data. As the bend angle increases, the intercepts of x and y-axis of the experimental data increases which is related to the coefficient of tension independent normal force, ς. However, the original model does not represent the line offset while the improved model matches with the experimental data. **Figure 3-12** shows the error between the fitted model and the experimental data for the original and the improved model in input tension domain. It is shown that the error of the improved model (orange cloud) is more close to the zero error line. **Figure 3-13** shows the root-mean-square (RMS) error of each model depending on the bend angle of the sheath. The RMS error of the improved model (red) is lower than the RMS error of the original model (black) in all bend angles with the total RMS error of 0.7836 N which is 39.63% lower than the total RMS error of the original model, 1.2980 N.

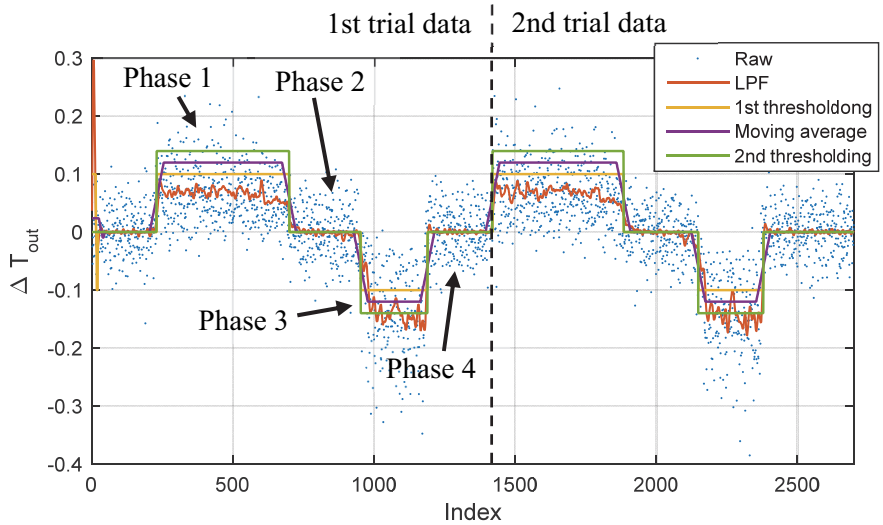

Figure 3-9 The processed data of the phase filtering algorithm showing raw data, processed data of low pass filtering, thresholding, and moving averaging.

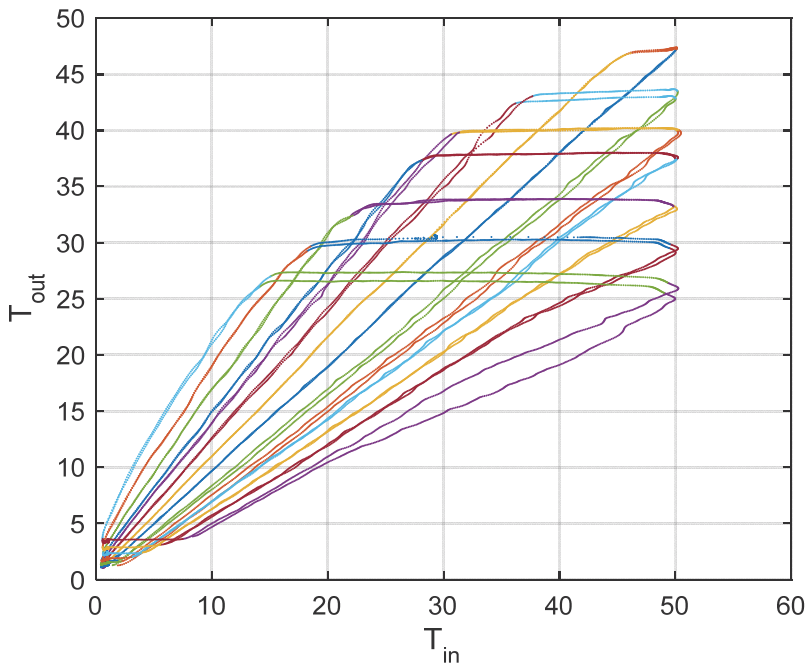

Figure 3-10 Results of the phase filtering with the data set from the bend angle of 0˚, 90˚, 180˚, 270˚, 360˚, 450˚, and 540˚. Each phase is differentiated by different colors.

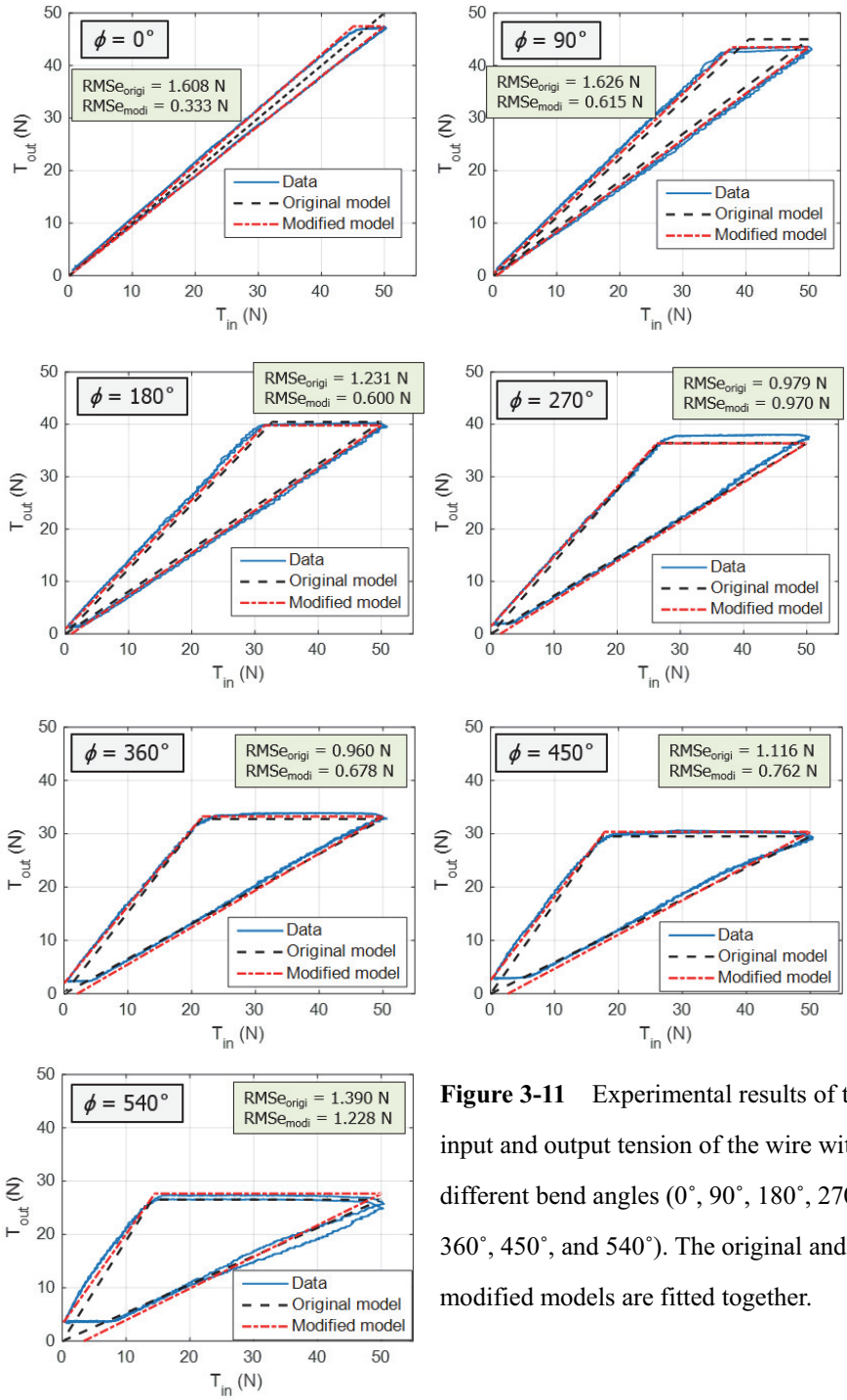

Figure 3-11 Experimental results of the input and output tension of the wire with different bend angles (0˚, 90˚, 180˚, 270˚, 360˚, 450˚, and 540˚). The original and modified models are fitted together.

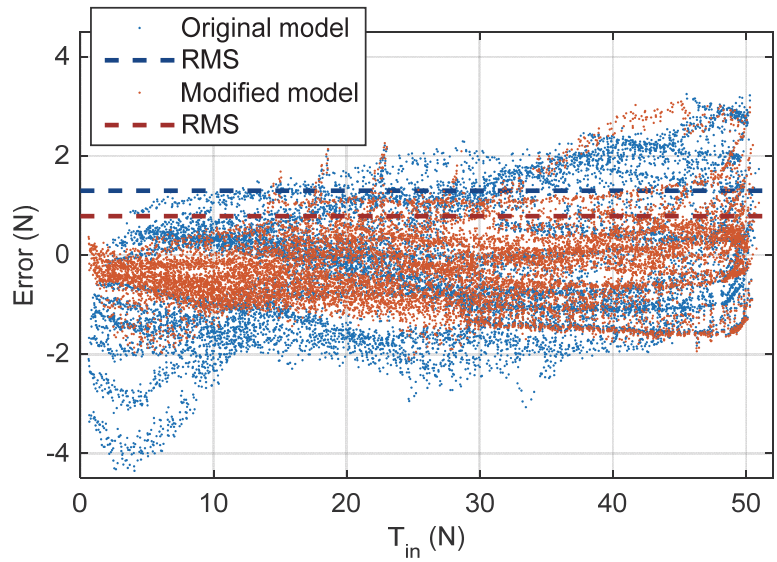

Figure 3-12 The comparison of errors with the original and modified models. Each dots refer data points and the dotted lines indicate the root-mean-square values of the errors.

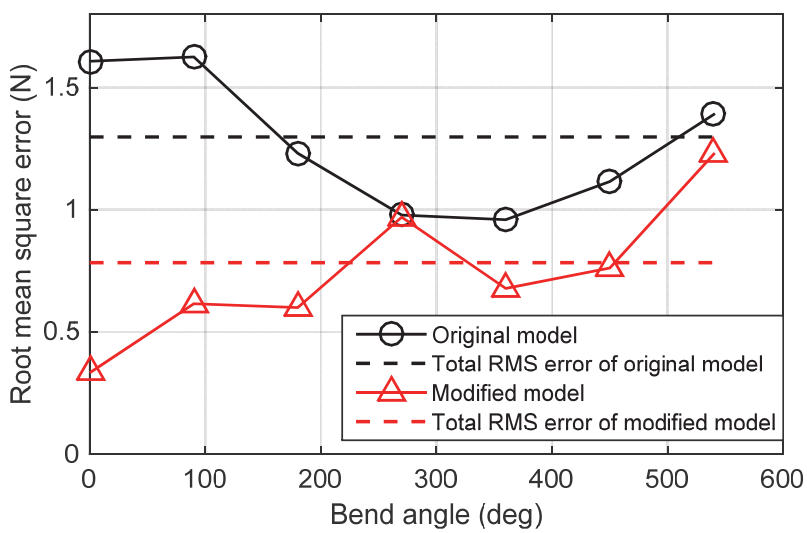

Figure 3-13 Root-mean-square error of the fitted model depending on the bend angle. The total RMS value of the modified model (red-dotted, 1.2980 N) is 39.63% lower than the total RMS value of the original model (black-dotted, 0.7836 N).

3.3 Friction Property Robustness

The friction characteristics of the system change with the repetitive operation because of the wear between the actuation wire and the sheath. In addition, changing ambient temperature of the environment can affect the friction due to the property change of the sliding surface. The varying characteristics of the friction affect the tension control performance of the proposed system since the system does not have output feedback and rely only on the pre-identified system parameters.

The experiment is conducted to see the effect of the repetitive operation (1 to 9,700 cycles) and the temperature change (−50 °C to +70 °C) on the friction property change of the Bowden-cable actuation system. The sheath is subjected to the 180˚ bend angle and the sinusoidal input tension (amplitude: 30 N, period: 3 s) is applied to the Bowden-cable system while the output tension is measured with the tension sensor.

3.3.1 Abrasion Effect

The sinusoidal input tension is applied on the system up to 9,700 cycles. The ambient temperature is maintained as consistent as possible (24.5 ± 1 ˚C) to reduce the effect of the temperature-dependent property change of the materials. The number of repetitions, input, and output tension of the wire were measured and saved for 8 seconds with every 10 minutes (used 0.457 mm diameter stainless steel wire from Sava Industries, Inc. and Teflon tube with 1.38 mm inner diameter).

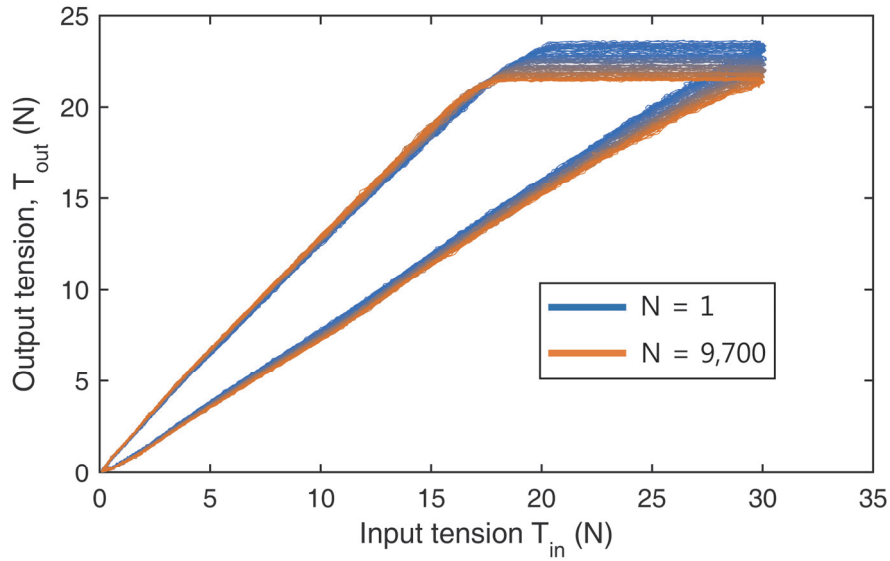

Figure 3-14 Input and output tension of the Bowden-cable actuation system with the repetitive operation up to 9,700 cycles.

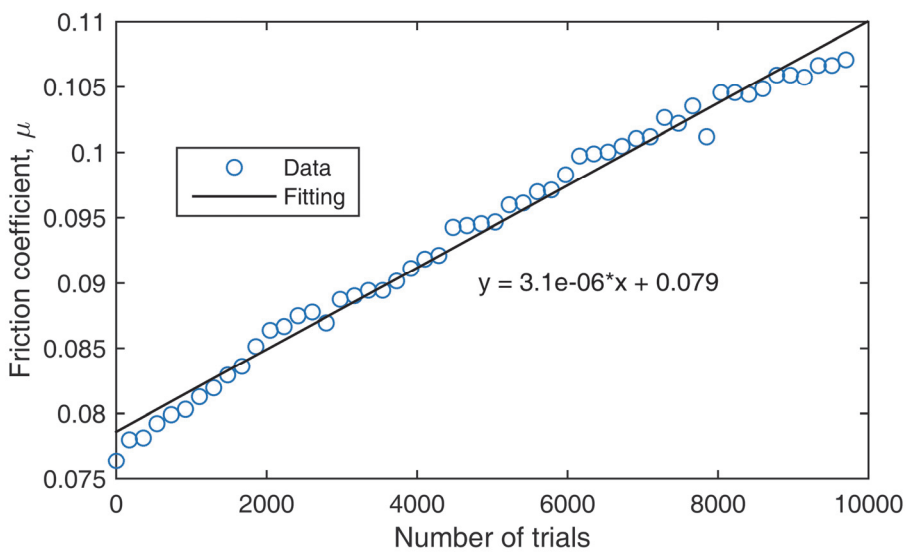

Figure 3-15 Experimental data of the friction coefficient with the increasing number of trials. The friction coefficient is calculated using the previous friction model.

Figure 3-14 shows the relationship between input and output tension of the Bowden-cable actuation system during the operation from 1 to 9,700 repetitions. The result shows that the friction along the cable increases with the repetitive operation of the system. **Figure 3-15** represents the friction coefficient calculated from the data in **Figure 3-14** using the previous friction model. It shows the friction coefficient increases with the repetitions with a change rate of 3.14×10^{-6}. The friction coefficient is increased 40.22% with the 9,700 repetitions and it takes about 1,700 repetitions for the friction coefficient to have a 10% errors compared to the initial value. This experimental result convinces that the model-based feedforward friction compensation system should take into account the degradation of the cable driven system. The basic approach to deal with the increasing friction coefficient is the periodic calibration of the system or replacement of the cable and the liner. This is the main disadvantage of the cable driven system that the cable system degrades (friction increment and elongation of the wire) with a number of usages should be replaced periodically. The algorithmic approach to compensate the friction change is using the experimental model for the estimation of the friction coefficient which increases with the number of repetitions.

3.3.2 Temperature Effect

The cable system is chilled down to −50 °C using an instant refrigerating spray (SF-1013, NAMBANG CNA Co., Ltd.) and warmed up using a heat-gun up to +70 °C. A digital thermometer is used to measure the lowest (−50 °C) and highest (+70 °C) temperature of the cable system together with the ambient temperature of the room (22 °C). The sinusoidal input tension is applied to the system and the output tension is measured during the experiment.

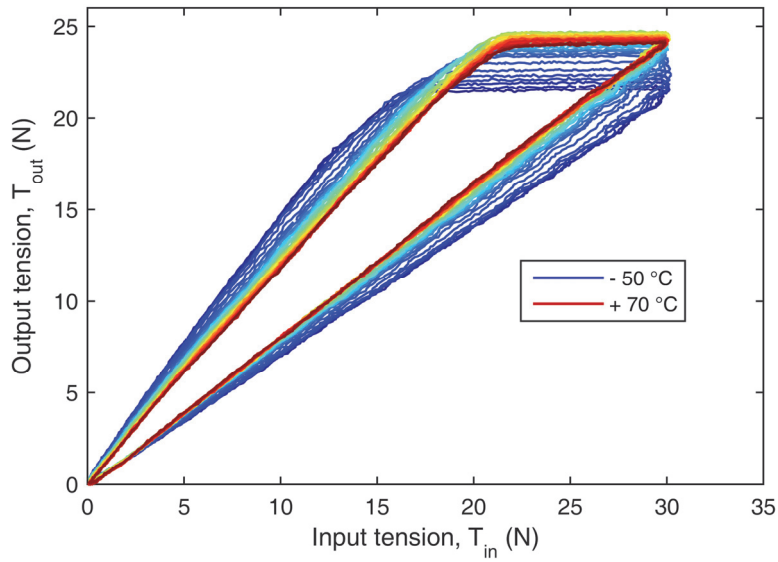

Figure 3-16 Input and output tension of the Bowden-cable actuation system with the varying temperature from −50 °C to +70 °C.

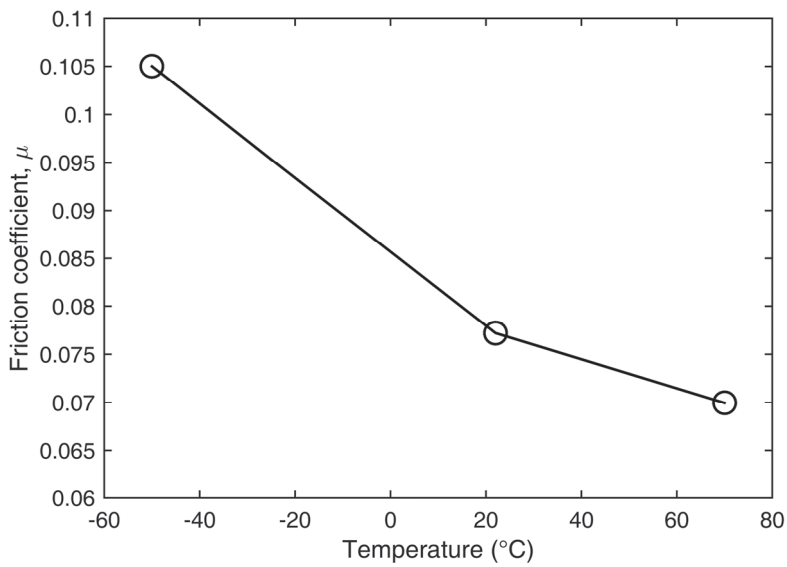

Figure 3-17 Experimental data of the friction coefficient with the varying temperature from −50 °C to +70 °C.

Figure 3-16 and **Figure 3-17** shows the relationship between the input and output tension of the wire during the temperature change from −50 °C to +70 °C. The result represents that the amount of the friction is inversely proportional to the temperature of the cable system. The friction coefficient calculated from the previous friction model decreased from 0.105 to 0.077 and 0.070 on −50 °C, +22 °C, and +70 °C respectively. The average change rate of the friction coefficient depending on the temperature is -2.92×10^{-4} $°C^{-1}$ which indicates the temperature change of 10 °C results in 3.79% error of the friction coefficient on the basis of the ambient temperature +22 °C. The effect of the temperature on the cable system should be taken into account and it should be properly compensated if the system is expected to encounter the varying temperature that would exceed the required tolerance of the system. For example, a temperature sensor (e.g. LM35, Texas Instruments Inc.) can be used with a linear fitting model of the friction coefficient change rate to compensate the temperature dependency.

Chapter 4

Actuation with Embedded Bending Sensing

4.1 Concept

Bend estimation of the Bowden-cable is crucial when the shape of the sheath is expected to change during operation. The optical sensors used to measure the shape of the sheath are thin and flexible. However, the structure of the device should be modified for a separate shape-sensing system. Furthermore, the fabrication process and signal processing of the grating fiber are complicated.

This section discusses a dual-wire scheme that uses an actuation wire and a sensing wire inside the same sheath for real-time estimation and compensation of Bowden-cable hysteresis with a fully embedded design.

4.1.1 Principle

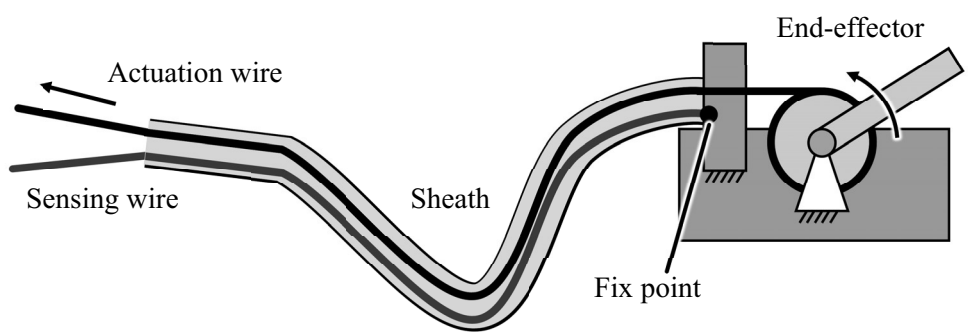

Figure 4-1 Dual-wire scheme combining an actuation wire and a sensing wire inside the same sheath.

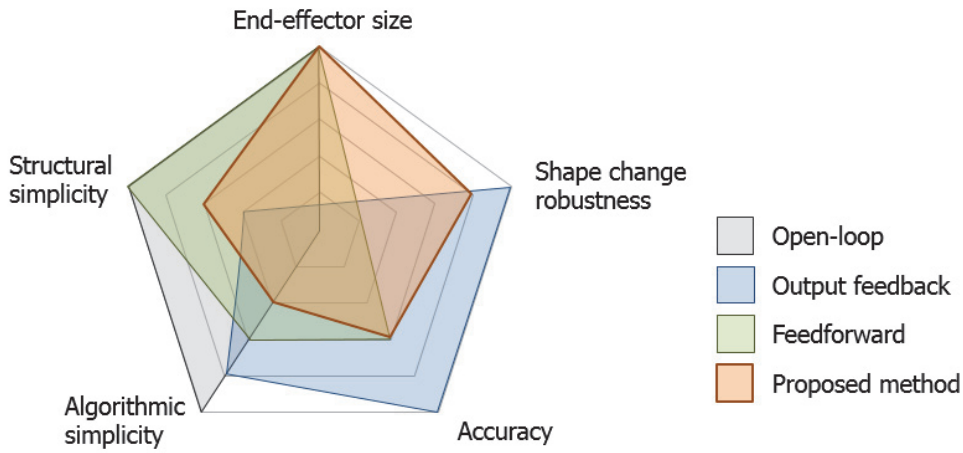

Figure 4-2 Qualitative comparison of different cable actuation approaches.

The bend estimation technique that uses the sensing wire can share the same sheath with the Bowden-cable actuation system. **Figure 4-1** illustrates the concept of the dual-wire scheme: The actuation wire and sensing wire are placed inside the same spring sheath. The output port of the actuation wire is connected to the end-effector, and one end of the sensing wire is fixed to the frame of the end-effector. The actuation wire transfers power through the guide sheath while the sensing wire detects the central displacement change of the sheath and estimates the bend.

The proposed method is advantageous because a separate bend-sensing system is not required and the only additional component needed for bending sensing is just another wire. In addition, the sensing wire is thinner than optical fibers and does not require the complex signal processing that is commonly used for shape sensors.

In addition, the proposed method is distinguished from other methods such as open-loop, output feedback, and feedforward compensation in that the size and the structural complexity of the end-effector can be minimized while retaining the robustness of the sheath shape change and the accuracy of control. The only additional element on the end-effector is the fixation point of the sensing wire, which

is easily achieved with an adhesive, bolting, or knots.

4.1.2 System Configuration

The overall system configuration is illustrated in **Figure 4-3** using the block diagram. The system mainly consists of five parts—the Bowden-cable transmission with the embedded sensing wire, end-effector, tension estimation system, friction compensation algorithm, and the tension-controlled tendon actuator. The input to the whole system is the tension setpoint, T_s, and the output of the system is the output tension, T_{out}, on the output port of the Bowen-cable. The tension of the wire is only measured at the actuator side to provide the accurate tension source. The reference output tension sensor can be used on the end-effector for the calibration of the friction properties of the Bowden-cable. The calibration of the bend estimation system can be done while the Bowden-cable is constrained in a fixed shape.

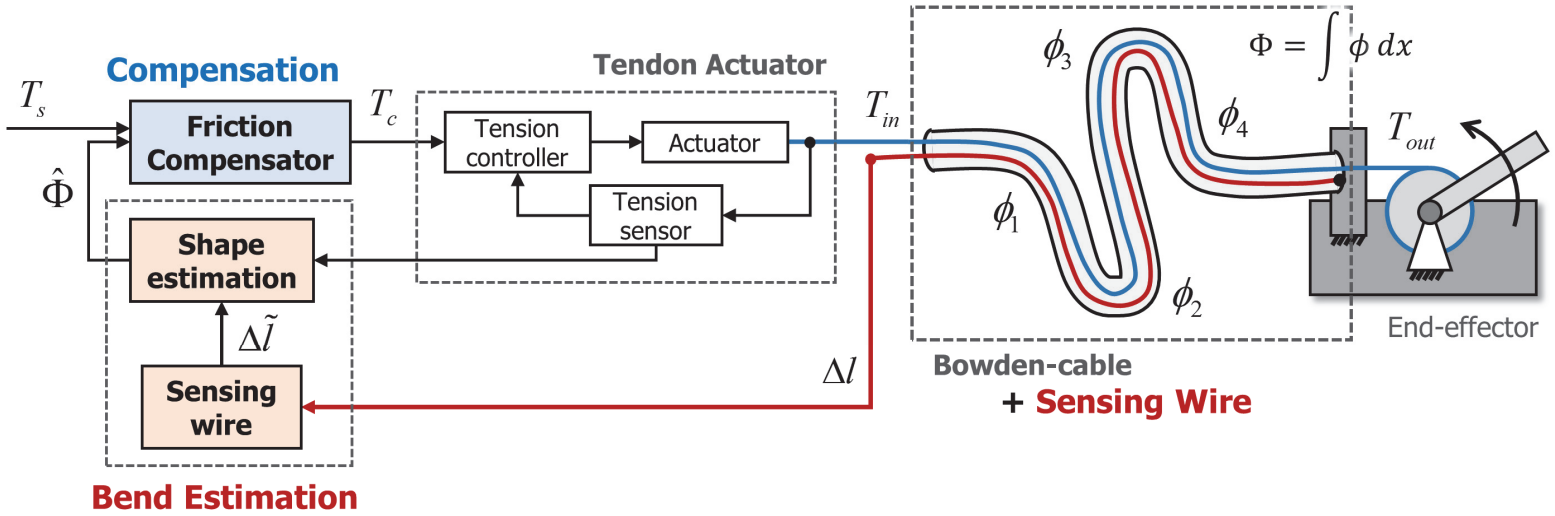

Figure 4-3 Block diagram of the proposed sensorless control system of a Bowden-cable with a dual-wire scheme. The system consists of five parts: Bowden-cable with embedded sensing wire, end-effector, bend estimation system, friction compensation algorithm, and tension-controlled tendon actuator.

4.2 Bend Estimation during Actuation

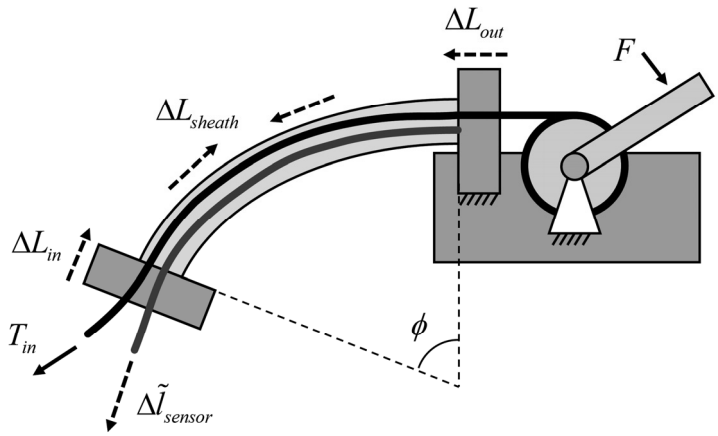

Figure 4-4 Compressive force is applied to the sheath and the supporting parts along the axial direction as a reaction force to the tension of the actuation wire.

The bend estimation technique described in the previous section cannot be directly applied to the dual-wire scheme because of the compressibility of the spring sheath when the actuation wire applies tension (tension of the sensing wire is negligibly small). The actuation wire can transmit force through the sheath because the supports on the ends of the sheath exert a compressive reaction force to the sheath along the axial direction. This phenomenon results in compression of the sheath and the supporting parts which affect the displacement change of the sensing wire. Therefore, the displacement changes of the sensing wire due to the tension of the actuation wire should be compensated to accurately estimate the bend angle of the Bowden-cable. Then the estimation of the bend angle, $\hat{\phi}$, becomes:

$$\hat{\phi} = \frac{1}{A}\left\{\Delta \tilde{l}_{sensor} + \Delta \hat{L}_{compress}\right\} \tag{4-1}$$

where $\Delta \tilde{l}_{sensor}$ is the measurement of the displacement change of the sensing wire and $\Delta \hat{L}_{compress}$ is the estimation of the compression along the supports and

the sheath.

For the estimation of the compression, the stiffness of the sheath and supporting parts is assumed to be linear with the value of E_s, K_{in}, and K_{out} as Young's modulus of the sheath multiplied by the cross-sectional area, stiffness of the supporting part on the input port and the output port respectively. Then the compression along the sheath (ΔL_{sheath}) and the deformation of the supporting parts (ΔL_{in} and ΔL_{out}) can be represented with the tension distribution as:

$$\Delta L_{compress} = \int_{in}^{out} \frac{T(x)}{E(x)} dx = \Delta L_{in} + \Delta L_{sheath} + \Delta L_{out} \tag{4-2}$$

$$\Delta L_{sheath} = \int_{0}^{L} \frac{T(x)}{E_s} dx \tag{4-3}$$

$$\Delta L_{in} = \frac{T(x=0)}{K_{in}} \tag{4-4}$$

$$\Delta L_{out} = \frac{T(x=L)}{K_{out}} \tag{4-5}$$

Then, $\Delta L_{compress}$ becomes a function of bend angle (ϕ) that has four phases since it is affected by the friction along the cable as in **Figure 4-5**. Equations (4-4) and (4-5) can be directly calculated from (3-21) while (4-3) requires some integral calculus. ΔL_{sheath} can be calculated by deriving the under area of the tension distribution for the steady-state and transient-state of the winding (4-6) and releasing (4-8) phases which are depicted in **Figure 4-5**.

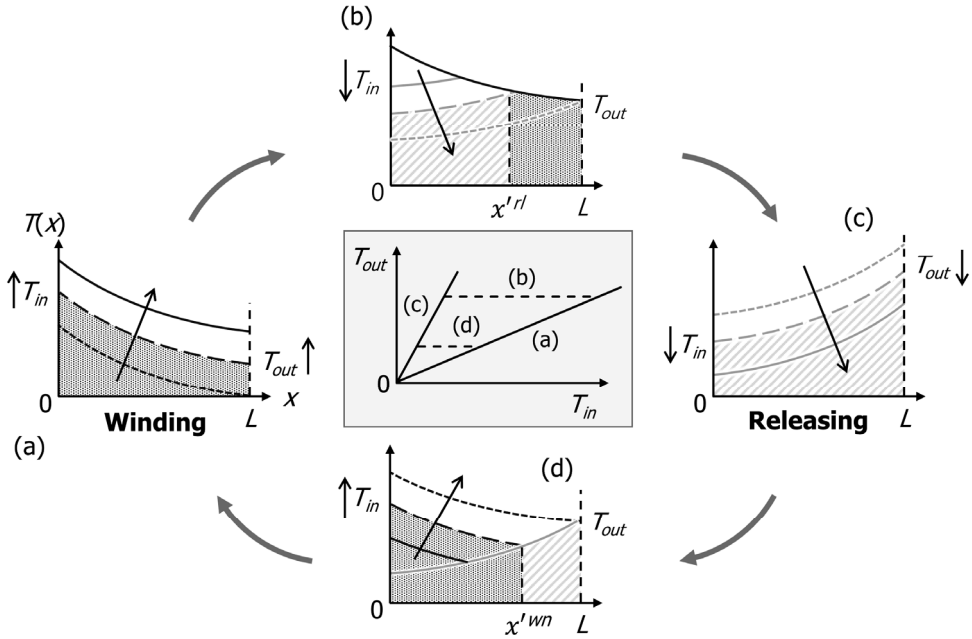

Figure 4-5 The graphs showing the tension distributions along the cable for four phases; (**a**) steady-state winding; (**b**) transient-state releasing; (**c**) steady-state releasing; (**d**) transient-state winding.

$$\Delta L_{sheath}^{wn} = \int_0^{x'^{wn}} \frac{T(x)\big|_{\delta=-1}}{E_s} dx + \int_{x'^{wn}}^{L} \frac{T(x)\big|_{\delta=1}}{E_s} dx \tag{4-6}$$

$$x'^{wn} = \frac{L}{2\mu\phi} \ln\left(\frac{\eta_0 T_{in} + \varsigma}{\eta_0^{-1} T_{in0} + \varsigma} \right) \tag{4-7}$$

$$\Delta L_{sheath}^{rl} = \int_0^{x'^{rl}} \frac{T(x)\big|_{\delta=1}}{E_s} dx + \int_{x'^{rl}}^{L} \frac{T(x)\big|_{\delta=-1}}{E_s} dx \tag{4-8}$$

$$x'^{rl} = \frac{L}{2\mu\phi} \ln\left(\frac{\eta_0 T_{in0} + \varsigma}{\eta_0^{-1} T_{in} + \varsigma} \right) \tag{4-9}$$

where x' is the transition position of x that the graph of $T(x)|_{\delta=1}$ and $T(x)|_{\delta=-1}$ intersects and satisfies $0 < x' < L$ for the transition phases (**Figure 4-5**

b and **d**). T_{in0} refers the latest value of T_{in} before it changes the sign of $\dot{T}_{in}$. Then the steady-state sheath compression of the winding phase and the releasing phase should become $\Delta L^{wn}_{sheath}|_{x'=L}$ and $\Delta L^{rl}_{sheath}\big|_{x'=L}$ respectively. The detailed calculation of (4-6)–(4-9) is provided in **Appendix B**.

The above equations, however, are numerically unstable near $\phi = 0$ and require intensive computation. In addition, it lacks simplicity to be used on the embedded real-time application. Therefore, (4-6)–(4-9) can be linearized using an approximation of (4-10) and resulting (4-11).

$$e^{\mu\phi\cdot\delta} \approx \mu\phi\cdot\delta + 1 \tag{4-10}$$

$$\Delta L^{steady}_{sheath} \approx \frac{\mu}{2K_s\delta}\left(\eta_0{}^{-\delta}T_{in} + \varsigma\right)\phi + \frac{\eta_0{}^{-\delta}}{K_s}T_{in} \tag{4-11}$$

where K_s is the stiffness of the sheath which equals to E_s/L. The transient sheath compression of the approximated model maintains the constant value until it meets the other steady-state curve which is same as the hysteresis of the friction in **Figure 3-2**. See **Appendix B** for the details of the transition tension of the approximated model.

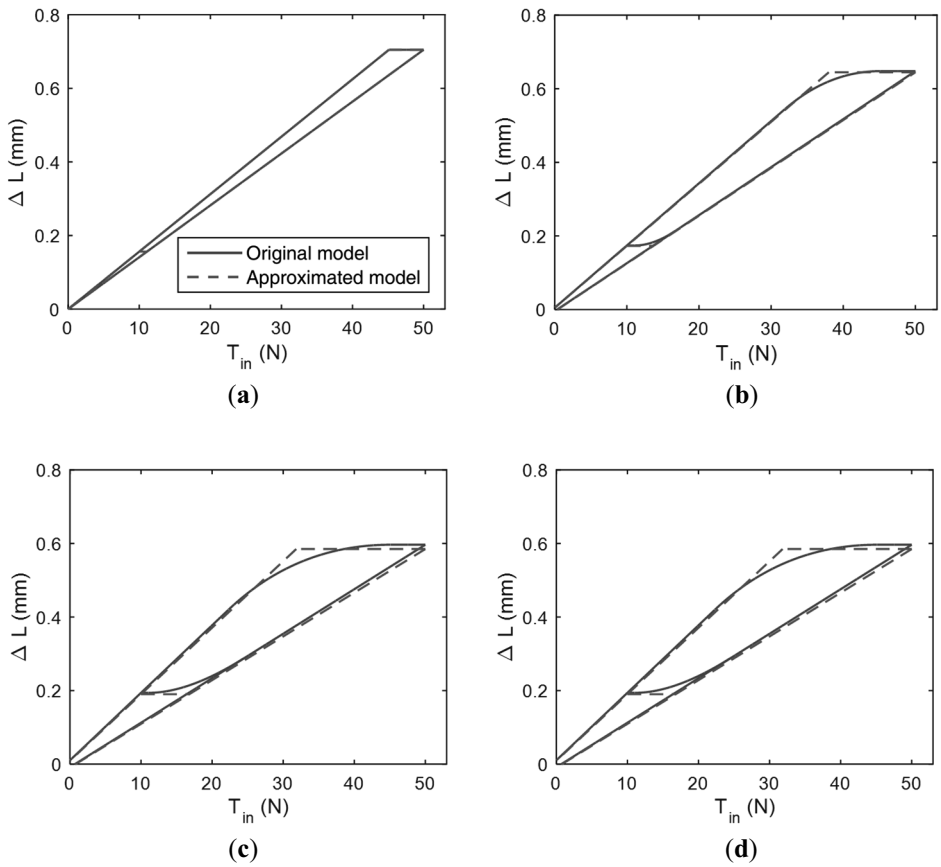

Figure 4-6 The compression model of the sheath and supporting parts with the original model (blue solid line) and the approximated model (orange dotted line) for the bend angle (**a**) $\phi = 0$; (**b**) $\phi = \pi$; (**c**) $\phi = 2\pi$; (**d**) $\phi = 3\pi$. The approximated model represents the hysteresis curve of the original model but with the easily implementable linear lines.

The estimation of the bend angle using (4-1) requires a numerical iteration because it does not have an analytical solution since $\Delta\hat{L}_{compress}$ includes a hysteresis that is dependent on the bend angle and the tension of the wire. A fixed-point iteration [61] was used to solve the above problem since it is easy to implement, does not require Jacobian information, and (4-1) does not have local minima. In addition, (4-1) coincide with the precondition of the fixed-point iteration that the

function *f* should be represented as $x = f(x)$.

Proof Let $f(\hat{\phi}) = \frac{1}{A}\{\Delta\tilde{l}_{sensor} + \Delta\hat{L}_{compress}(\hat{\phi})\}$, then (4-1) can be represented as $\hat{\phi} = f(\hat{\phi})$. Then $\hat{\phi}_{n+1} = f(\hat{\phi}_n)$ converges to the solution of $\hat{\phi} = f(\hat{\phi})$ within a finite step if $f(\hat{\phi})$ satisfy an inequality, $|df(\hat{\phi})/d\hat{\phi}| < 1$ which can be rearranged to (4-12). Therefore, the design parameters satisfying the inequality of (4-12) guarantee the convergence of the solution.

$$0 \le T_{in} < \frac{\left(2AK_{out}K_s\right)/\mu - \varsigma\left(K_{out} + 2K_s\right)}{K_{out} + 2K_s}\eta_0 \tag{4-12}$$

Equation (4-12) illustrates the region that guarantees the convergence of the solution is affected by the tension of the wire, the stiffness of the system components, and the friction properties of the wire. **Figure 4-7** illustrates the stable the region that satisfies the convergence condition in (4-12) with the given system parameters (η_0 = 0.95, ς = 4 N, A = 0.269 mm/rad, E_s = 54,000 N, μ = 0.05). It is shown that if the operating condition of the system is within the range of $0 \le \phi \le 3\pi$ and $0 \le T_s \le 80$ N, the bend angle could be estimated with the sheath length (L) up to 5 m which has an enough stability margin.

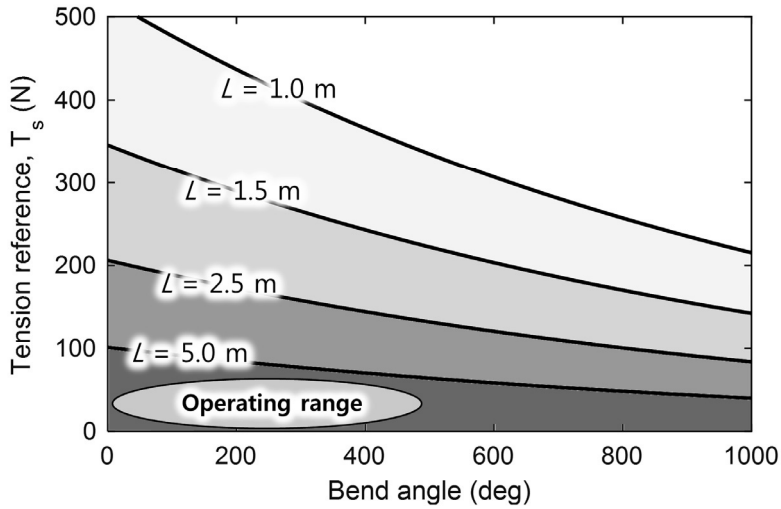

Figure 4-7 The region that satisfies the convergence condition in (4-12). The condition of the operating range (η_0 = 0.95, ς = 4 N, A = 0.269 mm/rad, E_s = 54,000 N, μ = 0.05, $0 \le \phi \le 3\pi$, $0 \le T_s \le 80$ N) satisfies the convergence of the solution for (4-1) using the fixed-step iteration up to L = 5 m with the assumption that the output support part is rigid ($K_{out} \to \infty$).

Figure 4-8 and **Figure 4-9** shows the simulation result of the bend estimation with a varying bend angle of the sheath and the input tension of the wire using the approximated compression model and fixed-point iteration. There exists a small estimation error that is originated from the approximation of the original compression model. It shows the stable convergence of the bend estimation.

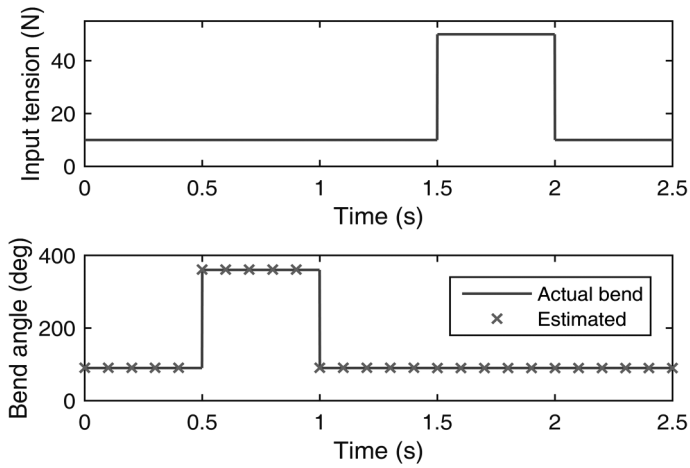

Figure 4-8 Simulation result of the bend estimation using the fixed-point iteration with a loop time 0.1 s showing the convergence of the estimated bend angle.

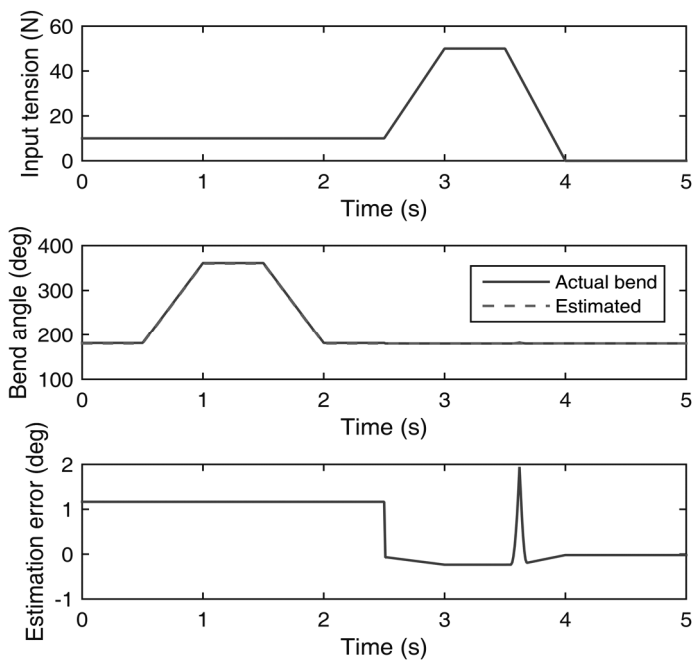

Figure 4-9 Simulation result of the bend estimation with a varying bend angle of the sheath and the input tension of the wire using the approximated compression model and fixed-point iteration. Simulation condition: $\mu = 0.05$; $\varsigma = 4$ N; $\eta = 0.95$; $K_s = 180$ N/mm; loop time = 0.01 s.

4.3 Multi-Bending Curvature

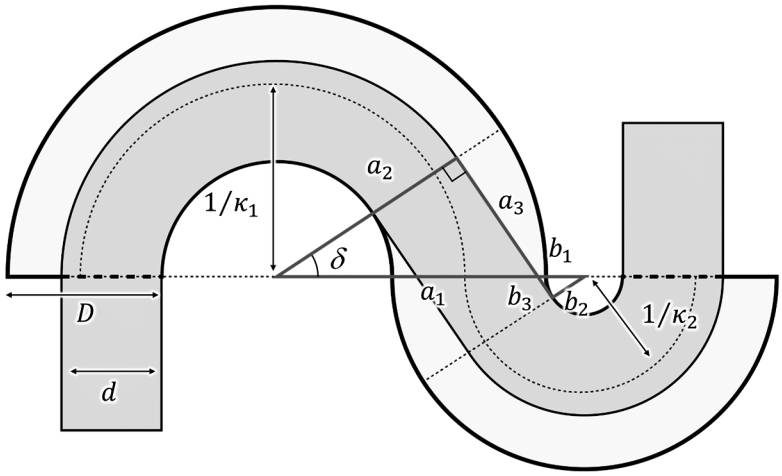

Figure 4-10 A schematic of the sheath and the sensing wire showing the effect of wire-sheath gap on multi-bending curvature.

The gap between the sensing wire and the sheath can affect bend estimation when the two adjacent curvatures have different curving directions. **Figure 4-10** shows the schematic of sheath and wire with the diameter of D and d respectively. The traveling path of the wire is shorter than that of the sheath if $d < D$ and two neighboring curvatures have different curving directions. It causes the bend estimation error when the diameter of the sensing wire is smaller than the inner diameter of the sheath.

The displacement changes of the sensing wire when it is subjected to sheath-wire gap, $\Delta l_{gap,}$ becomes:

$$\Delta l_{gap} = A\left(\Phi_{sheath} - \Phi_{gap}\right) \tag{4-13}$$

$$\Phi_{gap} = \sum_{i=1}^{c} \chi_i \cdot \cos^{-1}\left\{1 - \frac{\kappa_i \kappa_{i+1}\left(D-d\right)}{\kappa_i + \kappa_{i+1}}\right\} \tag{4-14}$$

$$\chi_i = \frac{1}{2}\left|\mathrm{sgn}\left(\kappa_i\right) - \mathrm{sgn}\left(\kappa_{i+1}\right)\right| \tag{4-15}$$

where Φ_{sheath} is the accumulated bend angle along the sheath, Φ_{gap} is the error of bend angle due to the sheath-wire gap, c is the number of different curvatures, and κ_i and κ_{i+1} are the adjacent curvatures along the sheath. χ_i indicates whether the adjacent curvatures contain the inflection point or not. (4-13) indicates that the length change of the sensing wire is affected by the curvature variation along the sheath. The simulation result of (4-14) shows that Φ_{gap} becomes 23.0° when the $D - d = 0.5$ mm and $\kappa_1 = \kappa_2 = 80.0$ m^{-1} which is not a negligible value. In this case, the bend estimation error using the sensing wire is unpredictable when the sheath is subject to varying configuration condition.

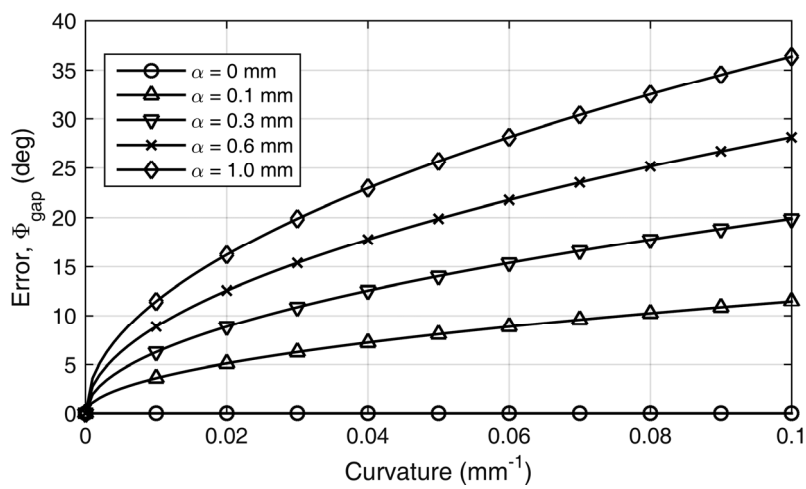

Figure 4-11 The simulation result illustrating the error of the bend angle due to the sheath-wire gap with two adjacent curves with the same amount of curvature and different direction. Plotted with the different curvatures and backlash gap ($\boldsymbol{\alpha = D - d}$).

However, the bend estimation error became an advantage when the estimation is used for the purpose of friction estimation and compensation along the cable. The

bend angle, ϕ, in the previous friction modeling section should be the accumulate contact angle between the wire and inner surface of the sheath, not the bend angle of the sheath which converts ϕ in (3-21) to:

$$\phi = \Phi_{friction} = \Phi_{sheath} - \Phi_{gap} \tag{4-16}$$

where $\Phi_{friction}$ is the friction effective bend angle that is related to the friction along the cable. Therefore, the bend estimation using the sensing wire with (2-14) and (2-15) estimates the friction effective bend angle, if the diameter of the sensing wire is same as the diameter of the actuation wire, which should be used for the estimation and compensation of the friction along the cable. This sensing characteristic assimilates with friction compensation system that the other bending sensing method cannot perform—the optical fiber–based sensors measures Φ_{sheath} that brings estimation and compensation error of the friction.

4.4 Friction Compensation

4.4.1 Compensation Rule

The feedforward compensation rule follows the inverse of the friction model (3-21).

$$T_c = \eta_0^{-\delta} \left\{ \left(T_s + \varsigma \right) \cdot \exp\left(\mu \hat{\Phi} \cdot \delta \right) - \varsigma \right\} \tag{4-17}$$

$$\delta = \operatorname{sgn}\left(\frac{dT_s}{dt} \right) \tag{4-18}$$

where T_c is compensated tension that should be applied to the input port of the Bowden-cable to generate the setpoint tension, T_s, on the output port. Here, T_s is used rather than T_{in} to avoid the control jitter that could arise from the sensor noise. $\hat{\Phi}$ is the accumulated bend angle estimation of the sheath calculated from (4-1). The

overall block diagram of the system is illustrated in **Figure 4-3**.

4.4.2 Friction Degradation

The identified parameters of the friction model in **0** is used for the friction compensation using (4-17). However, one drawback of the model-based feedforward control system is the uncertainty of the model parameters that varies over time due to the environmental conditions and the aging of the hardware. In a case of the proposed system, the friction coefficient can increase as the wire and the sheath liner wears out with the continual operation of the system.

To minimize the degradation of the friction property, the actuation wire and the sheath liner should be chosen that has a high durability of abrasion. In this study, a stainless steel wire without a coating and a Teflon lining are used for the cable system. The polymer wires are not preferred for the actuation wire since the stainless steel wire has high abrasive durability compared to the polymer-based wires (PTFE, nylon, Dyneema, Kevlar, etc.). In addition, it is recommended to use the wire without coating because the coating wears out easily and play a great role in the rapid degradation of the friction property. Also, the stainless steel without the coating has the same friction coefficient (= 0.04) compared to the FEP coated one if it is used with Teflon liner [62].

Nevertheless, there remains an unavoidable aging of the cable system and it results the control error of the system. The simulation is conducted to see the control performance with the friction parameter uncertainty on the cable system. **Figure 4-12** to **Figure 4-14** show the simulation results of the friction compensation using the compensation rule in the previous section with the model parameters $\mu = 0.05$; $\varsigma = 4$ N/rad; $\eta = 0.95$; $K_s = 180$ N/mm and the bend angle 2π. The friction coefficient of the plant, μ, is increased from 0 to 30% to simulate the abrasion and aging of the cable system.

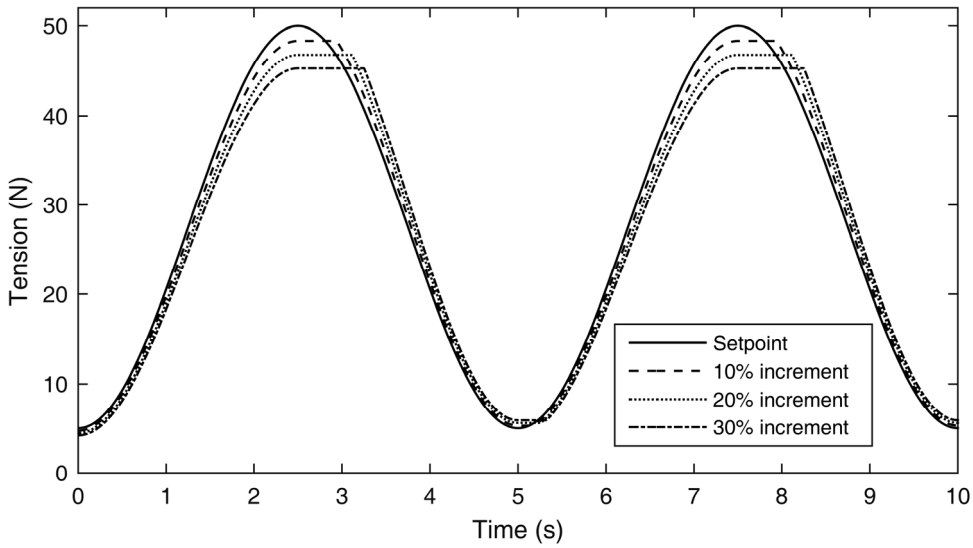

Figure 4-12 The simulation result that shows the output tension of the system with the friction coefficient increment of the system in the time domain. (solid line) tesnsion setpoint; (dashed line) 10%; (dotted line) 20%; (dash-dot line) 30% increment of the friction coefficient.

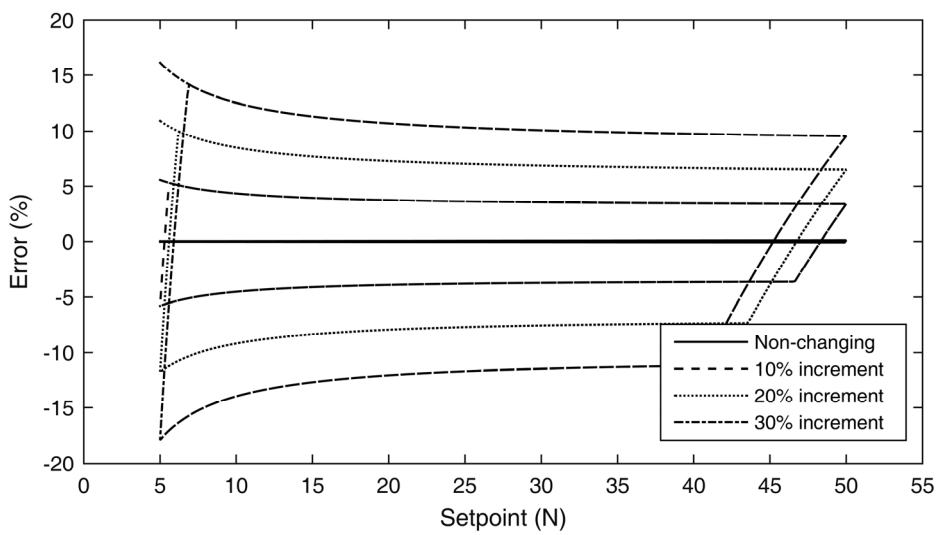

Figure 4-13 The simulation result showing the control error, $[T_s - T_{out}]/T_s \times 100\%$, in the setpoint domain with the fricion coefficient increment. (solid line) non-changing; (dashed line) 10%; (dotted line) 20%; (dash-dot line) 30% increment of the friction coefficient.

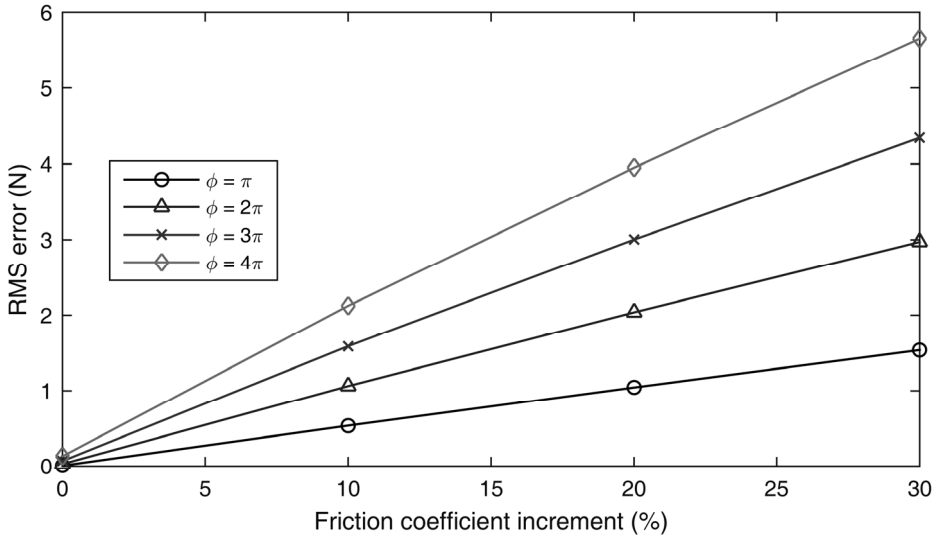

Figure 4-14 The simulation result showing the root-mean-square error of the output tension with the friction coefficient increments from 0% to 30% and the bend angle from π to 4π.

4.5 Tendon Actuator

4.5.1 Slack Enabling Actuator

Most TMDs use a spool and motor to wind and release the wire. In this case, the derailment of the tendon from the spool and friction along the cable sheath make the robot difficult to control. The tension of the wire near the spool has to be maintained over a certain level to prevent slacking of the wire, which derails the wire from the spool and causes the actuator to fail. Several studies have attempted to solve this problem in the view of mechanical design and control. One study [13] used a rubber pad to maintain taut tension of the wire inside the actuator. Another [63] used a passive tensioner with slack adjustment and an active tensioner to account for slack loss and to keep the wire from derailing. A third study [64] designed an array of pulleys to be in constant contact for preventing excessive high wire tension and derailment. Another placed pressure rollers on the surface of the pulley to prevent

derailment [65]. Lastly, [66] inserted stiff spiral springs in series within the sleeve and motor casing to ensure constant pre-tension. Efforts have also been made to prevent the derailment of the tendon using a control algorithm. Tendon driven systems with redundant tendons are generally controlled with optimization and null space between the tendon and joint space to maintain the tension above a certain level while controlling each joint with desired torque [5], [13], [67]. However, these methods are developed for tendon driven systems, in which the output tendon maintains positive tension and each tendon has pre-tension. This pre-tension provides the advantage of increasing stiffness for the pulley routed TDM. However, because of friction, pre-tension of the wire can be problematic when the tendon driven system is applied to a soft wearable robot. Therefore, this study suggests new type of tendon actuator called slack enabling tendon actuator which can prevent derailment of the tendon inside the actuator while allowing slack, non-positive tension, of output tendon [68]–[70].

Concept of Slack Enabling Tendon Actuator

The newly developed slack enabling tendon actuator [68]–[70] has advantages for soft wearable robots as described below.

1) Pushes the antagonistic wire so that it slacks decreasing the pre-tension of the antagonistic wire to zero and eliminating friction from the antagonistic wire.
2) Decreases unexpected position errors arising from the friction of the antagonistic wire on an underactuated system.
3) Avoid tendon derailment from the spool by preventing the slack of the tendon inside the actuator under any operating conditions.

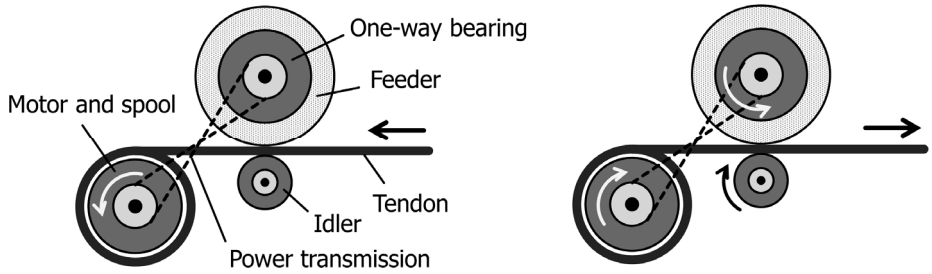

Figure 4-15 Concept of slack enabling mechanism: (**a**) winding; (**b**) releasing.

Figure 4-15 illustrates the concept of the slack enabling tendon actuator. The actuator primarily consists of four components: spool, feeder, idler, and tendon. The tendon is wound on the spool, which is connected to the output axis of the DC motor and passes between the feeder and idler; this provides friction force on the tendon. There are two one-way bearings inside the feeder and idler that selectively provide friction force on the tendon during winding and releasing. The feeder is actuated by a power transmission connected to the DC motor and the idler rotates passively. When releasing the wire, the feeder, which has a larger diameter than the spool, actively pushes the tendon to the outside of the actuator to maintain a certain level of tension on the tendon inside the actuator for preventing the derailment of the tendon from the spool. This mechanism can push the tendon outside the actuator even when there is no pre-tension on the output port of the tendon. When the actuator winds the tendon, the feeder and idler stop rotating and provide friction to the tendon to maintain the inner tension of the actuator. The spools for agonistic and antagonistic wires are stacked together on the same motor, and therefore, the mechanism can actuate a pair of tendons with one DC motor.

4.5.2 Tension Controller

The high bandwidth tension control is necessary to properly achieve the friction compensation using the feedforward compensation rule (4-17). The sign function in (4-18) makes T_c to follow the discontinuous tension with a large tension gap, ΔT_c, when T_s changes the pulling and releasing direction:

$$\Delta T_c = \pm \left| T_c\left(\delta = 1\right) - T_c\left(\delta = -1\right) \right| \tag{4-19}$$

which is around 30 N when T_s changes the pulling and releasing direction on 50 N with 360˚ bend angle for example. However, the abrupt change of the tension can generate vibration [71] and make the system unstable on some situations.

Plant Modeling

The dynamic equation of the system can be represented with a lumped parameter model:

$$m\ddot{x} + c\dot{x} + k\left(x - x_{eq}\right) + \gamma \,\mathrm{sgn}\left(\dot{x}\right) = u \tag{4-20}$$

$$T_{in} = k\left(x_{eq} - x\right) \tag{4-21}$$

where x is the displacement of the wire on the spool; x_{eq} is the displacement of the wire on the end-effector; m is the inertia of the system; c is the damping coefficient of the system; k is the stiffness of the wire; γ is the Coulomb friction of the actuator; u is the control input; T_{in} is the tension of the wire. Here, the stiffness of the wire (k) should become 0 when $x \le x_{eq}$ because the wire can only transfer the tensile forces.

The state space representation with $X = [x_1;\ x_2] = [x;\ \dot{x}]$ and $\mathrm{y} = T_{in}$ becomes:

$$\begin{bmatrix}\dot{x}_1\\ \dot{x}_2\end{bmatrix}=\begin{bmatrix}0 & 1\\ -\frac{k}{m} & -\frac{c}{m}\end{bmatrix}\begin{bmatrix}x_1\\ x_2\end{bmatrix}+\begin{bmatrix}0\\ \frac{1}{m}\end{bmatrix}u+\begin{bmatrix}0\\ \frac{k}{m}\end{bmatrix}x_{eq}+\begin{bmatrix}0\\ \Gamma\end{bmatrix} \tag{4-22}$$

$$\Gamma=-\tfrac{\gamma}{m}\cdot\tanh\left(\rho x_2\right) \tag{4-23}$$

$$y=\begin{bmatrix}k & 0\end{bmatrix}\begin{bmatrix}x_1\\ x_2\end{bmatrix}-kx_{eq} \tag{4-24}$$

where Γ is a nonlinear term related to the Coulomb friction of the feeder which is approximated to the hyperbolic function with the smoothing factor ρ as in (4-23). (4-22) can be written in a short form, $\dot{X}=A_pX+B_pu+E_px_{eq}+\bar{\Gamma}$ and $y=kC_pX-kx_{eq}$ where $A_p=[0\ \ 1;\ \ -k/m\ \ -c/m]$; $B_p=[0;\ \ 1/m]$; $E_p=[0;\ \ k/m]$; $\bar{\Gamma}=[0;\ \ \Gamma]$; $C_p=[1\ \ 0]$.

Control Design

Let the states of the controller $Z=[z_1;\ \ z_2]$ represent T_{in} and $\dot{T}_{in}$ respectively since the control objective is the convergence of T_{in} to the desired value. The error term, $e=T_{in}-T_s=\dot{w}$, is introduced as an integrating term of the controller. Then the control system in the state space representation becomes:

$$\begin{bmatrix}\dot{Z}\\ w\end{bmatrix}=\begin{bmatrix}A_p & 0\\ 1 & 0\end{bmatrix}\begin{bmatrix}Z\\ w\end{bmatrix}+\begin{bmatrix}B_p\\ 0\end{bmatrix}u-\begin{bmatrix}0\\ 1\end{bmatrix}T_s+d \tag{4-25}$$

$$y=\begin{bmatrix}1 & 0\end{bmatrix}\begin{bmatrix}Z\\ w\end{bmatrix} \tag{4-26}$$

Here, Γ in (4-22) is considered as a disturbance to the system and represented with $d=[\bar{\Gamma};0]$ in (4-25). The above equations can be written in the short form:

$$\dot{Z}_a=A_aZ_a+B_au-\begin{bmatrix}0; & 0; & 1\end{bmatrix}T_s+d \tag{4-27}$$

$$y = \begin{bmatrix} 1 & 0 & 0 \end{bmatrix} Z_a \tag{4-28}$$

The derived system is controllable since $\text{rank}([A_a \mid B_a]) = 3$. Then the full-state feedback control can be designed as:

$$u = -K_a Z_a \tag{4-29}$$

where K_a is a feedback gain with $Z_a = [\dot{z}_1;\ \dot{z}_2;\ \dot{w}]$. Now the closed loop dynamics of the control system becomes:

$$\dot{Z}_a = \left(A_a - B_a K_a\right) Z_a - \begin{bmatrix} 0; & 0; & 1 \end{bmatrix} T_s + d \tag{4-30}$$

The pole placement was conducted to determine K_a using '*place'* function on Matlab. Here, z_1 and w are the measurable signals using the tension sensor but z_2 is not. Also, the disturbance, d, in (4-30) should be rejected to get a desired closed loop dynamics of the system.

Therefore, a disturbance observer is adopted to estimate z_2 and eliminate the disturbance, d. The disturbance, d, can be modeled using the states X_d as:

$$\dot{X}_d = A_d X_d \tag{4-31}$$

$$\hat{d} = C_d X_d \tag{4-32}$$

with the assumptions that $A_d = [0\ \ 1; 0\ \ 0]$ and $C_d = [1\ \ 0]$. Then the augmented system consist of the states $Z = [z_1;\ z_2]$ and X_d can be composed:

$$\begin{bmatrix} \dot{Z} \\ \dot{X}_d \end{bmatrix} = \begin{bmatrix} A_p & B_p C_d \\ 0 & A_d \end{bmatrix} \begin{bmatrix} Z \\ X_d \end{bmatrix} + \begin{bmatrix} B_p \\ 0 \end{bmatrix} u \tag{4-33}$$

$$y = \begin{bmatrix} C_p & 0 \end{bmatrix} \begin{bmatrix} Z \\ X_d \end{bmatrix} \tag{4-34}$$

The above equations can be reduced to the simple forms; $\dot{Z}_t = A_t Z_t + B_t u$ and $y = C_t Z_t$. Then the disturbance observer for the augmented system (4-33) and (4-34) can be composed as (4-35) since the states are observable; $\text{rank}([C_t;\ C_t A_t;\ C_t A_t^2]) = 4$.

$$\dot{\hat{Z}}_t = A_t \hat{Z}_t + B_t u + L_d \left(y - \hat{y} \right) \tag{4-35}$$

where the symbols with hat ($\hat{Z}_t$ and $\hat{y}$) are the estimation of the corresponding symbols. And L_d is the gain of the disturbance observer that can be determined with the pole placement for the closed loop observer dynamics, $\dot{e} = (A_t - L_d C_t)e$, where $e = Z_t - \hat{Z}_t$. Then the resulting control law for the tension tracking becomes:

$$u = -K_a \hat{Z}_a - \hat{d} + B_r T_s \tag{4-36}$$

Experimental Results of Tension Control

The experiments were conducted to see the response of the proposed tension controller for the slack enabling actuator. The tension controller designed in the previous section was converted to the discrete-time system and implemented to the real-time control system (cRIO-9082, National Instruments). The poles of the controller were finely tuned so that the tension of the actuator converges without overshoot and vibration of the system. **Figure 4-16** represents the experimental results of the step (1–10 N) and the sinusoidal (0–50 N) responses for the proposed tension control system. It showed a rise time of 36.0 ms which is enough as the tension source for the Bowden-cable tension control system.

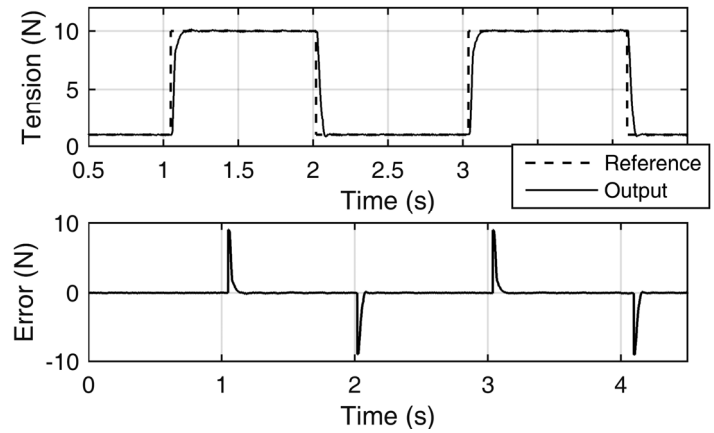

(**a**)

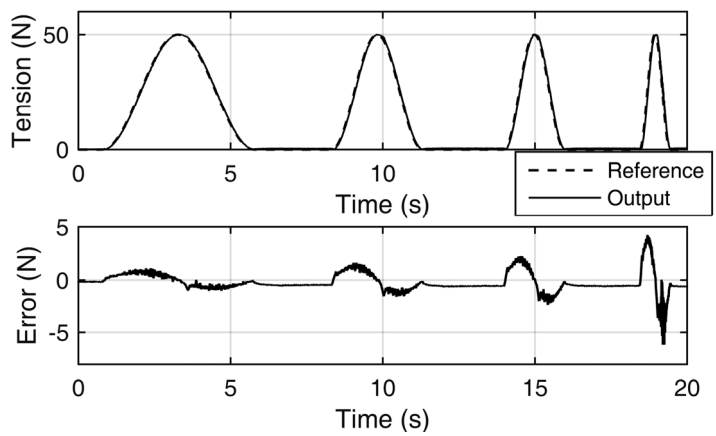

(**b**)

Figure 4-16 (**a**) The step response and (**b**) the sinusoidal responses of the tension controller for the slack enabling actuator.

4.5.3 Zero-Tension Controller

The mechanical stability of the actuator when the wire slack was provided with the slack enabling mechanism as described in the previous section. The actuator can easily provide the tension down to zero without the failure when the position based controller is used [69], [70].

However, the tension controller can diverge around zero tension due to the noise

(**Figure 4-17**) and the bias error (**Figure 4-18**) of the tension sensor and the characteristic of the wire that act as a linear spring providing only tensile force, not compression force. The measured tension from the tension sensor can be represented as $\tilde{T} = T + \varepsilon$, where T is the actual tension of the wire and ε is the sensing error that consists of the white noise and bias. The general rule for the reference tracking of the tension is using a control error, $e = T_s - \tilde{T} = (T_s - \varepsilon) - T$. In here, the control error becomes negative definite if $\varepsilon > T_s$ and it causes divergence of the control system because T should be always positive semidefinite. In a practical situation, if there exist a small value of positive ε in the tension sensing system, the reference input $0 \leq T_s < \varepsilon$ causes the failure of the actuation system with continuous negative control input. The simplest solution could be turning off the controller when T_s is smaller than ε, but the tension can remain high over ε when the reference tension decreased abruptly because of the friction inside the actuator. Also, the turned off controlled system is not backdrivable when the pulling force is exerted on the wire; the force higher than the friction should be applied to backdrive the actuator. Furthermore, merely constraining T_s to be larger than ε cannot enable slack on the system. Therefore, a zero-tension controller is required so that the slack enabling actuator can be used as a tension source that can cover the slack. The zero-tension controller mainly consists of two parts as described below.

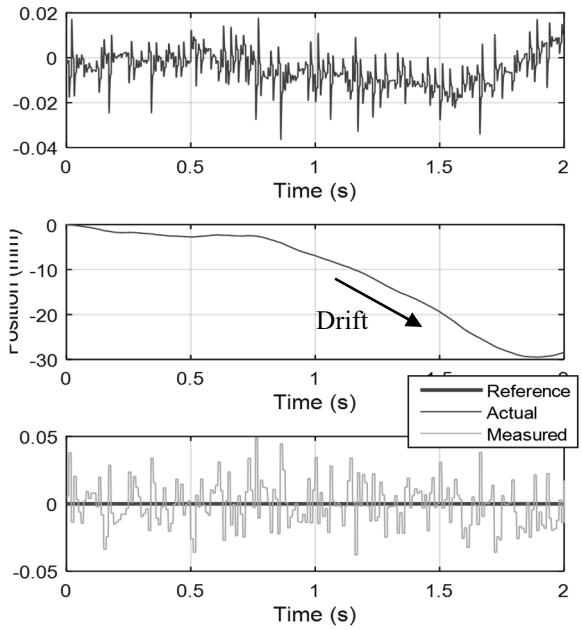

Figure 4-17 Simulation result that shows the drift of the wire position when the tension setpoint is zero with the white noise (0.05 N amplitude) on the tension measurement. The actual tension on the bottom graph is always zero.

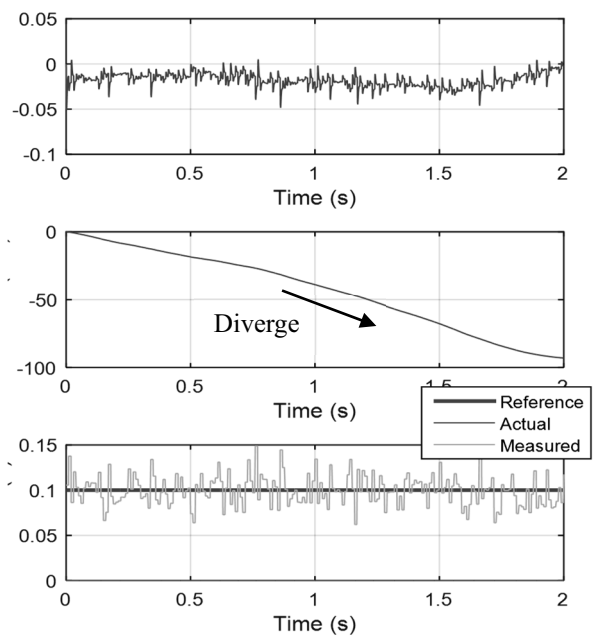

Figure 4-18 Simulation result that shows the divergence of the system when the tension setpoint is zero with the white noise (0.05 N amplitude) and the bias (0.1 N) on the tension measurement. The actual tension on the bottom graph is always zero.

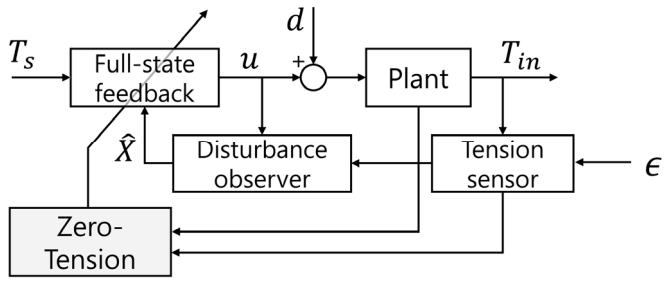

Figure 4-19 The concept of the zero-tension controller that regulates the control gain of the tension controller to make the controller stable on zero-tension using the tension and position feedback.

1) Run-down Speed Regulation

$$\textit{if } \{\tilde{T} < T_{th} \;\&\&\; v_{th} < \dot{x}\}$$

$$\textit{do } \{\textit{reset integrator;}\}$$

Restrict the winding speed of the wire (by resetting the integrator when the wire speed, $\dot{x}$, exceed the threshold speed, v_{th}) if the wire is in slack state (measured tension is lower than the threshold tension, T_{th}) to prevent the overshoot which can make the system unstable when the positive reference tension is provided on the slack state. In here, T_{th} is set to be a maximum expected value of ε.

2) Zero-Tension Regulation

$$\textit{if } \{0 < T_s < T_{th} \,||\, (T_s \leq 0 \;\&\&\; T_{th} < \tilde{T})\}$$

$$\textit{do } \{T_s = T_{th};\}$$

$$\textit{else if } \{T_s \leq 0 \;\&\&\; \tilde{T} < T_{th}\}$$

$$\textit{do } \{T_s = 0;\ u = 0 \textit{ if } u < 0;\}$$

When the reference tension (T_s) is set to be between 0 and T_{th}, forces the reference tension to be T_{th} because the tension is uncontrollable between 0 and positive value of ε. In addition, forces the reference tension to be T_{th} if the reference tension is set to 0 and measured tension is higher than T_{th} due to the friction inside the actuator. And constrain the negative control input (u) when the reference tension is set to zero so that the controller is stable on the slack state. Implementation of the proposed algorithm makes the system stable and backdrivable event though the reference tension is set below ε.

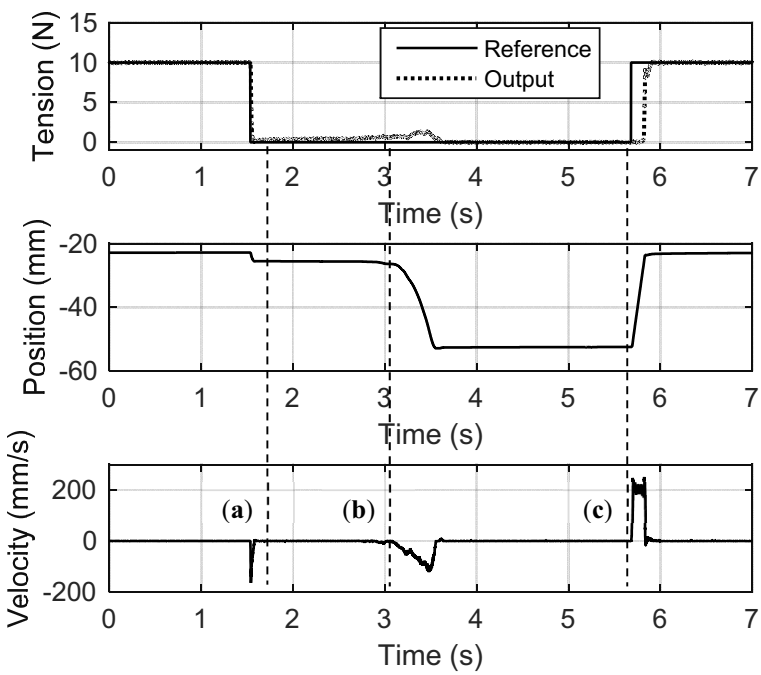

Figure 4-20 The experimental result of the zero-tension controller. (**a**) The tension setpoint is set to zero and it does not show instability as in **Figure 4-17** and **Figure 4-18**; (**b**) The wire is pulled by hand and it shows backdrivable interaction; (**c**) The tension setpoint is set to 10 N. The position of the wire increases with the threshold speed 20 mm/s until the slack of the wire is eliminated and the tension converges to 10 N without the overshoot.

4.6 Experiments

4.6.1 Experimental Setup

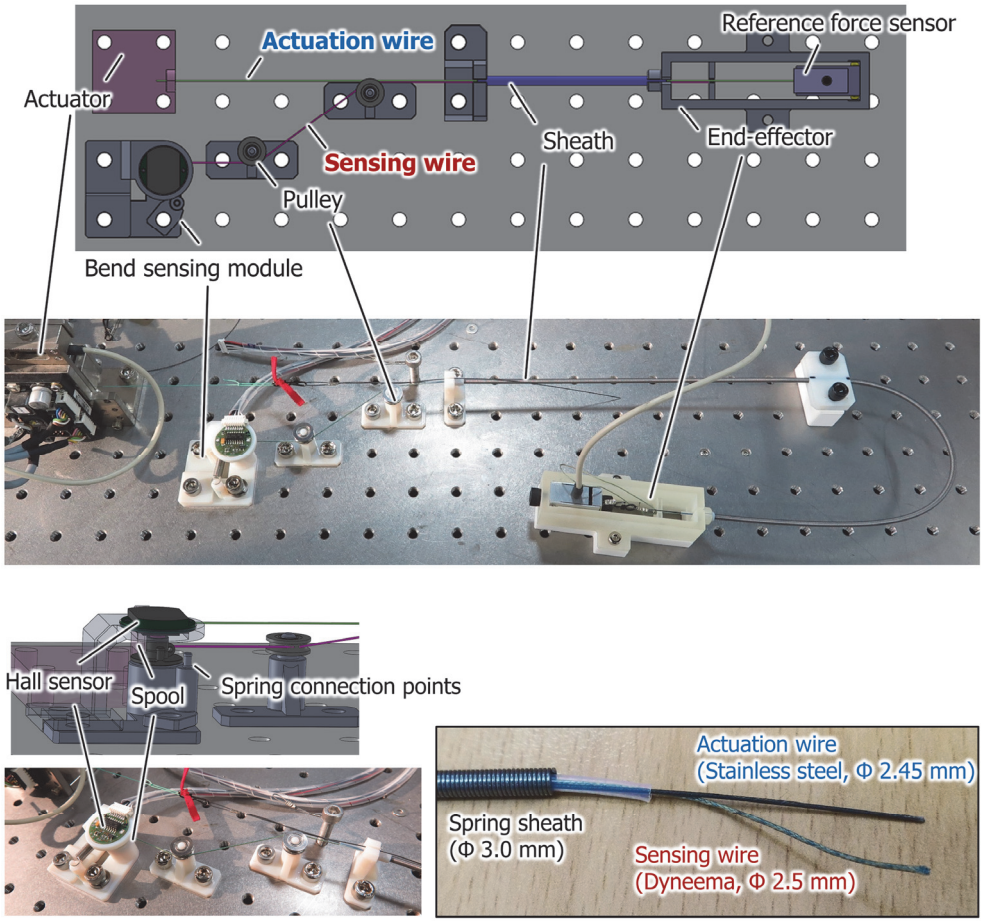

Figure 4-21 Experimental setup for the Bowden-cable control system, consisting of an actuator, actuation wire, bend sensor, sensing wire, sheath, and end-effector.

An experimental setup (**Figure 4-21**) was designed to verify the performance of the proposed concept. A tension-controlled tendon actuator consisting of a DC motor (RE25, 20W, Maxon motor), spool (5 mm radius), and tension sensor was used to generate the desired input tension, Tin, to the Bowden-cable (the setup can generate up to 50 N with a 5.4:1 gear ratio). The stainless steel actuation wire (#2019, 0.457

mm; Sava Industries, Inc.) from the tendon actuator was connected to the reference output tension sensor on the end-effector through the Bowden-cable (340×3.0×2.0 mm) and a Teflon tube (1.38×1.88 mm). One end of the sensing wire (braided Dyneema, 0.45 mm) was wound around a sensing spool that is connected to the linear spring, providing restoration torque to the spool to keep the sensing wire taut. Then the displacement change of the sensing wire could be calculated from the rotational angle of the spool, which was measured with a Hall-effect sensor (RMB20IC, RLS). Signals were measured and processed with an FPGA and a real-time engine (cRIO-9082, National Instruments Corp.). The tension of the tendon actuator was controlled with a PID control on the FPGA together with the current control mode of the ESCON motor driver (Maxon motor). All components could be embedded in one module for a compact actuation system but for the convenience of the experiment they were placed on a separate breadboard.

4.6.2 Results

Bend Estimation

An experiment was conducted to determine the effect of actuation tension on the displacement change of the sensing wire due to the sheath compression. Actuation tension from 1 N to 50 N was applied, and the encoder signal indicating the displacement of the sensing wire was measured to see how the sheath compressed. This experiment was conducted with three bend angles (0˚, 90˚, and 180˚) to check whether the bend angle of the sheath affects compression and the estimation model (4-1) is reasonable. It is shown in **Figure 4-22** that the displacement of the sensing wire increases as the input tension of the actuation wire increases. There exists a hysteresis in the relationship between the input tension and the displacement change which originated from friction along the wire and the compression of the parts as described in the previous chapter. The compression can be compensated to estimate

the bend angle with the bend estimation model in **Chapter 4.2** using the stiffness parameter of the system K_{in} = 220 N/mm; K_s = 800 N/mm; K_{out} = 170 N/mm.

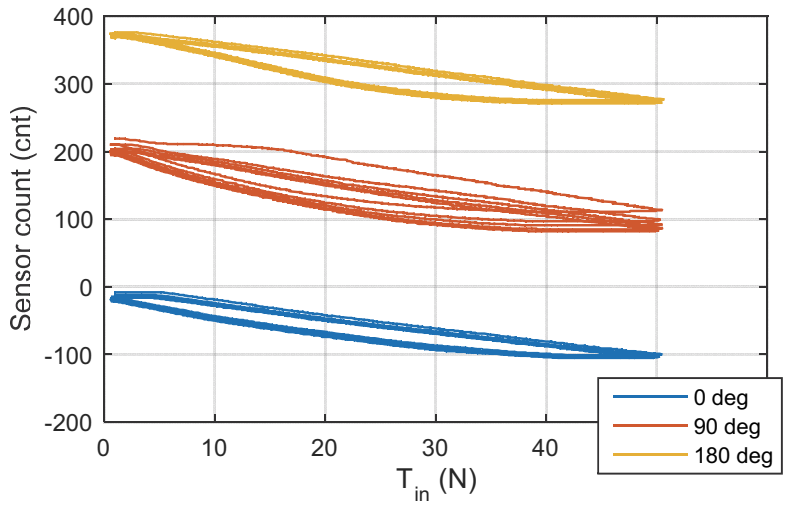

Figure 4-22 Experimental result of sensing wire length changes with varying input tension of the actuation wire and the accumulated bend angle of the sheath.

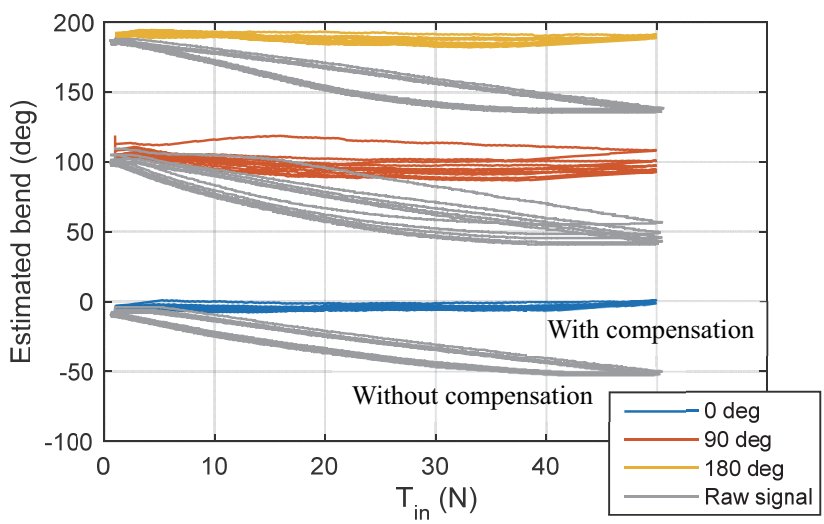

Figure 4-23 Bend angle estimation of the sheath using the sensing wire with and without sheath compression compensation.

Figure 4-23 is the result of bend estimation described in **Chapter 4.2** using the sensing data in **Figure 4-22**. The blue, orange, and yellow lines indicate the result of the compression compensation, and the gray line shows data obtained without compensation. The mean values of the compensated estimates of the top, middle, and bottom bend angles depicted in **Figure 4-23** are –7.1˚, 96.5˚, and 184.2˚, respectively. The standard deviations for the top, middle, and bottom bend angles depicted in **Figure 4-23** are 4.5˚, 9.3˚, and 5.5˚, respectively. The elaborate calibration of the sensing system and the hysteresis modeling could decrease the estimation error. However, the result presented here is acceptable for a rough estimation.

Tension Control with Bend Estimation

The experiment was conducted using the proposed Bowden-cable system with the output force (T_{out}) sensor as a reference. The tension setpoint (T_s) was given from 0 to 40 N while the cable was bent from 0 to 400˚. The shape of the sheath was kept constant as the setpoint increased and came back to zero tension. The results for the time domain and the tension domain are represented in **Figure 4-24** and **Figure 4-25**, respectively.

The uppermost plots in **Figure 4-24** and **Figure 4-25** show the relation between T_s, T_{in}, and T_{out}. The relation between Tin and Tout can be considered to be the input and output relation when there is no compensation. The uppermost plot in **Figure 4-25** shows the input and output characteristics of the Bowden-cable transmission that is described by the friction model in (3-21). It is shown that the slope of input and output decreases as the bend angle increases during the tension-increasing phase and vice versa for the tension-decreasing phase.

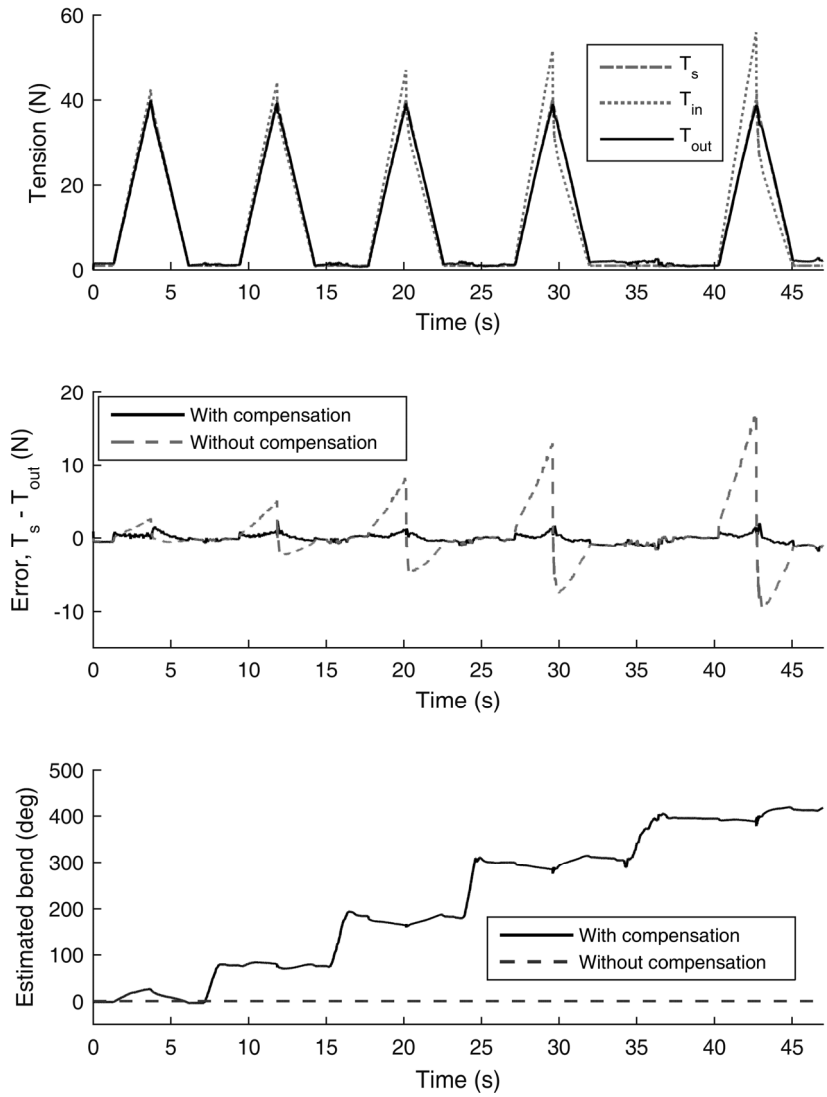

Figure 4-24 Experimental result showing the tension of the setpoint, input, and output at different accumulated bend angles of the sheath over time.

The lower plots of **Figure 4-24** and **Figure 4-25** show the estimated bend angle of the sheath calculated from the displacement change of the sensing wire and input tension. The estimated bend angle shows the amount of sheath deformation, although there are an estimation error and hysteresis (the fluctuations of the estimation are 24˚ and 29˚ for a 0˚ and 400˚ bend angle, respectively) due to the rough compression

model of the sheath. However, this error could be decreased with more accurate modeling because it shows the consistent tendency.

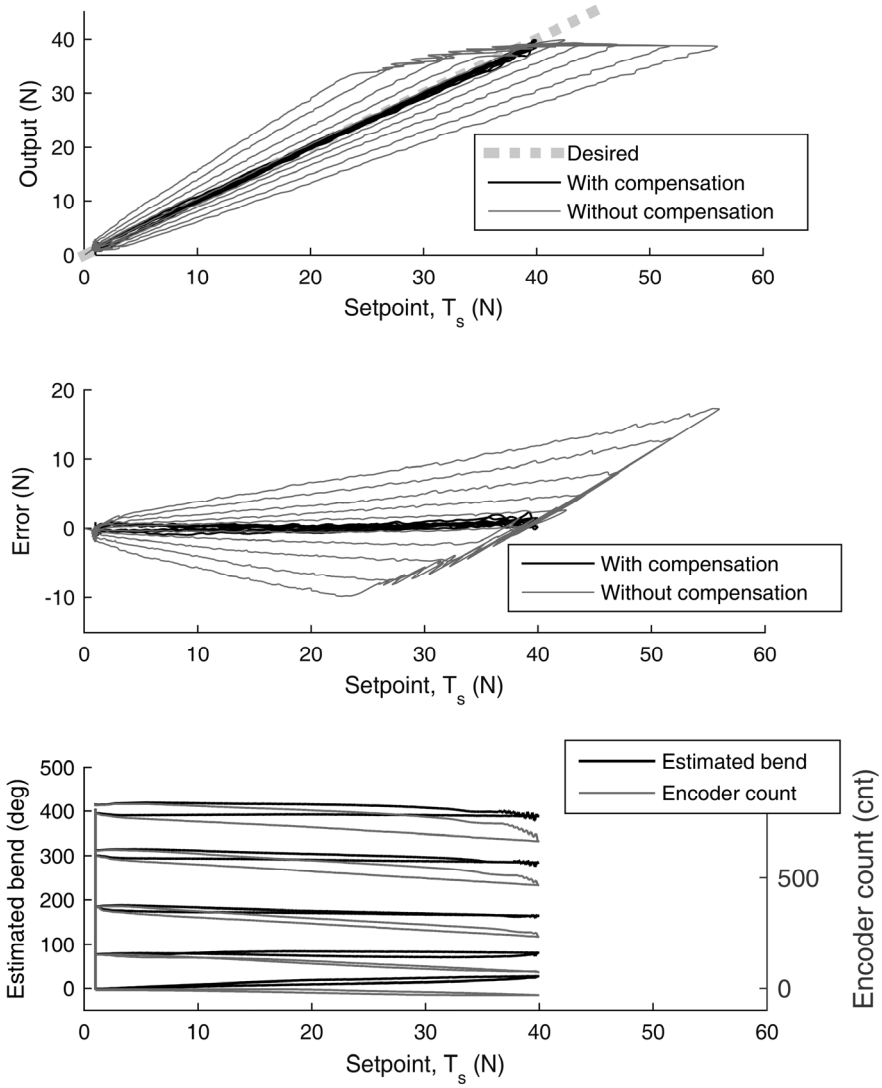

Figure 4-25 Results for feedforward force control with bend estimation.

The relation between T_s and Tout describes the tension-tracking performance of the proposed method. As the bend angle of the sheath increases, it is shown that the

amount of increment and decrement of T_{in} increases to overcome friction along the cable. As a result, the output of the system (T_{out}) follows the desired reference tension (T_s) with an RMS error of 0.50 N, which is 1.25% of the maximum setpoint (40 N). This error is 90.4% lower than the RMS error of 5.21 N when there is no compensation.

The abrupt change of the input tension originating from the switching compensation rule causes some vibration on the input tension that increases the tracking error and decreases the stability margin of the system. Full-state feedback tension controller used in this study has insufficient bandwidth. A robust and high bandwidth tension controller is needed for the higher performance of the system.

Chapter 5 Implementation and Application

5.1 Exo-Glove

Exoskeleton robots have been developed for various purposes, including daily assistance, rehabilitation, and force augmentation. Assistive wearable robots require compact design for daily use. Additionally, robots for rehabilitation and force augmentation require a high degree of freedom. Both these types of robots require compact design for practical usage. This requires the robot to have a small volume per unit degrees of freedom.

TDMs have great advantages for soft wearable robots. The soft wearable robot [2], [69], [72] is an emerging type of wearable robot, which consists of soft fabric for its structure and flexible power transmission. It is a type of wearable actuator because the actuator and transmission directly work on body parts and the soft structure holds the shape of transmission. However, precise control of soft wearable robots is difficult to achieve because of its inherent characteristics, which consist of soft, easily deformed material. However, these robots have the advantages of compact and light design [1], [2], [73], [74], compared to conventional wearable robots with rigid links and rigid transmission. These advantages may lead soft wearable robots to be used in daily life by people requiring simple assistance and ease usability.

Figure 5-1 shows examples of sheath paths when soft tendon routing [1] is applied to an upper limb soft wearable robot. Because the bending angle of the sheath continuously changes during operation, it is almost impossible to estimate the friction force unless there is a special sensor to measure the summation of bent angles of the sheath for each segment. In addition, unlike robots with rigid links which can adopt traditional strain gauge based force sensor, there are few flexible sensors that

can be attached to next skin or soft fabric. This results in unexpected modeling errors and degradation of control performance.

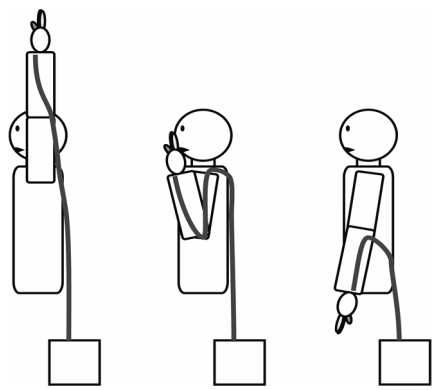

Figure 5-1 Examples of sheath path bending on soft wearable robot. (**a**) 0; (**b**) 2π; (**c**) π

5.1.1 Influence of Antagonistic Tension of the Wire

Pre-tension of the antagonistic wire creates friction force on the Bowden cable, which arises from the contact surface between wire and sheath as the Bowden cable bends. Decreasing the friction force of antagonistic wire can increase the posture accuracy of the soft tendon routed system. In TDMs, the minimum number of wires should be $n + 1$ or $2n$, where n is degrees of freedom of the system, to fully constrain the kinematics of the mechanism because the wire can only pull and cannot push [14]. If the actuation wires cannot constrain the mechanism, there should be passive components, such as springs, to make the system controllable; this is designated the underactuated mechanism [16]. When we consider a wearable robot, which is a combined system with a human body and a transmission, the spring-like passive properties of human body joints [75] act as passive components of the system. Thus, the antagonistic wire does not need to flex the finger as shown in **Figure 5-2**. In this

case, the posture of the joints and links is determined by the position of the tendon, while joint torque exerted by the tension of the wire and torque by passive property attempts to create equilibrium through the constraint of the position of the tendon. Therefore, the unmeasured tension of the antagonistic wire arising from friction exerts a disturbance on the system.

An example for the case of a soft wearable robotic hand will be discussed. **Figure 5-2** provides a schematic of an index finger, consisting of four links and three joints with torsional springs representing the passive elastic property of finger joints. The equilibrium posture and the stiffness arising from the passive property were referred from the previous study on human finger [75]. Additionally, there are two tendons in the soft wearable robotic hand for flexion and extension of a finger. The flexion tendon is attached next to the DIP joint and acts as agonist wire, and the extension wire is attached next to the PIP joint and acts as antagonist wire.

As the agonist tendon is pulled to flex the finger, the posture of the finger follows an angle that satisfies torque equilibrium.

$$\tau = P(\theta)T + \tau_p(\theta) = 0 \tag{5-1}$$

where P represents a 3 × 2 Jacobian matrix relating joint torque and wire tension; T represents the tension of the agonist and the antagonist wires [T_{an}; T_{ant}]; and θ represents the angle of each of the three joints. The elastic passive property of the finger, τ_p, and the kinematics of the joint tendon system are adopted from previous studies [75], [76].

The friction force exerted by antagonistic wire is defined as

$$T_{atg} = T'_{atg} \exp(\mu\phi) \tag{5-2}$$

Here, T'_{atg} represents the remaining tension of the antagonistic wire on the actuator side and is set to 10 N; μ is defined to 0.1 which is the value between steel

and Teflon; ϕ is set to 0–2π, representing the cases in **Figure 5-1**.

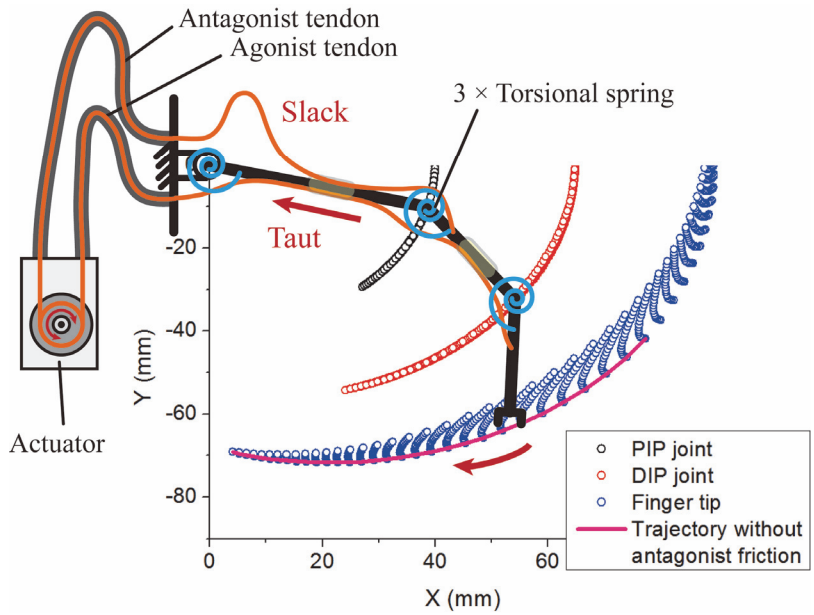

Figure 5-2 Simulation result of finger trajectory while winding agonist tendon and exerting the friction of antagonist tendon.

Figure 5-2 shows the simulation results of the way the friction force of the antagonistic wire affects the posture changes of the finger. The curved and dotted lines represent the trajectory of the finger for cases in which only the agonist tendon exerts and when friction force from the antagonist wire additionally exerts, respectively. The results indicate that an error of trajectory of fingertip originating from the friction of antagonistic wire has approximately 10 mm, which is a sufficient error to influence grasping stability.

Eliminating the antagonistic tension of the wire provides the additional advantage of increasing the position accuracy of the system for the soft wearable robot. Unlike the rigid structure of conventional robots, the fabric used as the structure and routing strap of the soft wearable robot [1] can be easily deformed

when the transmission exerts force to the system, as illustrated in **Figure 5-3**.

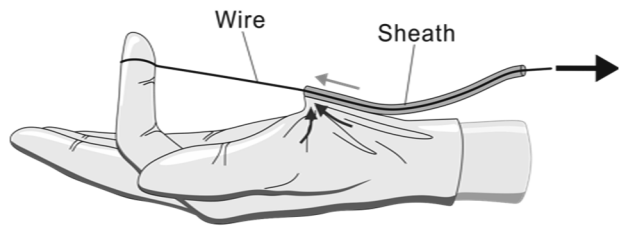

Figure 5-3 Example of deformation of soft wearable robot.

Therefore, excessive force originating from the friction of the antagonistic wire causes deformation of the structure. Considering the difficulty of a lack of suitable proper sensors for end-effectors or joint position feedback controls for soft wearable robots, the deformation of the structure generates excessive errors in position control. Although the deformation of the structure cannot be avoided for soft wearable robots, it should be minimized by eliminating unnecessary forces exerted by tendons.

5.1.2 Grasping Force with Different Arm Postures

The proposed actuation system was implemented (**Figure 5-4**) on the Exo-Glove Poly [77] which is the polymer version of the Exo-Glove [1]. The proposed bending sensing system can be embedded inside the preexisting Bowden-cable actuation system without adding or modifying the structure of the glove. The sensing wire (braided Dyneema, 0.45 mm) was inserted into the sheath of the actuator side and fixed to the branching part in **Figure 5-5**. The actuation wire and the sensing wire of the actuator side were connected to the bending sensing and tendon actuation setup in **Figure 4-21**.

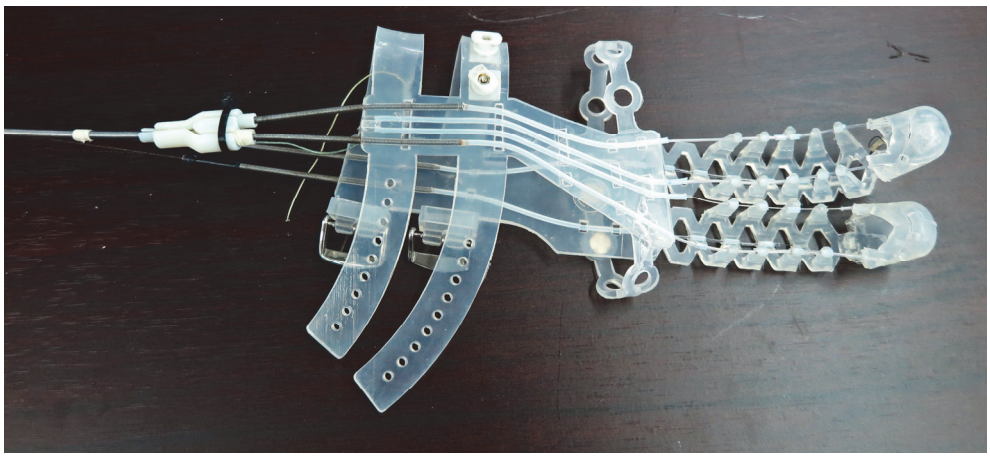

Figure 5-4 The Exo-Glove Poly [77] with the embedded bending estimation system.

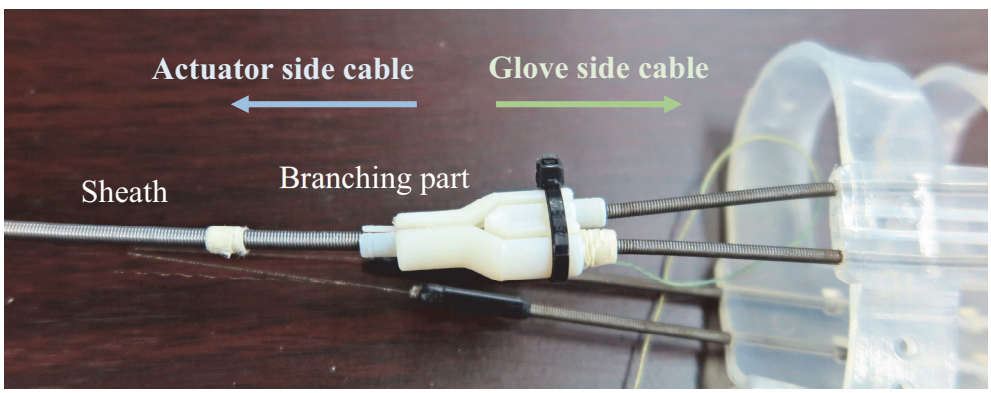

Figure 5-5 Branching part of the Exo-Glove Poly that the one end of the sensing wire is fixed on. The actuator side of the cable consists of the sheath, Teflon lining, actuation wire, and sensing wire while the glove side of the cable does not have the sensing wire.

The grasping force was measured (**Figure 5-6**) with and without the proposed actuation method for the three different arm postures (**Figure 5-7**) that involve different sheath shapes which occur in the operation of the glove. Four periods of sinusoidal tension setpoint, 0–40 N, was given to the system with each arm posture.

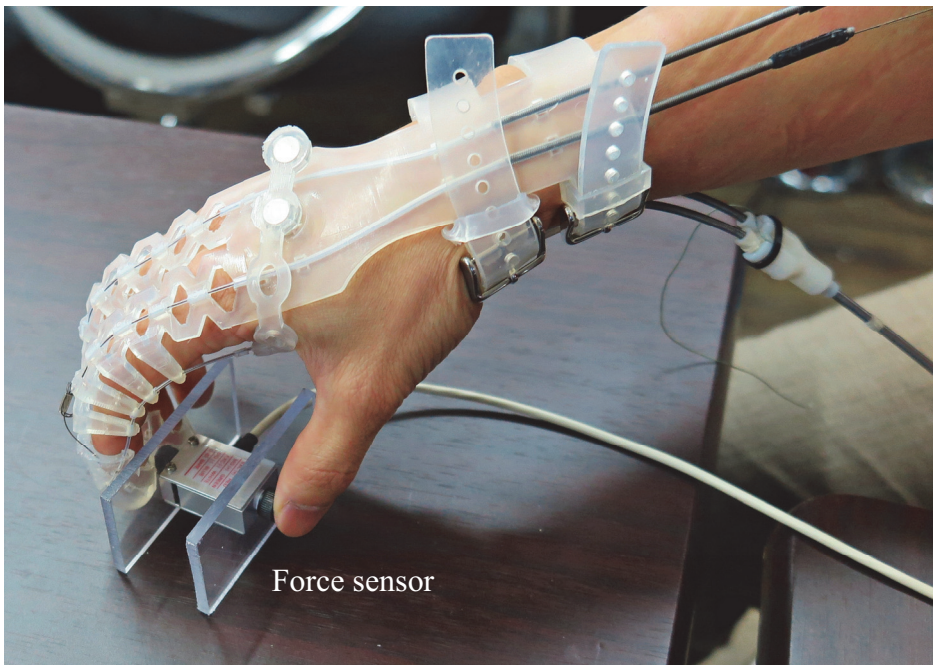

Figure 5-6 Grasping force measurement using the force sensor (100 N capacity, Ktoyo) and the polycarbonate plate.

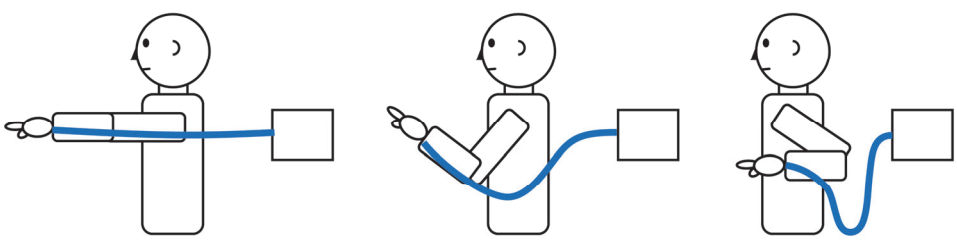

Figure 5-7 Three different arm postures that involve different bend angles of the sheath. (**a**) $\phi \approx 0$; (**b**) $\phi \approx \pi$; (**c**) $\phi \approx 2\pi$.

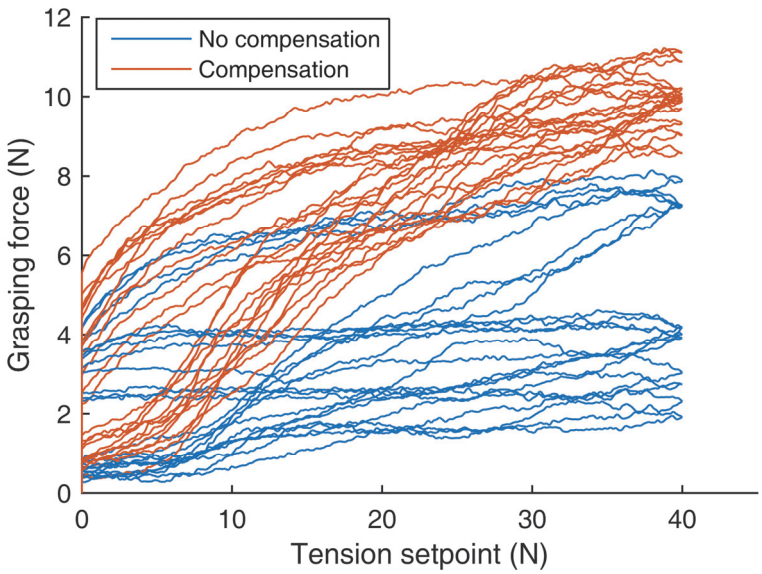

Figure 5-8 The measured grasping force of the Exo-Glove Poly, not using (blue) and using (orange) the proposed actuation method with three different arm postures.

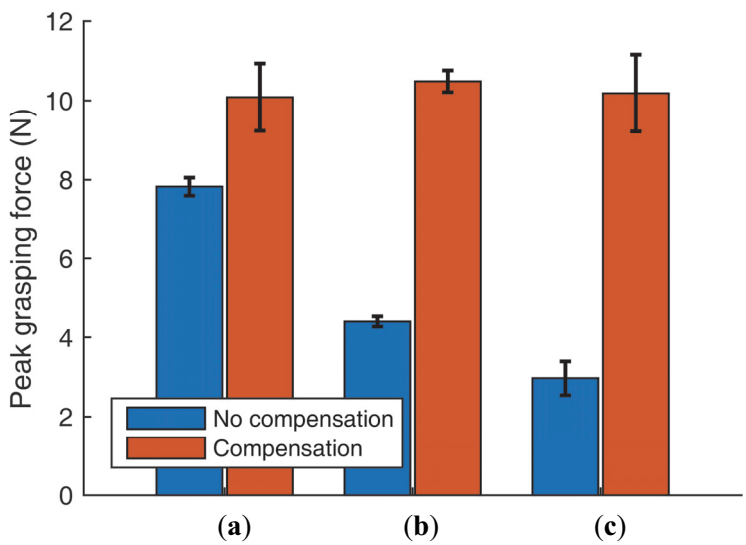

Figure 5-9 The peak grasping forces measured with three different arm postures **a**, **b**, and **c** in **Figure 5-7**, not using (blue) and using (orange) the proposed actuation method.

Figure 5-8 and **Figure 5-9** show the experimental results of the grasping force measurement with different arm postures. The blue lines and bars in figures are the results of without compensation and the orange lines and bars are the results of with the proposed compensation method. The results show that the relation between input tension of the wire and the grasping force varies as the arm posture changes if there is no compensation. As the arm bends from **Figure 5-7 a** to **c**, the accumulated bend angle of the sheath increases from around 0 to 2π increasing the friction along the cable. The peak grasping force without compensation (blue bar) exponentially decreases as the arm bends and this inconsistency of the grasping force limits the application of the glove. For example, the glove could exert excessive force to the grasping object when the sheath is straight or lack of grasping force when the sheath is bent a lot. On the other hand, the result with the proposed method (orange lines and bars) maintains the grasping force consistent although the posture of the arm and the sheath configuration changes. The hysteresis on the relation between the setpoint tension and the grasping force (**Figure 5-8**) implies the nonlinearities of the glove and finger properties and it could be further improved by the upper-level control strategy of the gloves with the proposed sheath shape robust tension actuation method.

5.2 Endoscopic Forceps

One future application of the proposed Bowden-cable actuation system is the flexible endoscopic forceps that consist of the spring sheath, actuation wire, and the gripper. The endoscopic forceps have been used for the biopsy through the natural orifices (i.e. mouth, anus, vagina, etc.).

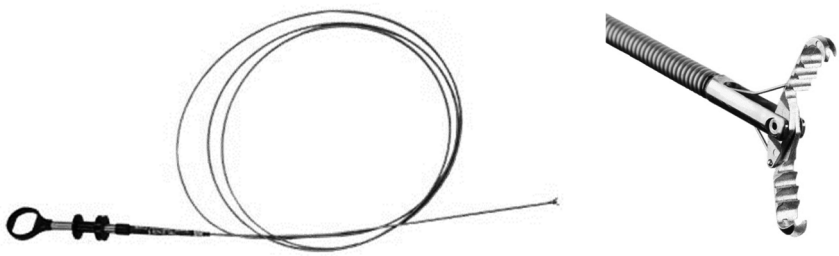

Figure 5-10 The endoscopic forceps that consist of the spring sheath, actuation wire, and gripper. (US Endoscopy [78])

In these days, natural orifice transluminal endoscopic surgery (NOTES) [79]–[81] has been gradually operated to get rid of a keyhole for the tool insertion and unsightly scars on the patient's body. The NOTES (**Figure 5-11**) employs endoscope with multiple channels to engage with several tools (the forceps, a camera, an infuser, etc.). The previous application of the endoscopic forceps is limited to the biopsy since the grasping force of the forceps cannot be accurately controlled. The accurate control of the endoscopic forceps became an important issue since only the visual feedback of the surgeon has limitations [82]. **Figure 5-12** shows the schematic of the endoscope through the mouth and reached to the stomach. The endoscope inside the stomach experiences complex routing path which highly affects the friction properties of the grasping and the wire driven devices. The proposed actuation scheme could be applied to the wire driven endoscopic system for more accurate tension and force control of the endoscopic devices.

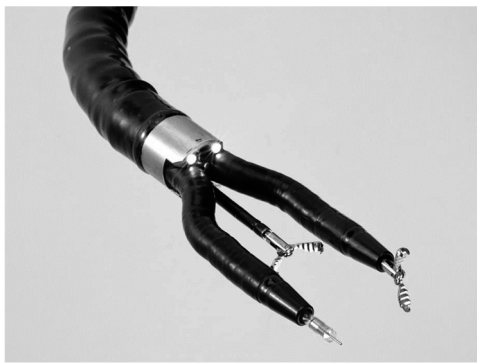

(**a**)

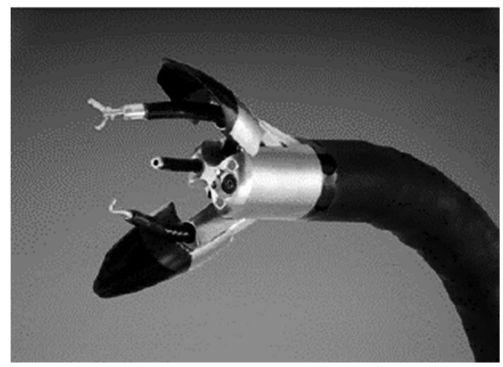

(**b**)

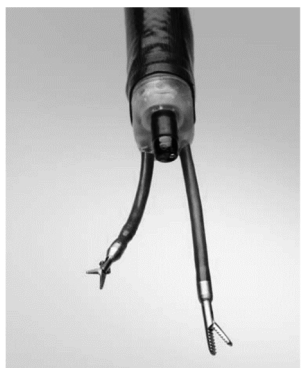

(**c**)

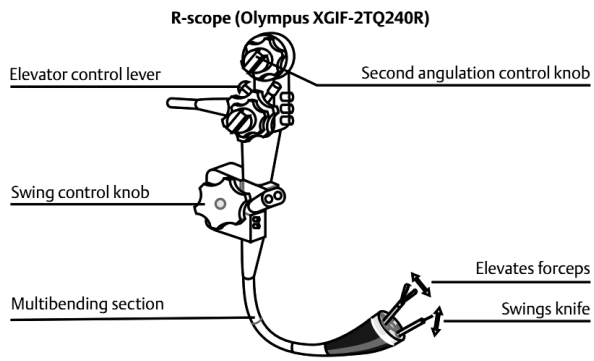

(**d**)

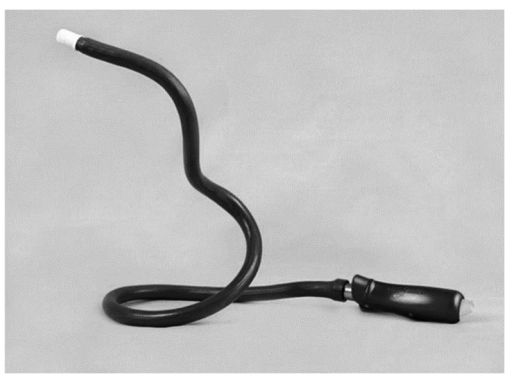

(**e**)

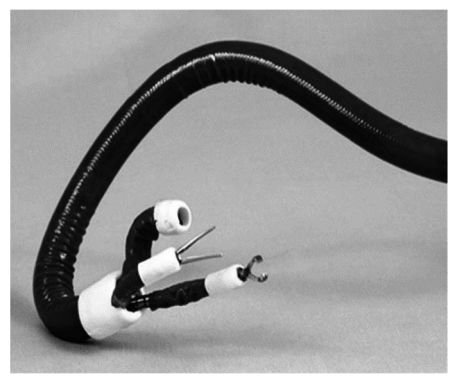

(**f**)

Figure 5-11 (**a**) EndoSamurai [83] (Olympus Corp., Tokyo, Japan); (**b**) Anubis scope® [84] (Karl Storz, Tuttlingen, Germany); (**c**) a "fourth generation" endoscopic platform [85] (Boston Scientific Corp., Natik, USA); (**d**) the R-scope [86] (XGIF−2TQ240R; Olympus Corp., Tokyo, Japan); (**e**) ShapeLock Endoscopic Guide [87] (USGI Medical, Inc., San Clemente, USA); (**f**) ShapeLock Cobra [87] (USGI Medical, Inc., San Clemente, USA)

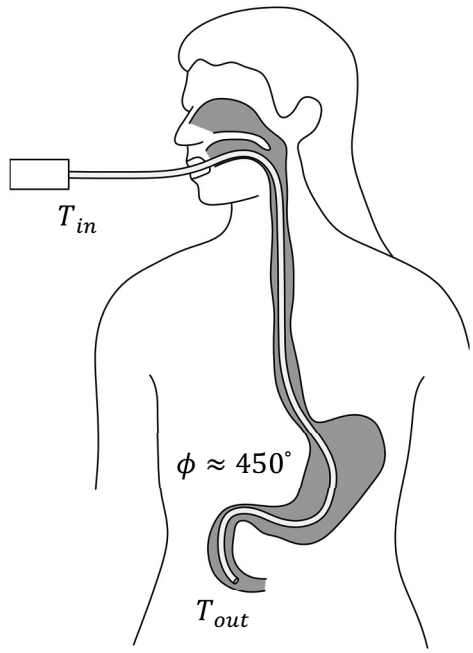

Figure 5-12 The insertion of the endoscope through the mouth that requires complex routing path along the organs.

Chapter 6 Concluding Remarks

This dissertation proposed a novel actuation system for the Bowden-cable transmission. The basic idea is using an actuation wire and a sensing wire inside the same sheath to transmit the power and estimate the varying shape of the cable at the same time. Then the shape dependent hysteresis can be compensated with a feedforward control manner.

A new type of bending sensing methodology is proposed in **Chapter 2** that uses a Bowden-cable and a displacement sensing element. The basic principle of the sensor is based on the displacement change of the inner wire when the bend angle of the sheath changes, which previous studies have considered to be an error. It has been shown that the output signal of the sensor has high linearity with the bend angle and can measure a wide range of accumulated bending angles with large curvatures. The proposed bending sensing technique has four main advantages over previous bend sensors, including Flex sensors and optical fiber-based sensors. First, it can be embedded inside the previous Bowden-cable actuation system without increasing the size, weight, and complexity of the system. Second, it is low cost. The design and manufacturing process for the proposed sensing system are very simple. It can be easily made in laboratories with cheap and affordable parts that do not require any special fabrication technique. Third, it is easy to use. It does not need complicated signal processing because the bend angle of the sensor is proportional to the output signal of the displacement sensing module. Fourth, it can measure a wide range of bend angles and curvatures (up to 450° bend angle and 80.0 m^{-1} curvature for the first prototype). The sensor signal is linear with large curvatures (R-square value up to 0.9969 with a curvature 80.0 m^{-1}), and the length of the sensor can be easily extended to measure large angles. Nevertheless, the proposed method has some

limitations. Some non-linearity, which is shown in the initial bend of the sensor, can accumulate if the sensor is subjected to multiple bend points. However, many applications that use other types of bend sensors do not involve multiple bend points. Also, some sensor nonlinearities can be compensated for with more precise modeling and calibration, because the signal is repeatable. Despite these limitations, the proposed sensor is expected to overcome the usability and accessibility deficiencies of Flex sensors and optical fiber-based sensors. Many existing studies can be further developed by using the proposed bend sensor for more precise control of a Bowden-cable [1], [2], [6]–[10], [24], [56] or to obtain bend feedback from soft-bodied structures like soft robots [88], [89].

A novel Bowden-cable actuation system is proposed in **Chapter 4** that has four main advantages over previous studies. First, it can deal with the varying shape of the Bowen-cable. The flexible characteristic of the Bowden-cable is highly restricted if it cannot be used in situations that allow the shape of the cable to change. Second, it does not require sensors to be placed on the output port of the cable to measure output tension or position. In other words, it eliminates the need for a sensor on the end-effector to help minimize the size and complexity of the end-effector. Third, it does not require an additional sensor body to be placed on the sheath to measure the bend angle. The bend-sensing system is embedded in the same sheath as the actuation wire, which enables the simple design of the whole system. Fourth, the proposed bend-sensing system is low cost. The proposed system for the Bowden-cable adds only a few dollars to the whole system. This is very cheap compared to the FBG-based sensing system that is commonly used in shape sensing systems. However, this study has the limitation that the proposed method is an estimation and modeling-based approach. It strongly relies on friction modeling of the Bowden-cable, which has some uncertainties. The friction coefficient of the cable changes over a period of time, which requires periodic calibration of the system. In addition, system

robustness to external disturbances should be further studied, including the effect of configuration change during actuation and interference between the two wires. Notwithstanding these limitations, the proposed actuation system is expected to contribute to applications that require a minimized system size and hysteresis compensation with an affordable price. The examples of such applications include wearable robots, catheters, and endoscopes.

Appendix A

Taylor series expansion of (2-9)

$$\mathrm{X}(\mathrm{K}) = \frac{\sqrt{2\{1-\cos(\mathrm{K})\}}}{\mathrm{K}} = \sum_{n=0}^{\infty} \frac{\mathrm{X}^{(n)}(x_0)}{n!}(x-x_0)^n \tag{A1}$$

$$\mathrm{X}^0(0) = \lim_{\mathrm{K}\to 0} \frac{\sqrt{2(1-\cos\mathrm{K})}}{\mathrm{K}} = 1 \tag{A2}$$

$$\mathrm{X}^1(0) = \left[-\frac{\sqrt{2(1-\cos\mathrm{K})}}{\mathrm{K}^2} + \frac{\sin\mathrm{K}}{\mathrm{K}\sqrt{2(1-\cos\mathrm{K})}} \right]_{\mathrm{K}=0} = 0 \tag{A3}$$

$$\mathrm{X}^2(0) = \left[\frac{2\sqrt{2(1-\cos\mathrm{K})}}{\mathrm{K}^3} + \frac{\cos\mathrm{K}}{\mathrm{K}\sqrt{2(1-\cos\mathrm{K})}} - \frac{\sqrt{2}\sin\mathrm{K}}{\mathrm{K}^2\sqrt{1-\cos\mathrm{K}}} - \frac{\sin^2\mathrm{K}}{2\sqrt{2}(1-\cos\mathrm{K})^{3/2}} \right]_{\mathrm{K}=0} = \frac{1}{12} \tag{A4}$$

$$\mathrm{X}(\mathrm{K}) = 1 - \frac{\mathrm{K}^2}{24} + \frac{\mathrm{K}^4}{1920} - \frac{\mathrm{K}^6}{322560} + \frac{\mathrm{K}^8}{92897280} + \cdots \tag{A5}$$

$$\mathrm{X}(\mathrm{K}) = \sum_{n=0}^{\infty} \frac{1}{16^n} \frac{1}{n!} \frac{1}{(3/2)^{(n)}} \mathrm{K}^{2n} \tag{A6}$$

Appendix B

The steady state sheath compression of (4-6) ***when*** $x' = L$

$$\Delta L_{sheath}^{wn}\Big|_{x'=L} = \int_0^L \frac{T(x)\big|_{\delta=-1}}{E_s} dx + \int_L^L \frac{T(x)\big|_{\delta=1}}{E_s} dx \tag{B1}$$

$$= \frac{L\eta_0}{E_s\mu}\frac{1-e^{-\mu\phi}}{\phi}\cdot T_{in} + \frac{L\varsigma}{E_s}\left(\frac{1}{\mu}\frac{1-e^{-\mu\phi}}{\phi} - 1\right) \tag{B2}$$

The steady state sheath compression of (4-8) ***when*** $x' = L$

$$\Delta L_{sheath}^{rl}\Big|_{x'=L} = \int_0^L \frac{T(x)\big|_{\delta=1}}{E_s} dx + \int_L^L \frac{T(x)\big|_{\delta=-1}}{E_s} dx \tag{B3}$$

$$= \frac{L\eta_0^{-1}}{E_s\mu}\frac{e^{\mu\phi}-1}{\phi}\cdot T_{in} + \frac{L\varsigma}{E_s}\left(\frac{1}{\mu}\frac{e^{\mu\phi}-1}{\phi} - 1\right) \tag{B4}$$

The transient sheath compression of (4-6) ***when*** $0 \le x' < L$

$$\Delta L_{sheath}^{wn} = \int_0^{x'} \frac{T(x)\big|_{\delta=-1}}{E_s} dx + \int_{x'}^L \frac{T(x)\big|_{\delta=1}}{E_s} dx \tag{B5}$$

$$= -\frac{L\eta_0}{E_s\mu}\frac{e^{-\mu\phi'}-1}{\phi}\cdot T_{in} + \frac{L\varsigma}{E_s}\left(-\frac{1}{\mu}\frac{e^{-\mu\phi'}-1}{\phi} - \frac{\phi'}{\phi}\right) \tag{B6}$$

$$+\frac{L\eta_0^{-1}}{E_s\mu}\frac{e^{\mu\phi}-e^{\mu\phi'}}{\phi}\cdot T_{in0} + \frac{L\varsigma}{E_s}\left(\frac{1}{\mu}\frac{e^{\mu\phi}-e^{\mu\phi'}}{\phi} - 1 + \frac{\phi'}{\phi}\right) \tag{B7}$$

$$\phi' = \frac{1}{2\mu}\ln\left(\frac{\eta_0 T_{in0} + \varsigma}{\eta_0^{-1} T_{in} + \varsigma}\right) \tag{B8}$$

The transient sheath compression of (4-8) ***when*** $\mathbf{0 \le x' < L}$

$$\Delta L_{sheath}^{wn} = \int_0^{x'} \frac{T(x)\big|_{\delta=-1}}{E_s} dx + \int_{x'}^{L} \frac{T(x)\big|_{\delta=1}}{E_s} dx \tag{B9}$$

$$= -\frac{L\eta_0}{E_s\mu}\frac{e^{-\mu\phi} - e^{-\mu\phi'}}{\phi}\cdot T_{in0} + \frac{L\varsigma}{E_s}\left(-\frac{1}{\mu}\frac{e^{-\mu\phi} - e^{-\mu\phi'}}{\phi} - 1 + \frac{\phi'}{\phi}\right) \tag{B10}$$

$$+\frac{L\eta_0^{-1}}{E_s\mu}\frac{e^{\mu\phi'} - 1}{\phi}\cdot T_{in} + \frac{L\varsigma}{E_s}\left(\frac{1}{\mu}\frac{e^{\mu\phi'} - 1}{\phi} - \frac{\phi'}{\phi}\right) \tag{B11}$$

$$\phi' = \frac{1}{2\mu}\ln\left(\frac{\eta_0 T_{in} + \varsigma}{\eta_0^{-1} T_{in0} + \varsigma}\right) \tag{B12}$$

The transition tension of the approximated model

The transition point of the input tension from the phase 4 to phase 1 can be derived from the condition (B13) and calculated as (B14).

$$\Delta L_{sheath}^{steady}\Big|_{\delta=-1}\left(T = T_{D,wn}\right) = \Delta L_{sheath}^{steady}\Big|_{\delta=1}\left(T = T_0\right) \tag{B13}$$

$$T_{D,wn} = \frac{\mu\left(\eta_0^{-1} T_0 + 2\varsigma\right)\phi + 2\eta_0^{-1} T_0}{\eta_0\left(-\mu\phi + 2\right)} \tag{B14}$$

The transition point of the input tension from the phase 2 to phase 3 can be derived from the condition (B15) and calculated as (B16).

$$\Delta L_{sheath}^{steady}\Big|_{\delta=1}\left(T=T_{D,rl}\right)=\Delta L_{sheath}^{steady}\Big|_{\delta=-1}\left(T=T_0\right) \tag{B15}$$

$$T_{D,rl}=\frac{-\mu\left(\eta_0 T_0+2\varsigma\right)\phi+2\eta_0 T_0}{\eta_0^{-1}\left(\mu\phi+2\right)} \tag{B16}$$

Bibliography

[1] H. In, B. B. Kang, M. Sin, and K.-J. Cho, "Exo-Glove: A Wearable Robot for the Hand with a Soft Tendon Routing System," *IEEE Robot. Autom. Mag.*, vol. 22, no. 1, pp. 97–105, Mar. 2015.

[2] U. Jeong, H.-K. In, and K.-J. Cho, "Implementation of various control algorithms for hand rehabilitation exercise using wearable robotic hand," *Intell. Serv. Robot.*, vol. 6, no. 4, pp. 181–189, Sep. 2013.

[3] M. Nilsson, J. Ingvast, J. Wikander, and H. von Holst, "The Soft Extra Muscle system for improving the grasping capability in neurological rehabilitation," in *2012 IEEE EMBS Conference on Biomedical Engineering and Sciences (IECBES)*, 2012, pp. 412–417.

[4] C. J. Nycz, T. Bützer, O. Lambercy, J. Arata, G. S. Fischer, and R. Gassert, "Design and Characterization of a Lightweight and Fully Portable Remote Actuation System for Use With a Hand Exoskeleton," *IEEE Robot. Autom. Lett.*, vol. 1, no. 2, pp. 976–983, Jul. 2016.

[5] A. D. Deshpande, J. Ko, D. Fox, and Y. Matsuoka, "Control strategies for the index finger of a tendon-driven hand," *Int. J. Robot. Res.*, vol. 32, no. 1, pp. 115–128, Jan. 2013.

[6] Y. Ding, I. Galiana, A. Asbeck, B. Quinlivan, S. M. M. De Rossi, and C. Walsh, "Multi-joint actuation platform for lower extremity soft exosuits," in *2014 IEEE International Conference on Robotics and Automation (ICRA)*, 2014, pp. 1327–1334.

[7] J. F. Veneman, R. Kruidhof, E. E. G. Hekman, R. Ekkelenkamp, E. H. F. V. Asseldonk, and H. van der Kooij, "Design and Evaluation of the LOPES Exoskeleton Robot for Interactive Gait Rehabilitation," *IEEE Trans. Neural Syst. Rehabil. Eng.*, vol. 15, no. 3, pp. 379–386, Sep. 2007.

[8] B. Bardou, F. Nageotte, P. Zanne, and M. de Mathelin, "Improvements in the control of a flexible endoscopic system," in *2012 IEEE International Conference on Robotics and Automation (ICRA)*, 2012, pp. 3725–3732.

[9] T. N. Do, T. Tjahjowidodo, M. W. S. Lau, and S. J. Phee, "Adaptive control of position compensation for Cable-Conduit Mechanisms used in flexible surgical robots," in *2014 11th International Conference on Informatics in Control, Automation and Robotics (ICINCO)*, 2014, pp. 110–117.

[10] S. B. Kesner and R. D. Howe, "Robotic catheter cardiac ablation combining ultrasound guidance and force control," *Int. J. Robot. Res.*, vol. 33, no. 4, pp. 631–644, Apr. 2014.

[11] V. Agrawal, W. J. Peine, B. Yao, and S. Choi, "Control of cable actuated

devices using smooth backlash inverse," in *2010 IEEE International Conference on Robotics and Automation (ICRA)*, 2010, pp. 1074–1079.

[12] J. F. Veneman, R. Ekkelenkamp, R. Kruidhof, F. C. T. van der Helm, and H. van der Kooij, "A Series Elastic- and Bowden-Cable-Based Actuation System for Use as Torque Actuator in Exoskeleton-Type Robots," *Int. J. Robot. Res.*, vol. 25, no. 3, pp. 261–281, Mar. 2006.

[13] Y. Mao and S. K. Agrawal, "Design of a Cable-Driven Arm Exoskeleton (CAREX) for Neural Rehabilitation," *IEEE Trans. Robot.*, vol. 28, no. 4, pp. 922–931, Aug. 2012.

[14] R. Ozawa, H. Kobayashi, and K. Hashirii, "Analysis, Classification, and Design of Tendon-Driven Mechanisms," *IEEE Trans. Robot.*, vol. 30, no. 2, pp. 396–410, Apr. 2014.

[15] M. Grebenstein *et al.*, "The hand of the DLR Hand Arm System: Designed for interaction," *Int. J. Robot. Res.*, vol. 31, no. 13, pp. 1531–1555, Nov. 2012.

[16] M. Ciocarlie, F. M. Hicks, and S. Stanford, "Kinetic and dimensional optimization for a tendon-driven gripper," in *2013 IEEE International Conference on Robotics and Automation (ICRA)*, 2013, pp. 2751–2758.

[17] M. Kaneko, T. Yamashita, and K. Tanie, "Basic considerations on transmission characteristics for tendon drive robots," in *Fifth International Conference on Advanced Robotics*, 1991, pp. 827–832.

[18] G. Palli and C. Melchiorri, "Model and control of tendon-sheath transmission systems," in *2006 IEEE International Conference on Robotics and Automation (ICRA)*, 2006, pp. 988–993.

[19] Carlson, Lawrence E., Veatch, Bradley D., and Frey, Daniel D., "Efficiency of Prosthetic Cable and Housing," *J. Prosthet. Orthot.*, vol. 7, no. 3, pp. 96–99, Summer 1995.

[20] G. Palli, G. Borghesan, and C. Melchiorri, "Modeling, Identification, and Control of Tendon-Based Actuation Systems," *IEEE Trans. Robot.*, vol. 28, no. 2, pp. 277–290, Apr. 2012.

[21] K. Kong, J. Bae, and M. Tomizuka, "Torque Mode Control of a Cable-Driven Actuating System by Sensor Fusion," *J. Dyn. Syst. Meas. Control*, vol. 135, no. 3, Feb. 2013.

[22] P. Agarwal, J. Fox, Y. Yun, M. K. O'Malley, and A. D. Deshpande, "An index finger exoskeleton with series elastic actuation for rehabilitation: Design, control and performance characterization," *Int. J. Robot. Res.*, vol. 34, no. 14, pp. 1747–1772, Dec. 2015.

[23] L. S. Chiang, P. S. Jay, P. Valdastri, A. Menciassi, and P. Dario, "Tendon sheath analysis for estimation of distal end force and elongation," in *2009*

IEEE/ASME International Conference on Advanced Intelligent Mechatronics, 2009, pp. 332–337.

[24] U. Jeong and K.-J. Cho, "Feedforward friction compensation of Bowden-cable transmission via loop routing," in *2015 IEEE/RSJ International Conference on Intelligent Robots and Systems (IROS)*, 2015, pp. 5948–5953.

[25] K. P. Laby, R. M. Ohline, C. M. Pistor, C. E. Swinehart, B. R. Woodley, and A. Belson, "System for controlling an instrument using shape sensors," U.S. Patent 8 784 303, 22-Jul-2014.

[26] Y. L. Park *et al.*, "Real-Time Estimation of 3-D Needle Shape and Deflection for MRI-Guided Interventions," *IEEEASME Trans. Mechatron.*, vol. 15, no. 6, pp. 906–915, Dec. 2010.

[27] S. C. Ryu and P. E. Dupont, "FBG-based shape sensing tubes for continuum robots," in *2014 IEEE International Conference on Robotics and Automation (ICRA)*, 2014, pp. 3531–3537.

[28] H. Liu, A. Farvardin, S. A. Pedram, I. Iordachita, R. H. Taylor, and M. Armand, "Large deflection shape sensing of a continuum manipulator for minimally-invasive surgery," in *2015 IEEE International Conference on Robotics and Automation (ICRA)*, 2015, pp. 201–206.

[29] J. Jurgens and P. E. Patterson, "Development and evaluation of an inexpensive sensor system for use in measuring relative finger positions," *Med. Eng. Phys.*, vol. 19, no. 1, pp. 1–6, Jan. 1997.

[30] Mulder, A, "How to build an instrumented glove based on the Powerglove flex sensors," *PCVR Mag.*, vol. 16, pp. 10–14, 1994.

[31] L. K. Simone and D. G. Kamper, "Design considerations for a wearable monitor to measure finger posture," *J. NeuroEngineering Rehabil.*, vol. 2, no. 5, 2005.

[32] L. E. Dunne, B. Smyth, and B. Caulfield, "A Comparative Evaluation of Bend Sensors for Wearable Applications," in *2007 11th IEEE International Symposium on Wearable Computers*, 2007, pp. 121–122.

[33] R. Gentner and J. Classen, "Development and evaluation of a low-cost sensor glove for assessment of human finger movements in neurophysiological settings," *J. Neurosci. Methods*, vol. 178, no. 1, pp. 138–147, Mar. 2009.

[34] D. J. Sturman and D. Zeltzer, "A survey of glove-based input," *IEEE Comput. Graph. Appl.*, vol. 14, no. 1, pp. 30–39, Jan. 1994.

[35] T. G. Zimmerman, "Optical flex sensor," U.S. Patent 4 542 291, 17-Sep-1985.

[36] Y. L. Harvill, T. G. Zimmerman, and J. J. G. Grimaud, "Motion sensor which produces an asymmetrical signal in response to symmetrical movement,"

U.S. Patent 5 097 252, 17-Mar-1992.

[37] A. Tognetti, F. Lorussi, N. Carbonaro, and D. de Rossi, “Wearable Goniometer and Accelerometer Sensory Fusion for Knee Joint Angle Measurement in Daily Life,” *Sensors*, vol. 15, no. 11, pp. 28435–28455, Nov. 2015.

[38] M. Stoppa and A. Chiolerio, “Wearable Electronics and Smart Textiles: A Critical Review,” *Sensors*, vol. 14, no. 7, pp. 11957–11992, Jul. 2014.

[39] C.-T. Huang, C.-L. Shen, C.-F. Tang, and S.-H. Chang, “A wearable yarn-based piezo-resistive sensor,” *Sens. Actuators Phys.*, vol. 141, no. 2, pp. 396–403, Feb. 2008.

[40] R. Ponticelli and P. Gonzalez de Santos, “Full perimeter obstacle contact sensor based on flex sensors,” *Sens. Actuators Phys.*, vol. 147, no. 2, pp. 441–448, Oct. 2008.

[41] W. Peng, D. Tianhuai, and X. Feng, “A novel flexible sensor for compression stress relaxation,” in *Proceedings of IEEE Sensors*, 2003, pp. 265–268.

[42] J. R. Starck, G. Murray, P. V. Lawford, and D. R. Hose, “An inexpensive sensor for measuring surface geometry,” *Med. Eng. Phys.*, vol. 21, no. 10, pp. 725–729, Dec. 1999.

[43] Christopher T. Gentile, Michael Wallace, Timothy D. Avalon, Scott Goodman, Richard Fuller, Tracy Hall, “Angular displacement sensors,” U.S. Patent 5 086 785, 11-Feb-1992.

[44] Spectra Symbol, “Spectra Symbol Flex sensor.” [Online]. Available: http://www.spectrasymbol.com/flex-sensor. [Accessed: 12-Apr-2016].

[45] Flexpoint, “Flexpoint,” *Flexpoint Sensor Systems*. [Online]. Available: http://www.flexpoint.com/. [Accessed: 12-Apr-2016].

[46] K. Kure, T. Kanda, K. Suzumori, and S. Wakimoto, “Flexible displacement sensor using injected conductive paste,” *Sens. Actuators Phys.*, vol. 143, no. 2, pp. 272–278, May 2008.

[47] G. Saggio, “Electrical Resistance Profiling of Bend Sensors Adopted to Measure Spatial Arrangement of the Human Body,” in *Proceedings of the 4th International Symposium on Applied Sciences in Biomedical and Communication Technologies*, 2011, vol. 5.

[48] G. Saggio, “Mechanical model of flex sensors used to sense finger movements,” *Sens. Actuators Phys.*, vol. 185, pp. 53–58, Oct. 2012.

[49] Y. Qi, L. Ma, J. Sun, Z. Kang, Y. Bai, and S. Jian, “Highly sensitive bending sensor based on multimode–multimode–coreoffset fiber structure,” *Opt. Laser Technol.*, vol. 75, pp. 52–56, Dec. 2015.

[50] K. S. C. Kuang, W. J. Cantwell, and P. J. Scully, “An evaluation of a novel

plastic optical fibre sensor for axial strain and bend measurements," *Meas. Sci. Technol.*, vol. 13, no. 10, pp. 1523–1534, 2002.

[51] Y. Liu, J. A. R. Williams, and I. Bennion, "Optical bend sensor based on measurement of resonance mode splitting of long-period fiber grating," *IEEE Photonics Technol. Lett.*, vol. 12, no. 5, pp. 531–533, May 2000.

[52] S. Chen, Z. Tong, Q. Zhao, Z. Liu, and X. Dong, "A smart bending sensor with a novel temperature- and strain-insensitive long-period grating," *Sens. Actuators Phys.*, vol. 116, no. 1, pp. 103–106, Oct. 2004.

[53] Y. Dong *et al.*, "Novel bending sensor based on a meniscus shaped beam with LPG," *Opt. - Int. J. Light Electron Opt.*, vol. 124, no. 24, pp. 6737–6739, Dec. 2013.

[54] A. Taghipour, A. Rostami, M. Bahrami, H. Baghban, and M. Dolatyari, "Comparative study between LPFG- and FBG-based bending sensors," *Opt. Commun.*, vol. 312, pp. 99–105, Feb. 2014.

[55] Y. Miao, K. Zhang, B. Liu, W. Lin, and J. Yao, "Characteristics of bend sensor based on two-notch Mach–Zehnder fiber interferometer," *Opt. Fiber Technol.*, vol. 18, no. 6, pp. 509–512, Dec. 2012.

[56] S. J. Phee, S. C. Low, P. Dario, and A. Menciassi, "Tendon sheath analysis for estimation of distal end force and elongation for sensorless distal end," *Robotica*, vol. 28, no. 7, pp. 1073–1082, Dec. 2010.

[57] D. E. Knuth, "Two notes on notation," *Amer Math Mon.*, vol. 99, no. 5, pp. 403–422, Apr. 1992.

[58] "Torque Coil." [Online]. Available: http://www.asahi-inteccusa.com/index.php/medicalcomponents/products/torquecoil. [Accessed: 27-Oct-2016].

[59] "Dyneema Comprehensive Factsheet." Pelican Rope.

[60] S. Mehrotra, "On the Implementation of a Primal-Dual Interior Point Method," *SIAM J. Optim.*, vol. 2, no. 4, pp. 575–601, Nov. 1992.

[61] V. Berinde, *Iterative Approximation of Fixed Points*. Springer, 2007.

[62] D. Chen, Y. Yun, and A. D. Deshpande, "Experimental characterization of Bowden cable friction," in *2014 IEEE International Conference on Robotics and Automation (ICRA)*, 2014, pp. 5927–5933.

[63] V. Chernyak *et al.*, "The design and realization of a high mobility biomimetic quadrupedal robot," in *2012 IEEE/ASME International Conference on Mechatronics and Embedded Systems and Applications (MESA)*, 2012, pp. 93–98.

[64] J. C. Perry and J. Rosen, "Design of a 7 Degree-of-Freedom Upper-Limb Powered Exoskeleton," in *The First IEEE/RAS-EMBS International*

Conference on Biomedical Robotics and Biomechatronics (BioRob), 2006, pp. 805–810.

[65] J. v Zitzewitz, G. Rauter, R. Steiner, A. Brunschweiler, and R. Riener, "A versatile wire robot concept as a haptic interface for sport simulation," in *IEEE International Conference on Robotics and Automation (ICRA)*, 2009, pp. 313–318.

[66] P. Letier, A. Schiele, M. Avraam, M. Horodinca, and A. Preumont, "Bowden Cable Actuator for Torque-Feedback in Haptic Applications," in *Proc. Eurohaptics 2006 Conf.*, 2006.

[67] D. Sawada and R. Ozawa, "Joint control of tendon-driven mechanisms with branching tendons," in *2012 IEEE International Conference on Robotics and Automation (ICRA)*, 2012, pp. 1501–1507.

[68] H. In, U. Jeong, H. Lee, and K.-J. Cho, "A novel slack enabling tendon drive that improves efficiency, size, and safety in soft wearable robots," *IEEE Trans. Mechatron.*, Early Access.

[69] H. In, H. Lee, U. Jeong, B. B. Kang, and K.-J. Cho, "Feasibility study of a slack enabling actuator for actuating tendon-driven soft wearable robot without pretension," in *2015 IEEE International Conference on Robotics and Automation (ICRA)*, 2015, pp. 1229–1234.

[70] U. Jeong, H. In, H. Lee, B. B. Kang, and K.-J. Cho, "Investigation on the control strategy of soft wearable robotic hand with slack enabling tendon actuator," in *2015 IEEE International Conference on Robotics and Automation (ICRA)*, 2015, pp. 5004–5009.

[71] U. Jeong and K.-J. Cho, "A Feasibility Study on Tension Control of Bowden-Cable Based on a Dual-Wire Scheme," in *2017 IEEE International Conference on Robotics and Automation (ICRA)*, submitted.

[72] C. Majidi, "Soft Robotics: A Perspective—Current Trends and Prospects for the Future," *Soft Robot.*, vol. 1, no. 1, pp. 5–11, Jul. 2013.

[73] C.-H. Yeow, A. T. Baisch, S. G. Talbot, and C. J. Walsh, "Cable-Driven Finger Exercise Device With Extension Return Springs for Recreating Standard Therapy Exercises," *J. Med. Devices*, vol. 8, no. 1, Dec. 2013.

[74] M. Wehner *et al.*, "Experimental characterization of components for active soft orthotics," in *2012 4th IEEE RAS EMBS International Conference on Biomedical Robotics and Biomechatronics (BioRob)*, 2012, pp. 1586–1592.

[75] D. G. Kamper, T. George Hornby, and W. Z. Rymer, "Extrinsic flexor muscles generate concurrent flexion of all three finger joints," *J. Biomech.*, vol. 35, no. 12, pp. 1581–1589, Dec. 2002.

[76] R. M. Murray, Z. Li, S. S. Sastry, and S. S. Sastry, *A Mathematical Introduction to Robotic Manipulation*, 1 edition. Boca Raton: CRC Press,

1994.

[77] B. B. Kang, H. Lee, H. In, U. Jeong, J. Chung, and K. J. Cho, “Development of a polymer-based tendon-driven wearable robotic hand,” in *2016 IEEE International Conference on Robotics and Automation (ICRA)*, 2016, pp. 3750–3755.

[78] “US Endoscopy.” [Online]. Available: http://www.usendoscopy.com/. [Accessed: 24-Oct-2016].

[79] A. N. Kalloo *et al.*, “Flexible transgastric peritoneoscopy: a novel approach to diagnostic and therapeutic interventions in the peritoneal cavity,” *Gastrointest. Endosc.*, vol. 60, no. 1, pp. 114–117, Jul. 2004.

[80] X. Wang and M. Q.-H. Meng, “Robotics for Natural Orifice Transluminal Endoscopic Surgery: A Review,” *J. Robot.*, vol. 13, no. 2, Dec. 2012.

[81] A. M. de Lacy *et al.*, “Transanal natural orifice transluminal endoscopic surgery (NOTES) rectal resection: ‘down-to-up’ total mesorectal excision (TME)—short-term outcomes in the first 20 cases,” *Surg. Endosc.*, vol. 27, no. 9, pp. 3165–3172, Mar. 2013.

[82] B. P. M. Yeung and T. Gourlay, “A technical review of flexible endoscopic multitasking platforms,” *Int. J. Surg.*, vol. 10, no. 7, pp. 345–354, 2012.

[83] “Olympus America | Medical |.” [Online]. Available: http://medical.olympusamerica.com/. [Accessed: 24-Oct-2016].

[84] “KARL STORZ Endoskope.” [Online]. Available: https://www.karlstorz.com/kr/en/index.htm. [Accessed: 24-Oct-2016].

[85] L. Swanström, P. Swain, and P. Denk, “Development and Validation of a New Generation of Flexible Endoscope for NOTES,” *Surg. Innov.*, vol. 16, no. 2, pp. 104–110, Jun. 2009.

[86] J. Yonezawa, M. Kaise, K. Sumiyama, K. Goda, H. Arakawa, and H. Tajiri, “A novel double-channel therapeutic endoscope (‘R-scope’) facilitates endoscopic submucosal dissection of superficial gastric neoplasms,” *Endoscopy*, vol. 38, no. 10, pp. 1011–1015, 2006.

[87] “The Emergence of Flexible Endoscopy as Therapy,” *Laparoscopy Today*. [Online]. Available: http://www.laparoscopytoday.com/2005/01/the_emergence_o.html. [Accessed: 24-Oct-2016].

[88] D. Rus and M. T. Tolley, “Design, fabrication and control of soft robots,” *Nature*, vol. 521, no. 7553, pp. 467–475, May 2015.

[89] Lee, J. Y., Kim, W. B., Choi, W. Y., and Cho, K. J., “Soft Robotic Blocks: Introducing SoBL, a Fast-Build Modularized Design Block,” *IEEE Robot Autom Mag*, vol. 23, no. 3, pp. 30–41, Sep. 2016.

국문 초록

임베디드 굽힘 센싱을 활용한 보던 케이블 구동 시스템의 장력 제어

보던 케이블 구동방식의 주요한 문제 중 하나는 구동 경로 굽힘에 따라 변화하는 마찰에 의한 히스테리시스 현상이며, 이는 제어 성능을 감소시키고 적용 범위를 제한한다. 보던 케이블의 입력과 출력 장력 사이의 관계는 케이블의 굽힘 각도에 따라 변화하며 이는 지수 함수를 따른다. 본 연구에서는 임베딩 된 보조 와이어인 센싱 와이어를 사용하여 보던 케이블의 마찰로 인한 히스테리시스 변화를 보상하여 출력 장력을 제어할 수 있는 새로운 구동 방식을 제안한다. 본 논문에서는 센싱 와이어의 변위 변화와 구동 와이어의 입력 장력을 통하여 케이블의 누적 굽힘 각도를 추정하는 센싱 방식을 제안한다. 보던 케이블의 굽힘 모양이 변화하여도 추정된 굽힘 각도와 케이블 마찰 모델을 이용하여 피드포워드 방식으로 히스테리시스를 보상함으로써 출력단의 장력 센싱 없이 케이블의 출력 장력을 제어할 수 있다. 제안된 시스템은 쉬스 안에 완전하게 임베딩 된 디자인을

갖기 때문에 추가적으로 외부 굽힘 센서나 출력 장력 센서를 사용할 필요가 없어 엔드 이펙터의 크기와 복잡도를 낮출 수 있다. 이를 이용하여 보던 케이블의 굽힘 각도가 0°에서 400°까지 변할 때 출력 장력의 제어 오차는 5.21 N에서 0.50 N까지 변화하는 결과를 얻었다. 제안된 구동 시스템은 유연한 착용형 로봇 손에 적용되었으며 팔 움직임에 따른 쉬스 모양 변화에도 불구하고 일정한 크기의 파지력을 낼 수 있었다.

주요어 : 보던 케이블, 케이블 컨듀잇, 케이블 구동, 장력 제어,
굽힘 센싱, 마찰 보상

학 번 : 2010 – 23231